Characterization of the osteocyte lacuno-canalicular network and its interplay with the cement line in human osteonal bone

Auteur : Bastin, Sophie
Promoteur(s) : Ruffoni, Davide
Faculté : Faculté des Sciences appliquées
Diplôme : Master en ingénieur civil biomédical, à finalité spécialisée
Année académique : 2023-2024
URI/URL : http://hdl.handle.net/2268.2/20863

Characterization of the osteocyte lacuno-canalicular network and its interplay with the cement line in human osteonal bone

Master thesis conducted by

SOPHIE BASTIN

with the aim of obtaining the degree of **Master of Science in Biomedical Engineering**

Under the supervision of

DAVIDE RUFFONI

Academic year 2023 - 2024

Abstract

Osteons are bordered by a layer known as the cement line, which functions as an interface separating osteons from each other and from the surrounding interstitial bone (IB). However, the precise sequence of events surrounding the formation of cement lines remains poorly understood. While they provide an appropriate surface for osteoid deposition, they also fulfill a crucial function in bone quality. Cement line appears to contribute to bone strength and affects the connections between osteons, thereby influencing bone mechanosensitivity. In the osteon, there are osteocytes, trapped in lacunae, and connected by tiny channels called canaliculi. Together, they form the osteocyte lacuno-canalicular network (OLCN). Indeed, interactions between different structural elements of bone might be influenced by the quantity of canaliculi that can cross cement lines and connect osteocytes from adjacent osteons. However, despite their importance, the properties of cement lines have not been thoroughly studied. Specifically, the OLCN has been studied within osteons, but very rarely, if ever, outside of them. Indeed, only a few studies have analyzed the network at the border of the osteon, but they contradict each other. Some have observed connections, while others reported none. To address this uncertainty, our goal is to evaluate if there are connections between osteons and their surroundings and if these connections are more likely with IB or other osteons.

To conduct this study, we used two microscopy techniques on the same regions on two bone samples from human femurs: confocal laser scanning microscopy (CLSM) to measure the OLCN in samples stained by rhodamine and quantitative backscattered electrons imaging (qBEI) to measure the local mineral content of the osteon. We also used the open-access tool for image network analysis (TINA) on four different osteons. To conduct this analysis, we had to create a mask and, to choose some parameters to ensure the good analysis of the osteon and an appropriate subvolume to capture the heterogeneities within the network. The analysis started with the evaluation of canalicular density, followed by a qualitative analysis of their orientation. Then, the cells were studied by evaluating their shape according to the mineral content of the osteons and their position within the osteon. Finally, a qualitative analysis was performed on the density of the cells. We observed few connections between the osteon and its surroundings, and these connections are more likely with other osteons than with IB. These sparse connections could be explained by the fact that osteons could behave independently and may not need to communicate and to exchange information We also noticed a very striking absence of network in certain regions of IB which corresponds to the highest mineralized regions. This absence may be due to poor penetration of the rhodamine, potentially hiding the presence of a network. A potential explanation could be that the network may be disrupted with aging and the rhodamine might not be able to penetrate in this specific region. To validate this hypothesis, Focused Ion Beam in dual beam configuration with Scanning Electron Microscope (FIB-SEM) tests should be conducted.

One other interesting finding is that the number of lacunae seems to increase near the cement line. This potential increase in lacuna density could signify a higher activity of osteoblasts at the onset of bone remodeling. Another potential explanation is that the cells can better detect microdamage at the periphery enabling better communication with the external environment. On the other hand, the density of the canaliculi decreases near the cement line and their orientation shifts from being perpendicular to the Haversian canal to parallel as they reach the border. This work offers detailed characterization of the OLCN network within and beyond the periphery of an osteon, revealing sparse connections between osteons and the surrounding bone. These connections likely play a crucial role in bone mechanosensitivity and cellular communication. To further this analysis, increasing the number of samples would allow for the quantification of these connections through the cement lines in relation to tissue age.

Acknowledgements

First of all, I would like to express my sincere gratitude to Professor Davide Ruffoni for allowing me to carry out this interesting study and for guiding and advising me throughout my work.

Next, I would also like to thank Astrid Cantamessa for being available whenever I needed her and for helping me throughout my work. This work would not have been possible without her invaluable support, kindness and patience.

Finally, I would like to thank my family and friends, who I could count on every day and without whom I would not have reached this point. They have continually encouraged me and given me strength throughout my studies, and thanks to them, I can proudly present this work. I am eternally grateful for your love and support.

Contents

List of acronyms

2D	Two-dimensional
3D	Three-dimensional
BE	Backscattered electron
Ca.Dn	Canalicular density
CL	Cement line
CLSM	Confocal laser scanning microscopy
DoG	Difference of Gaussians
FIB-SEM	Focused Ion Beam in dual beam configuration with Scanning Electron Microscope
GL	Gray level
IB	Interstitial bone
LCN	Lacuno-canalicular network
OLCN	Osteocyte lacuno-canalicular network
qBEI	Quantitative backscattered electron imaging
ROIs	Regions of interest
TINA	Tool for imaging network analysis

Introduction

In cortical bone, lamellae wrap in concentric layers around a central canal, forming a structure called osteon or Haversian system. Each osteon is arranged around a central Haversian canal and is separated from one another by cement lines (CLs) [1] [2] [3] [4]. Between the tubular lamellae, rings of osteocytes are trapped in lacunae. These are connected by channels called canaliculi. The canaliculi spread out radially from the central Haversian canal. Osteocytes communicate with one another via gap junctions contained within these canaliculi [5]. The canaliculi and the lacunae form a complex network known as the osteocyte lacuno-canalicular network (OLCN) [6].

Research highlights the diverse roles played by the OLCN in material transport, mechanobiological signaling, mineral homeostasis, and bone remodeling. The ubiquity of the LCN within the bone ensures the delivery of essential nutrients to osteocytes and the removal of waste products [7]. A few articles have studied the OLCN at the border of the osteon, but these studies contradict each other. Some have observed connections, while others report none. Therefore, we do not really know what happens at the periphery of the osteon, which is why we are studying this. Additionally, the OLCN has been extensively studied within osteons, but very rarely, if ever, outside of them.

In this study, our focus is on the interface called the cement line (CL), an interface that seems highly effective at deflecting cracks and that ensures the structural unity of bones [8] [9] [10]. Interactions between different structural elements of bone are influenced by the quantity of canaliculi that can cross CLs and connect osteocytes from adjacent structural units [6] [11]. Despite their importance, the properties of CLs are not thoroughly understood [12] [13]. Studies suggest that this interface might be formed from the combined actions of osteoclasts, osteoblasts, and osteoprogenitor cells. However, the precise sequence of events surrounding the formation of CLs remains poorly understood. While these interfaces provide an appropriate surface for osteoid deposition, they also fulfill a crucial function in bone quality [4][14] [15]. Some studies suggest that for effective deflection of incoming cracks, the CL must be significantly weaker than both the osteons and the interstitial bone (IB) [11] [12] [16]. This contrasts with other studies where the CL is found to be stiffer [17]. There is also uncertainty about the composition, particularly regarding mineral content. Some studies indicate a lower mineral content in CLs compared to the surrounding bone [18], while others report a higher mineral content [3].

Our goal is to evaluate if there are connections between osteons and their surroundings and if these connections are more likely with IB or other osteons. This work is divided into 4 chapters. The first one concerns the introduction of the concepts useful to understand this study. Presenting the bone with its composition and its structure, how this entity can adapt in its environment. The OLCN is defined by explaining its components, (*i.e.*, the canaliculi and the lacunae). The CL is also described with a review of the studies carried out. Finally the two techniques used on the same regions of interest (ROIs), confocal laser scanning microscopy (CLSM) and quantitative backscattered electrons imaging (qBEI) are explained.

The second chapter explains the materials and the methods used to obtain the samples, the images and to conduct the image analysis. This chapter includes the sample preparation, a description of the different parameters for the qBEI and the CLS, the choice of four different osteons, the image processing tool TINA which is an open access tool for the image network analysis and the evaluation of the canaliculi and the cells with different image processing techniques.

The two lasts chapter are divided into two parts. The first one concerning the canaliculi and the second one

regarding the cells. In the third chapter, the results are presented. These results comprise the evaluation of the density of the canaliculi and their orientation within the osteons and around them. This chapter highlights also some results about the cells concerning their shape.

In the last chapter, the observations made in the previous chapter are related and discussed in relation to the literature in order to characterize the osteons and to evaluate the connections between the osteon and its surrounding. Then, the limitations are described, as well as perspectives for future work.

Chapter 1

Background

The aim of this chapter is to establish the contextual background for the topics investigated in this master thesis. Initially, bone composition and structure are explained, followed by an examination of bone adaptation and the interface investigated in this study. Subsequently, two characterization techniques are detailed: confocal laser scanning microscopy and quantitative backscattered electron imaging. Finally, the purpose of this thesis is introduced.

1.1 Bone

1.1.1 Composition & structure

Bones are fundamental organs in the human body and integral to the skeletal system of vertebrates. They vary in shape, size, and mechanical properties based on their location and function. They play critical roles in protecting internal organs, enabling movement, and storing minerals. Achieving these functions requires bones to possess a combination of lightness and strength level [19], which is made possible by their intricate hierarchical structure from the molecular to the macroscopic level [20] [21].

As can be seen in figure 1.1, bone is a hierarchical structure with various levels of organization from the sub-nanoscopic to the macroscopic level [22]. At the molecular level, bone is composed of a composite material consisting of 30% organic matrix, 70% inorganic phase that includes mineral crystals, and 10% water, with the organic matrix primarily comprising collagen type I, osteopontin, osteocalcin, and proteoglycans [23][24]. The collagen type I molecule forms a helical structure composed of three polypeptide chains [25]. These collagen molecules are then arranged periodically to form collagen fibrils [26]. Within these fibrils, inorganic minerals, specifically hydroxyapatite particles, are deposited primarily in the gaps between collagen molecules but also extend beyond the fibrils [27]. These collagen fibrils further assemble into fibers or bundles at the next organizational level, which are subsequently organized into lamellae or sheets.

At the macroscopic level, two types of bone can be distinguished: cortical and trabecular bone, differing at the microstructural scale [28]. In cortical bone, lamellae wrap in concentric layers around a central canal, forming a structure called osteon or Haversian system. Each osteon is arranged around a central Haversian canal containing arterioles, venules, capillaries, and nerves. Between the tubular lamellae, rings of osteocytes are trapped in lacunae. These are connected by channels called canaliculi. The canaliculi spread out radially from the central Haversian canal. Osteocytes communicate with one another via gap junctions contained within these canaliculi. Each osteon is separated from one another by CLs that are not crossed by either collagen fibers [22]. The orientation of these fibers within individual lamellae can vary, even though osteons are mostly oriented parallel to the long axis of bone [29].

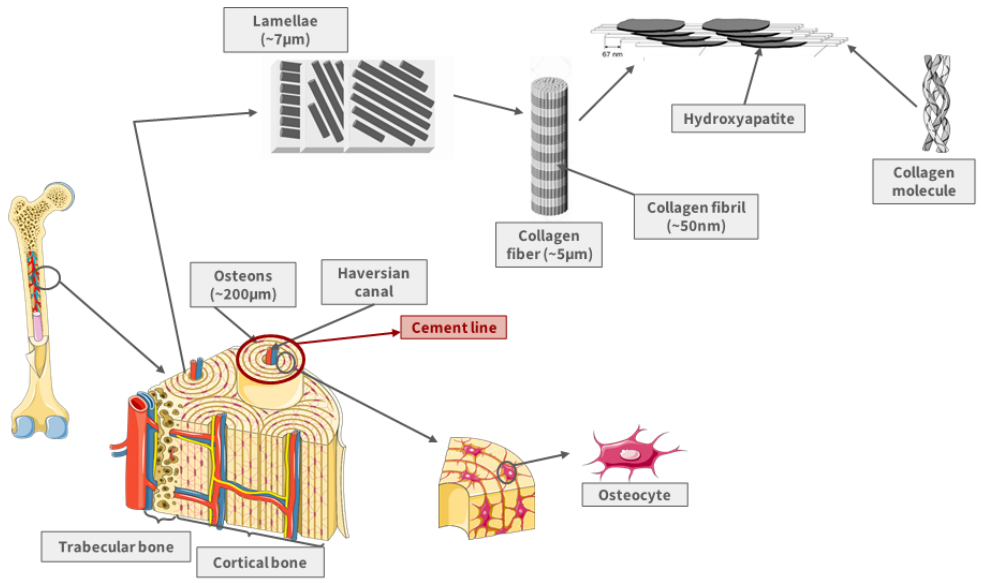

Figure 1.1: Hierarchical structure of bone from the sub-nanoscopic to the macroscopic level [1, 19, 30]. Inspired from [31].

Cortical bone is typically found at the outer layer of mature long bones, with low porosity mainly due to blood vessels and cellular spaces [32]. Trabecular (or cancellous) bone is found in areas subjected to high compression, filling the cortical bone shell. This bone is more porous and organized into a network composed of interconnected rods and plates called trabeculae. Blood vessels are located between the trabeculae rather than within them. Therefore, nutrition is provided by the bone marrow through diffusion [33]. A single trabecula consists of parallel lamellae, also referred to as bone packets, bounded by CLs and mainly oriented parallel to trabecular surfaces [34].

1.1.2 Adaptation

Bone is a dynamic living tissue characterized by its remarkable remodeling capability, allowing it to continually adjust to varying external biophysical stimuli within its environment to enhance functionality. Additionally, it possesses the ability to self-repair in the event of damage [35] [36]. Another function of bone remodeling is a mineral repository, capable of both storing and releasing minerals as required, or adjusting storage based on the mineral concentration in blood [37] [38].

This remodeling process is facilitated by the interaction of four types of bone cells: osteoblasts, osteocytes, osteoclasts, and bone lining cells. Osteoclasts are specialized cells tasked with bone resorption. As they break down bone tissue, osteoblasts step in to fill the resulting cavities with osteoids, a matrix consisting of non-mineralized bone components such as collagen, proteoglycans, and glycosaminoglycans. This matrix undergoes mineralization at a later stage. Subsequently, osteoblasts undergo differentiation, either integrating into the bone matrix to become osteocytes [39], or transforming into bone lining cells, or alternatively, undergoing apoptosis. The process of bone remodeling varies slightly between cortical and trabecular bone due to their occurrence on different surfaces: either at the intracortical/Haversian or at the endosteal/cancellous surfaces [40].

In cortical bone, osteons are formed through remodeling as osteoclasts and osteoblasts excavate circular tunnels through the bone matrix [6][41]. In trabecular bone, the process involves resorption of bone from the surface of trabeculae, leading to the formation of distinct bone packets at the surface [42]. These bone packets are not deposited simultaneously, resulting in variations in their mineral content over time [21].

Following their differentiation from osteoblasts, osteocytes within the bone matrix also develop their distinctive cellular extensions known as canaliculi. These osteocytes are housed within cavities called lacunae and communicate with neighboring cells through their dendritic projections within the canaliculi. Together with the cavities in which osteocytes reside (lacunae), these structures form a complex network known as the osteocyte

lacuno-canalicular network (OLCN) [6]. The OLCN is dynamic, as osteocytes can extend their dendrites to establish new gap junctions [5].

Osteocytes play crucial roles in bone health, including efficient transport, signaling, and mechanosensation [7] [43]. They regulate bone remodeling in response to environmental stimuli such as mechanical stress or hormonal changes by coordinating the activities of osteoclasts and osteoblasts [7].

1.1.3 Osteocyte lacuno-canalicular network

Osteocytes, originating from osteoblasts, are bone cells that arise when osteoblasts become embedded in their secreted matrix. They are not exactly formed but rather derived from former osteoblasts. These cells are interconnected via a network of canaliculi approximately 300 ηm in diameter. These osteocytes reside in lacunae that have a volume of about 400 μm³ [44] and a largest dimension exceeding 15 μm [43][45].

This interconnected system, referred to as the lacuno-canalicular network (LCN) [43], significantly influences the porosity of cortical bone [6] [46]. Researches highlight the diverse roles played by the LCN in material transport, mechanobiological signaling, mineral homeostasis, and bone remodeling.

Osteocytes, nestled within their lacunae in the bone, communicate directly through these canaliculi, enabling them to detect mechanical strains, alterations in loading, and micro-damage within the bone. In response to these signals, osteocytes can modulate the activity of osteoclasts and osteoblasts, the cell types responsible for bone remodeling [11][47] [48].

The ubiquity of the LCN within the bone ensures the delivery of essential nutrients to osteocytes and the removal of waste products [7].

Canaliculi

Studies have made several observations regarding canaliculi. The geometry of osteons does not seem to be correlated with the canalicular density, the volume occupied by the lacunae, or the distance between canaliculi [6].

It has been observed that canalicular density decreases from the Haversian Canal to the CL, with significant heterogeneity in the network, including areas where the network is inactive or not visible, likely due to poor penetration of rhodamine [6] [49]. In areas with high canalicular density, the degree of nodal connectivity is found to increase [50].

Moreover, conflicting findings exist regarding the canaliculi situated at the CL. Some propose that the canaliculi of osteocytes near the periphery of the osteon do not terminate at the CL but instead cross it and extend into the surrounding bone matrix, potentially influencing bone quality. This suggests that the CL may either disrupt the canalicular network [51] [52] or function as an impermeable barrier [53]. However, an alternative study observed that canaliculi can indeed go through the CL [54].

Peripheral canaliculi currently exhibit three distinct states: canaliculi that cross the CL, canaliculi that are interrupted at the CL, and a complete absence of visible canaliculi on the peripheral side of the outermost lacunae in osteons [11].

Lacunae

Regarding the cells, it has been observed that osteocyte lacunae from neighboring lamellae within the same osteon communicate both through direct connections between their radially oriented canaliculi and through indirect connections (between the radially and transversely oriented canaliculi) [11].

Osteocyte lacunae are believed to act as strain amplifiers, resulting in strain higher at the lacunar wall due to stress-concentrating effects [55].

Somes studies highlighted that although the lacunae appear to be randomly distributed in cross-section, they are actually orderly arranged along the length of the bone [43][56] [57] [58].

Additionally, a negative correlation between lacuna density and the mean degree of bone matrix mineralization is found [59].

Another study investigated the dependence of lacunae parameters on the distance from the Haversian canal to the CL. They found that the properties of lacunae vary according to their distance from the Haversian canal. Specifically, an increasing density of lacunae was observed near the CL, which then decreases at this interface. A notable decrease in this density was measured as the distance from the CL increased [60].

During the bone remodeling process, the rate of bone deposition by osteoblasts declines from the initial phase to the final phase, and this deposition rate is directly linked to the density of osteocytes [56] [61].

As the CL is the starting point for bone deposition [62], the increased density of osteocyte lacunae near the CL likely signifies elevated osteoblast activity at the onset of bone remodeling. Interestingly, it was found that the density of canaliculi varies inversely compared to the density of lacunae [60].

In figure 1.2, the OLCN network of an osteon and its surroundings, including the cells and canaliculi that comprise it, can be observed.

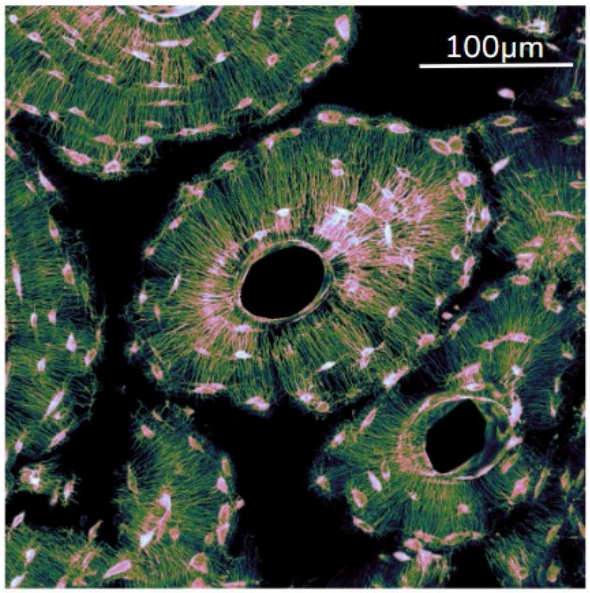

Figure 1.2: OLCN of one osteon and its surroundings obtained with CLSM and projected along the z direction on the entire stack.

1.1.4 Interfaces

The role of interfaces

Biological materials are usually comprised of a combination of elements: a rigid mineral phase, a more pliable organic phase, and a fluid component [33][63] [64].

These constituents are often organized hierarchically, with the organic phase acting as a binding agent between the mineral components. This organic phase, along with the presence of fluid, enables nonlinear deformation mechanisms, allowing inherently brittle materials to undergo partial inelastic deformation, redistribute stresses around imperfections, and absorb energy [65] [66].

Additionally, the organic components and fluid-filled pores act as pathways for cracks, directing them into configurations where their propagation is impeded or halted, thereby enhancing the material's toughness [63] [67].

The interfaces within biological materials have attracted significant attention due to their importance in governing deformation and fractures within them, despite occupying a small volume [63] [68] [69] [70] [71] [72].

Indeed, interfaces redirect cracks, guiding them into configurations that impede or stop their propagation, resulting in tougher materials [8][20] [73] [74].

For example, within enamel, mineral rods composed of hydroxyapatite crystalline rods are surrounded by proteins forming weak interfaces (Fig.1.3). This configuration directs cracks to propagate along the weak interface, bypassing the region where the mineral rods are situated, thereby preventing catastrophic failure [75] [76].

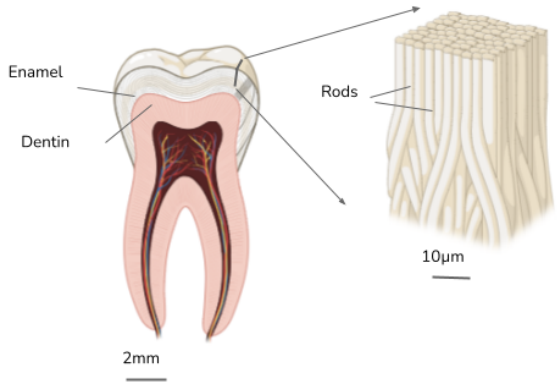

Figure 1.3: A summary of human dental anatomy and the microscopic composition of enamel with rods [77]. Inspired from [78].

Interfaces in man-made materials often serve as weak points, as the assembly of two distinct materials poses a significant challenge. Nature, on the other hand, has perfected this process, rendering such interfaces resilient. In this study, our focus is on the interface called the CL, which is an interface that seems highly effective at deflecting cracks and that ensures the structural unity of bones [8][9][10].

Cement line

Osteons are bordered by a layer known as the CL, which typically measures between 1 and 5 μm in thickness. These CLs function as interfaces that separate osteons from each other and from the surrounding IB [2] [3] [4].

They can also be found between bone and mineralized cartilage [79] [80], surrounding individual bone packets in trabecular bone [81] and also at osteochondral junctions [80].

Regarding their origin, CLs are formed during the reversal phase of bone remodeling, which connects the process of bone resorption with bone regeneration by creating a conducive environment for bone formation at remodeling sites. This intermediate period starts once the osteoclast departs and extends until the deposition of bone matrix begins [82] [83].

Studies have shown that osteoclasts, osteoblasts, and osteoprogenitor cells all have the capability to produce osteopontin, which is a marker associated with CLs. This suggests that these interfaces might be formed from the combined actions of these cells. However, there is a lack of understanding about the precise sequence of events surrounding the formation of CLs [4] [14] [15].

While those interfaces provide an appropriate surface for osteoid deposition [4], they are also supposed to fulfill a crucial function in the quality of bone. Indeed, microcracks can be deviated by reaching the CL depending on their size and path. This may lead to an improvement of bone fracture resistance [12] [13] [84] [85] [86].

The process by which microcracks are redirected and halted disperses energy, reducing the force driving crack propagation, all the while maintaining the integrity of both the osteon and the blood vessels housed within the central Haversian canal [8] [10] [85] [87] [88].

Studies exploring the potential interactions between different structural elements of bone suggest that these interactions are influenced by the quantity of canaliculi that can cross CLs and connect osteocytes from adjacent

structural units [6] [11]. Despite their importance, the properties of CLs are not thoroughly understood [12] [13].

Some studies suggest that for effective deflection of incoming cracks, it is essential for the CL to be significantly weaker than both the osteons and the IB [12] [13] [16].

However, this contrasts with other studies where the CL is found to be stiffer [17]. These studies present contrasting findings, but they employ different methods. For instance, Zhou et al. [13] used hydrated samples and measurements without confirming the CL position with another technique while Montalbano et al. [12] used indents with wider spacing compared to the study realized by Cantamessa et al. [17], and they determined the CL position using an optical microscope, although the interface is not clearly visible through it.

More intricate mechanical properties such as interfacial strength and fracture toughness remain even more difficult to precisely define. There is also an incomprehension about the composition and particularly at the level of mineral content. Some studies indicate a lower mineral content in CLs compared to the surrounding bone [18], while others report a higher mineral content [3]. Recent investigations, especially those employing methods like qBEI, propose that CLs commonly exhibit greater mineral [11] [60] [89].

Nonetheless, distinguishing CLs from the surrounding bone solely based on mineral density remains challenging [90] [91].

Furthermore, an unmineralized network of nanochannels smaller than the canaliculi connecting osteocyte lacunae has been found, and the CL appears to have a lower quantity of nanochannels compared to the surrounding bone. As a result, the hypermineralized condition of CLs could arise from their diminished nanochannel count [92].

As can be observed, there are only a small number of studies conducted on this subject, and there are still significant gaps in the research. This research topic is intriguing because the CL appears to contribute to bone strength and affects the connections between osteons, thereby influencing bone remodeling. However, since this area has not been thoroughly studied and the few existing studies are contradictory, further investigation is needed.

1.2 Characterization techniques

1.2.1 Confocal laser scanning microscopy

Conventional microscopy involves uniformly illuminating an entire sample positioned at the focal plane, using lenses to magnify the resulting image. Image quality is heavily influenced by the thickness of the sample being illuminated, as light scattered from objects both above and below the focal plane diminishes image contrast [93].

To mitigate the impact of the sample thickness and enhance optical resolution, a confocal microscope incorporates an extra lens to gather scattered light, coupled with a pinhole to eliminate out-of-focus signals before reaching the detector, as can be seen in figure 1.4. Confocal microscopy is engineered to eliminate obstructive out-of-focus light, thereby enhancing lateral resolution [93].

It presents significant advantages in image contrast and spatial resolution over traditional fluorescent microscopes. In contrast to traditional microscopes, these instruments employ lasers emitting light at various wavelengths, enabling fluorescence imaging and they additionally ensure a well-defined measurement volume in all three dimensions due to the confocal configuration [94]. The focal plane and the pinhole are positioned at "conjugate" planes of focus, hence the term "confocal," ensuring that only light emitted from the focal plane reaches the pinhole [95].

Light originating from out-of-focus regions within the sample is refracted differently by the objective lens. This stray light is filtered out by a small pinhole aperture, permitting only light from the focal point to proceed towards the detector [93].

This setup enables adjustments to the focal plane in the z-direction, allowing for the capture of a stack of images

throughout the entire sample. Moreover, since only one point in the sample is scanned at a time, scanning in the xy direction is achieved by employing scanning mirrors to move line by line.

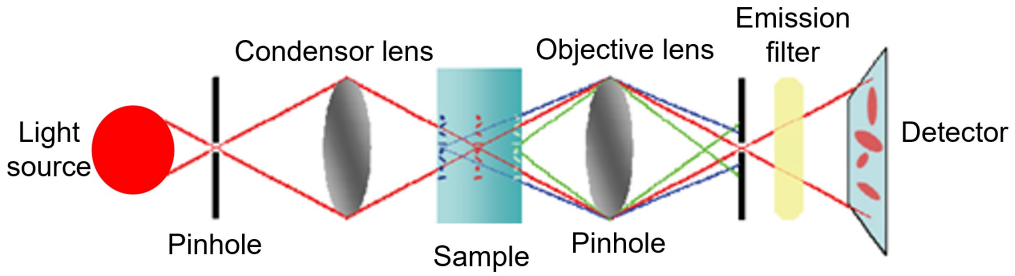

Figure 1.4: The fundamental design of a confocal microscope. The light from a photon source is directed through an entrance pinhole. Then this light is gathered by a condenser lens and focused onto the sample. Light that emanates from this focal plane is subsequently captured by the objective lens and focused through a second exit pinhole. The entrance, focal plane of the sample, and exit pinhole are aligned in conjugate focus (as indicated by the red lines) to ensure that only the focused light from the desired plane reaches the detector. Subsequently, the light passes through an emission filter that permits only specific wavelengths to reach the detector. Light originating from out-of-focus planes (represented by the blue and green lines) fails to reach the detector since it exits the pinhole out of focus [93].

Fluorescent molecules, known as fluorophores, can emit photons of a specific wavelength after absorbing light of a defined wavelength. This emission process occurs via an intermediate highly excited state of the molecule's energy, releasing fluorescence photons as it returns to the ground state. Due to transitions between electronic states, the emitted photons have lower energy and thus higher wavelengths. This wavelength shift allows for filtering of incoming light from the fluorescent signal, enhancing image quality.

To visualize the lacuno-canalicular network, fluorescent rhodamine (Rhodamine-6G) can be utilized. Rhodamine-6G solution stains non-mineralized tissue as well as osteoid, and due to its small molecular size, Rhodamine-6G diffuses rapidly through samples, staining all inner surfaces of the porosities in the mineralized tissue, including osteocyte lacunae and canaliculi [94].

1.2.2 Quantitative backscattered electron imaging

The technique of quantitative backscattered electron imaging (qBEI) relies on a specific electron-atom interaction signal, which can be employed to evaluate mineral content in mineralized tissues. When an electron beam strikes a sample, multiple interactions with its atoms occur, resulting in diverse signals.

These signals vary based on the energy of the beam and the structure of the sample. The interactions of electrons with the specimen give rise to elastic and inelastic scattering processes, which contribute to backscattered signals, as well as the generation of secondary electrons [93] [96].

Backscattered electrons (BEs) refer to electrons from the beam that are reflected back due to an elastic deviation by the atom nuclei as can be seen in figure 1.5. During elastic scattering, the energy of the electrons remains constant, while only their flight paths are altered. Consequently, a portion of the incoming electrons is scattered in the reverse direction. The quantity of BE contains valuable information regarding the atomic composition of the targeted area [94]. Thus, the BE signal is highly sensitive to the local atomic number Z: the higher the atomic number of the atoms struck by the beam, the stronger the BE signal.

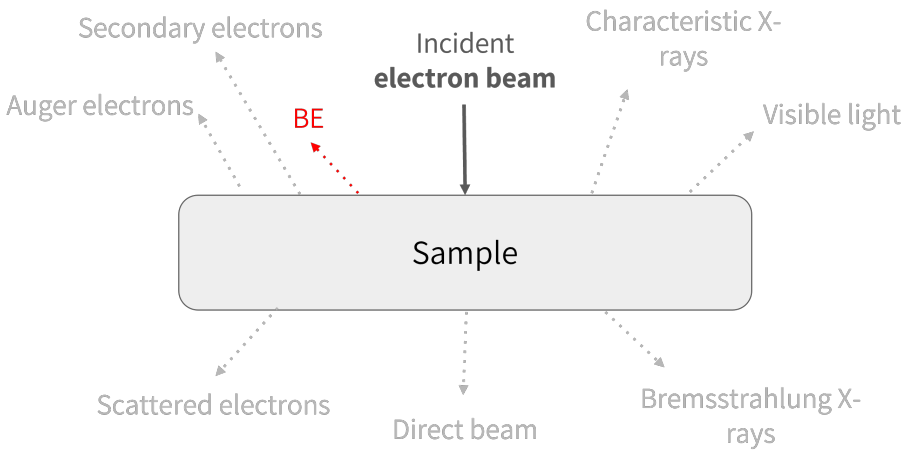

Figure 1.5: Backscattered electrons signal. The electrons from the beam are reflected back due to an elastic deviation by the atom nuclei of the sample, that interaction gives backscattered electron (BE) which is represented by the red arrow. Secondary electrons are low-energy electrons ejected from the sample. Auger electrons are electrons ejected following a specific relaxation process that occurs after the ionization of an atom in the sample. Scattered electrons are electrons from the incident beam that are scattered both inelastically and elastically by the atoms in the sample. Characteristic X-rays are emitted when inner-shell electrons of an atom are ejected and higher-energy electrons fill these vacancies, emitting X-rays characteristic of the element. Bremsstrahlung X-rays are produced when the incident electrons are decelerated by the electric field of the nuclei in the sample, emitting a continuous spectrum of X-rays. Visible light can be produced by the interaction of incident electrons with the sample. Direct beam is the electrons from the incident beam that pass through the sample without significant interaction.

Focusing on bone, a heterogeneous material, reveals that calcium (with an atomic number Z=20) is the predominant constituent influencing the intensity of BEs. Consequently, BEs can be utilized to assess local calcium concentration, indicative of mineralization degree which is a parameter relevant for determining bone age and offering insights into bone growth and remodeling dynamics [93][97].

In order to quantify this signal and establish a correlation between the gray level (GL) of BE images and the percentage of calcium, a calibration and standardization process needs to be followed [98]. This approach relies on the empirical observation that for elements with low atomic numbers (typically $Z < 20$), the relationship between BE intensity and local atomic number is roughly linear.

Consequently, the microscope undergoes initial calibration using carbon and aluminum standards: the brightness and contrast of the images are adjusted to achieve a GL of 25 ± 1 for carbon and 225 ± 1 for aluminum. This calibration enables the establishment of a reference line as seen in green in figure 1.6 (A) and ensures that the GL associated with hydroxyapatite, a compound with a known mean atomic number, is 255. This process facilitates the connection between GL and local calcium concentration [98].

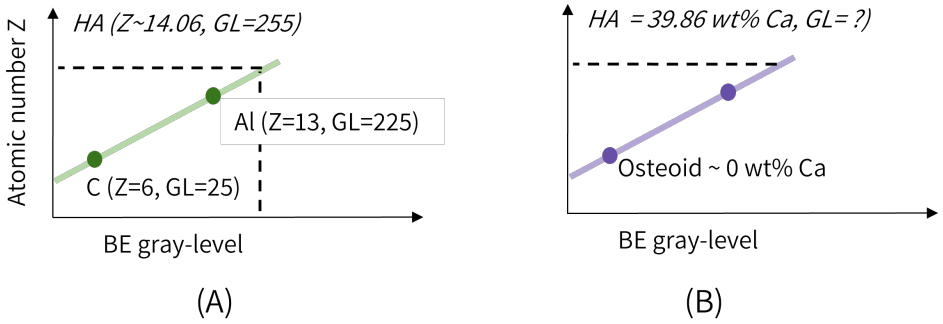

Figure 1.6: (A) : Atomic number as a function of BE gray-level. The green line was determined by the gray levels of carbon (C) and aluminum (Al). Then the gray value of hydroxyapatite (HA) was found by the calibration line with the Z of HA that is known. This GL is needed for the conversion of BE gray levels into calcium (Ca) concentration (B) : % calcium as a function of BE gray-level. The line was determined by osteoid and HA. Inspired from [98].

Secondly, the GL of osteoid, which is known to contain 0 wt % of calcium, is determined through experimental measurement. Additionally, since pure hydroxyapatite comprises 39.86 wt % of calcium, these two data points enable the establishment of the standardization line in purple on figure 1.6 (B), which connects calcium concentration and GL: Ca = 0.1733 GL - 4.332 [98]. Since bone undergoes continuous remodeling and mineral incorporation, its calcification is heterogeneous. qBEI emerges as a highly precise technique for assessing this process, where older tissue exhibits a brighter appearance compared to newer bone [21].

The bone mineralization density distribution, derived from the calcium content frequency distribution in an area scanned by qBEI, can provide insights into bone turnover, mineralization kinetics, average tissue age, and serve as a diagnostic tool or to evaluate treatment efficacy. The primary constraints of qBEI include the necessity for a biopsy sample and meticulous polishing to mitigate the effects of crystal orientation at the surface. Additionally, careful consideration of instrumental parameters is crucial as they can influence contrast [99]. It is essential to note that quantitative comparisons between qBEI measurements are only reliable when obtained using the same device and experimental settings.

1.3 Aim of this thesis

The previous section showed that the OLCN at the CL is an interesting controversy subject. Osteons are composed of lacunae where osteocytes reside, which interact through connections formed by canaliculi. Within the osteon, there are numerous connections. However, articles in the literature have mainly focused on the osteon alone, without considering its environment. These osteons have a border (*i.e.*, CL), beyong which, one can find IB or other osteons. The literature showed that studies are also highly controversial regarding the CL, its role, its composition, and its mechanical properties. This research topic is intriguing because the CL seems to contribute to bone strength and affects the communications between osteons, thereby influencing bone mechanosensitivity.

In this work, we aimed to understand if there is a complete disruption of the network at the CL or if some canaliculi are able to go through to connect the osteon to neighboring osteons or to IB. If such connections exist, the goal is also to determine if there are more inter-osteonal connections or more connection between the osteon and IB. Studies exploring potential interactions between different structural elements of bone suggest that these interactions are influenced by the number of canaliculi that can cross the CLs and connect osteocytes from adjacent structural units. These connections could influence communication between the osteon and its environment, which may include a more effective repair response in case of damage, for example.

Chapter 2

Materials and Methods

This chapter outlines the procedures and sample used to prepare the samples provided by A. Cantamessa for the characterization of the OLCN through the CL in human bone, the choice of the different osteons, the sequence of steps taken to conduct the image processing and to perform the evaluation on the canaliculi and on the cells.

The samples and the two first methods (qBEI and CLSM) utilized in this study were prepared and performed by Astrid Cantamessa during the first part of her PhD.

2.1 Sample preparation

During the necropsy at the Department of Forensic Medicine of the Medical University of Vienna, following approval by the institution's ethical commission (EK no. 1757/2013), two human femurs from male donors (aged 40 and 81 years) were obtained. These two bones were immediately frozen at -20°C for preservation prior to extraction and subsequent processing. Then, transverse cross sections (about 1.5 cm) were cut from the mid-diaphysis of the femur, perpendicular to its longitudinal axis. Following this, the sections were prepared according to a standardized procedure [92][98].

In this procedure, the following steps were:

(a) Dehydrated through graded ethanol series,

(b) Immersed in ethanol/acetone baths,

(c) Embedded in poly-methyl methacrylate (PMMA).

Before the embedding, samples underwent a staining with rhodamine (rhodamine-6G, 0.02% ethanol) which is a molecule of nanometer size capable of permeating all accessible pores and adhering to free surfaces.

2.2 Quantitative backscattered electron imaging

qBEI was employed for two-dimension spatial mapping of calcium content distributions in bone by measuring the intensity of the backscattered signal. Thanks to this, the degree of mineralization can be quantified [99] [98] [100].

Nineteen specific ROIs, each containing one or more osteons, were meticulously selected for analysis, encompassing the adjacent bone tissue. These ROIs were examined at a magnification of $\times 200$, providing a pixel resolution of 0.57 μm and allowing for a field of view of 1024×768 μm. This resolution allowed to accommodate the small dimensions of the CLs, typically measuring about 1-1.5 μm in transverse sections [92].

Calibration of the scanning electron microscopy backscattered signal was performed using carbon and aluminum standards, as described in section 1.2.2 [98].

The qBEI images of the osteons can be found in figure 2.1.

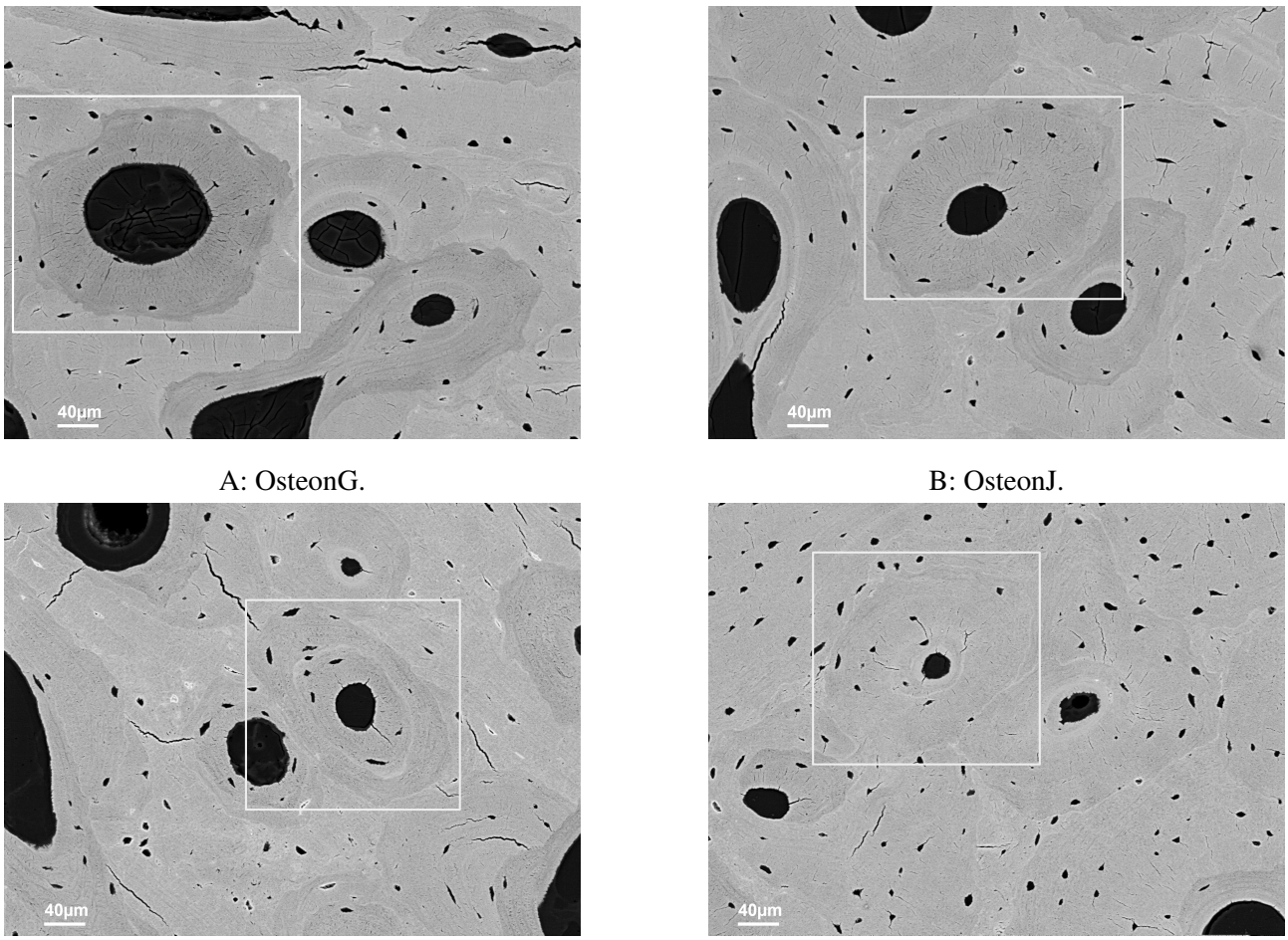

A: OsteonG. B: OsteonJ.

C: OsteonC. D: OsteonO.

Figure 2.1: qBEI of the four selected osteons and their surrounding environment, listed from least mineralized to most mineralized. The osteons chosen are highlighted with the white rectangles.

2.3 Osteons selection

First, to realize this study, four osteons have been chosen based on their mineral content and type. We included a large variability of mineral content and different types of osteons. OsteonG is the osteon with the lowest calcium content (Mean calcium content in the osteon (Os_{mean}) = 21.79 wt $\%$ and mean calcium content of the cement line (CL_{mean}) = 26.65 wt $\%$).

By contrast, osteonO is the osteon with the highest mineral content (Os_{mean} = 26.53 wt $\%$ and CL_{mean} = 28.67 wt $\%$). This osteon is a drifting osteon, (*i.e.*, an osteon characterized by continuous resorption on one side and continuous formation on the other). The mature drifting osteon that results has an off-center Haversian canal [101]. This osteon variety is distinguished by its motion occurring in both the longitudinal and transverse planes of the bone [101] [102]. Since we see a partial CL on the qBEI (Fig. 2.1D), osteonO could also be an osteon-in-osteon.

Two additional osteons of intermediate calcium content were also selected: osteonJ (Os_{mean} = 23.92 wt $\%$ and CL_{mean} = 26.2 wt $\%$) and osteonC (Os_{mean} = 25.94 wt $\%$ and CL_{mean} = 28.3 wt $\%$), a type II osteon (osteon-in-osteon). Type II osteons are used to distinguish them from the type I which are the “ordinary” osteons [103] [104] [105] [106]. They are known as embedded osteons and are essentially smaller versions of standard osteons that develop within the CL of an existing secondary osteon without crossing it. They originate from the radial erosion of a preexisting Haversian canal, followed by the inward deposition of lamellae [106] [101]. In these osteons, the connectivity of the canalicular network between the inner and outer regions is greatly reduced. By definition, type II osteons are characterized by having two concentric CLs [105]. We analyze these four osteons because they are different, they have completely different mineral content.

2.4 Confocal laser scanning microscopy (CLSM)

The same ROIs as for the qBEI have underwent imaging using a Leica TCS SP5 CLSM (Leica Microsystems, Wetzlar, Germany) equipped with a 63x oil immersion lens (HCX PL APO CS 63x 1.40 OIL) operating at a wavelength of 543 nm to facilitate rhodamine excitation. Fluorescence signals were captured between 553 and 705 nm. Each CLSM stack encompassed a volume of approximately $1024 \times 1024 \times 250$ pixels, with a voxel size of about $0.378 \times 0.378 \times 0.247$ μm. CLSM images of the four selected osteons can be found in figure 2.2.

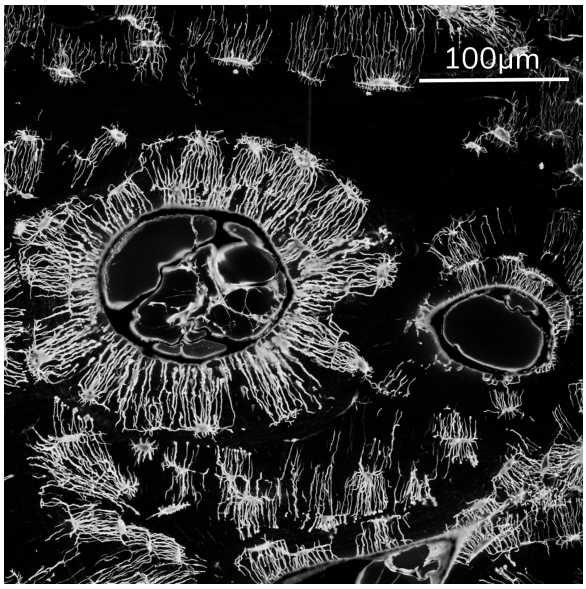

A: OsteonG and its surroundings.

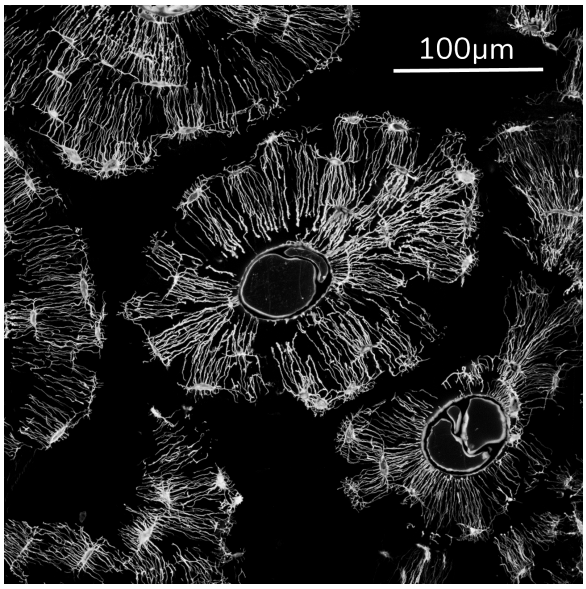

B: OsteonJ and its surroundings.

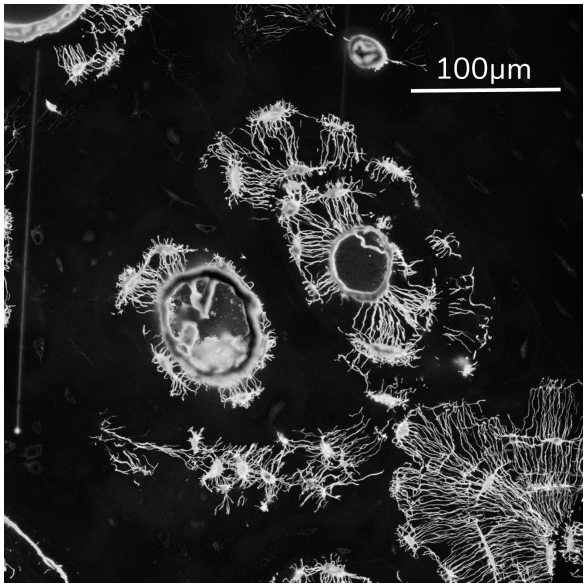

C: OsteonC and its surroundings.

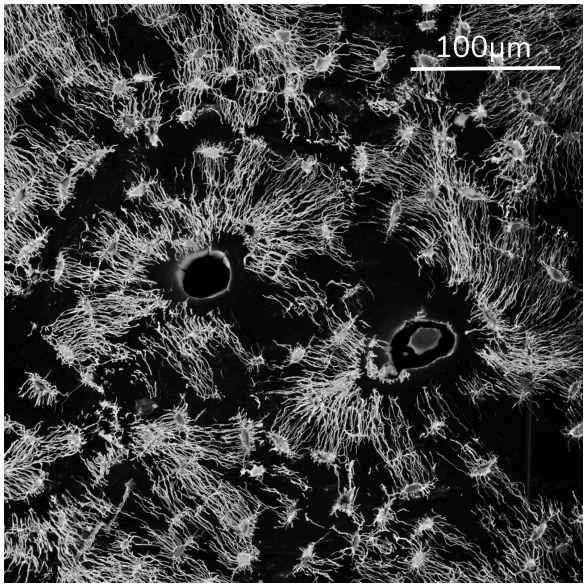

D: OsteonO and its surroundings.

Figure 2.2: CLSM of the fours selected osteons and their surroundings projected along the z direction over 12µm.

To confirm the type of each osteon, we looked at the second harmonic generation microscopy (SHG) that we can found in figure 2.3. Unfortunately, we do not have the SHG of the osteonJ at our disposal.

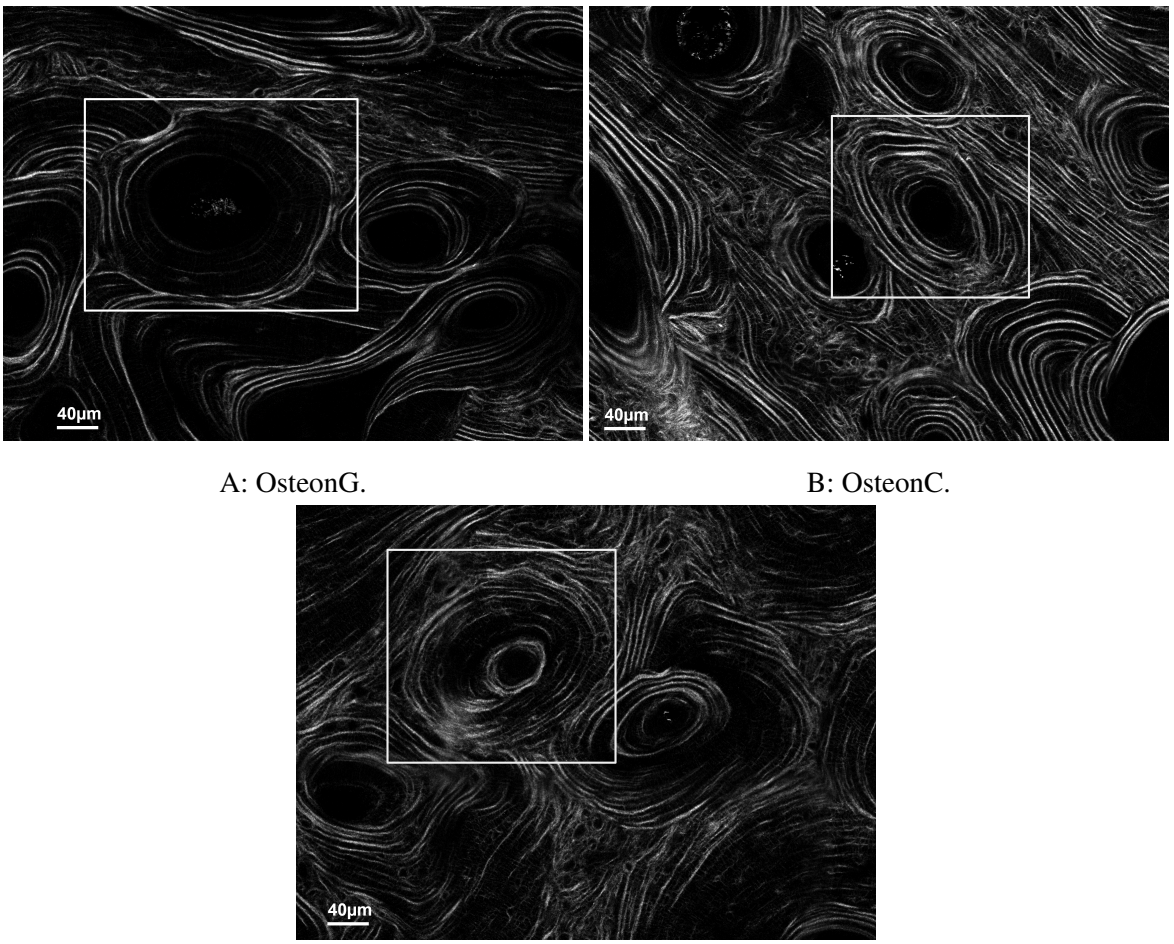

A: OsteonG. B: OsteonC.

C: OsteonO.

Figure 2.3: SHG images of osteonG, osteonC and osteonO and their surrounding environment used in this study. The osteons chosen are highlighted with the white rectangles.

2.5 Image processing

The CLSM dataset underwent binarization with an adaptive threshold and subsequent segmentation into canaliculi and larger pores using the in-house Python Tool for Image and Network Analysis (TINA) [107]. Initially, the stack of images obtained from confocal microscopy underwent binarization through a customized adaptive thresholding algorithm.

This algorithm, rooted in the concept of difference of Gaussians (DoG) [108], a classical feature enhancement technique in image science, was iteratively applied to accurately threshold both the canaliculi and the substantially larger lacunae. The first step is to define a set of parameters that are used to obtain good thresholded images. In this part, the choice of these parameters will be explained by showing an example of a typical osteon.

In imaging science, the DoG method is used to make features stand out better. It works by taking one version of an image that has been blurred a lot and subtracting it from another version that has been blurred less. This is typically done with grayscale images, where the original image is smoothed using different strengths of blurring. Blurring with a Gaussian kernel softens the sharp edges and details in the image. By subtracting one blurred image from another, DoG keeps the important details within a certain range of detail while getting rid of unnecessary noise. It is like using a filter to highlight specific features while smoothing out the rest [109].

2.5.1 Global thresholding

Initially, a global thresholding on the raw data (Fig.2.4) is performed to establish a threshold value that distinguishes between areas where the desired features exist and where they do not. This step is crucial for identifying regions where the features we are interested in are present.

Following global thresholding, an interactive visualization is conducted to determine the optimal threshold value, denoted as "thr", which produces satisfactory results. In this case, the value of the "thr" is 245 (Fig. 2.5).

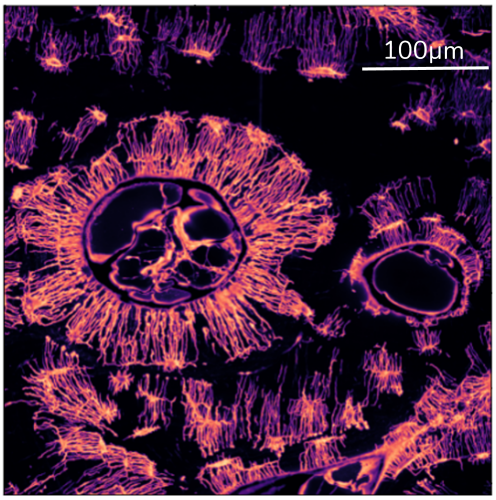

Figure 2.4: Raw data of the CLSM of the typical osteon.

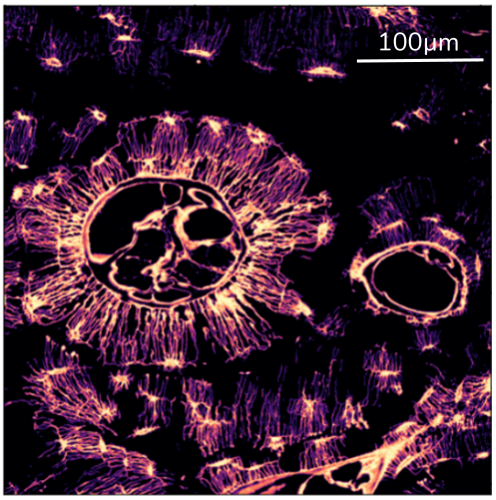

Figure 2.5: Thresholded data of the typical osteon with a threshold value of 245.

However, global thresholding has limitations as it does not fully consider the variation in intensity across the entire image. Consequently, certain areas may be inaccurately segmented, resulting in either too much segmentation or too little. This compromises the quality of subsequent segmentation analyses. Hence, adopting adaptive thresholding becomes necessary to address these limitations and improve the accuracy of the segmentation process.

2.5.2 Adaptive thresholding

In this section, we use the DoG method to threshold the osteocyte network. DoG can be likened to a feature detection mechanism or a band pass filter that targets specific feature sizes. This allows to segment the canaliculi and cells separately before combining them into a comprehensive representation.

Given that the diameter of the canaliculi is approximately the same as the optical resolution, all visualized canaliculi exhibit a similar diameter, much smaller than the typical distance between structures. Initially, the focus is on the canaliculi, where we must establish two smoothing ratios, denoted as s1 and s2, along with a threshold value "thr." Increasing s1 reduces noise, while a smaller distance between two radii requires a smaller threshold. Conversely, increasing s2 reduces noise but can also lead to thicker canaliculi with a lower threshold. In this case, the choice is s1= 0.6, s2= 1.2 and thr = 15 (Fig. 2.6).

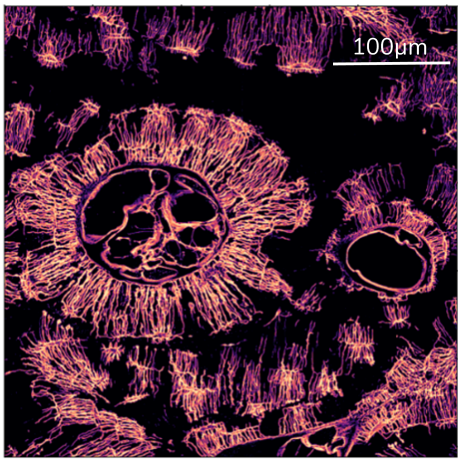

Figure 2.6: Thresholded data of the typical osteon with a threshold value of 15 with two smoothing ratios: s1= 0.6 and s2= 1.2.

For example, if we reduce s1 to 0.4, we can see that there is much more noise and we cannot distinguish the cells and the canaliculi (Fig. 2.7).

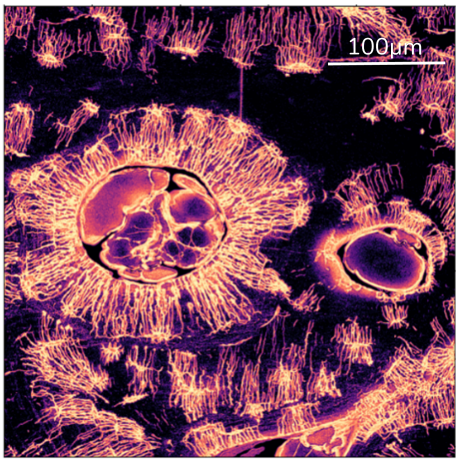

Figure 2.7: Thresholded data of the typical osteon with a threshold value of 15 with two smoothing ratios : s1= 0.4 and s2= 1.2.

In another example, if we increase s2 to 2 while keeping s1 = 0.6 and thr = 15, we can notice that the canaliculi become bigger and it is difficult to see difference between cells and canaliculi in terms of intensity (Fig.2.8).

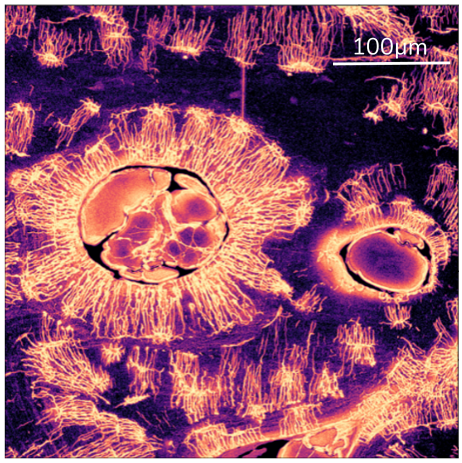

Figure 2.8: Thresholded data of the typical osteon with a threshold value of 15 with two smoothing ratios: s1= 0.4 and s2= 2.

Upon inspection of the cells at this stage, it becomes evident that they are no longer fully filled, and some may not appear as clearly defined cells. To improve their segmentation and achieve better thresholding, there are several approaches that can be explored. We can try to improve cells where only the surface gets thresholded, leaving a hollow body. We try to fill the cells because they can only be recognized as cells if they are completely closed.

To achieve this, we will apply the DoG method specifically for cells this time. Once again, we have three parameters: s1, s2, and thr. The goal is to create a contrast between cells and their surroundings. The idea is to make the cells more rounded like holes, without too many canaliculi standing out. In this case, the choice is s1 = 6.8, s2 = 8.9 and thr = 15. The threshold is chosen in order to not lose too much information (Fig. 2.9).

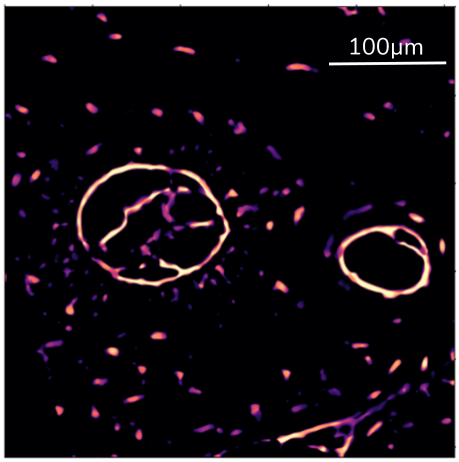

Figure 2.9: Thresholded data of the typical osteon with a threshold value of 15 with two smoothing ratios: s1= 6.8 and s2= 8.9.

If we choose s1 = 2.10 (Fig.2.10) for example, we obtain an image where we see the canaliculi but at this stage the focus is on the cells that is why s1 has been increased. In the case we increase s2 we have the same observation (Fig.2.11).

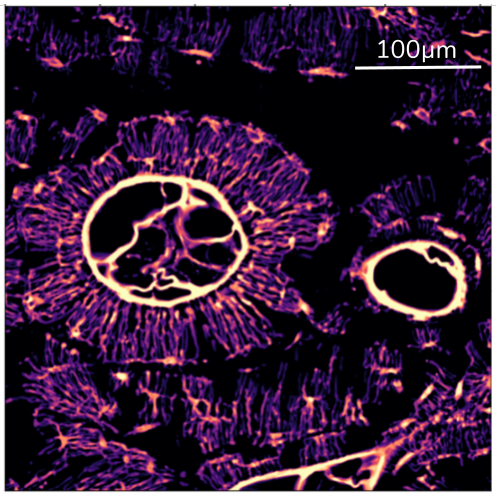

Figure 2.10: Thresholded data of the typical osteon with a threshold value of 15 and two smoothing ratios: s1= 6.8 and s2= 2.10.

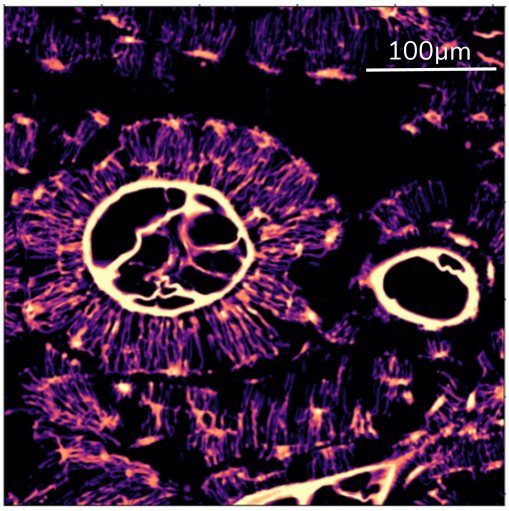

Figure 2.11: Thresholded data of the typical osteon with an increased smoothing ratio s2 to 10.

We also use morphological erosion to remove the canaliculi. Since some cells closely resemble the thickness of canaliculi, we generate a signal that peaks at the location of the canaliculi and decrease where the thresholding of the cells failed.

Then, we select a "$remove\_thr$" parameter to preserve areas where cells appear dark or empty while keeping canaliculi intact and bright. During this step, if we choose a very low "$remove\_thr$" we end up with an analyze where we underestimated the canaliculi. That is why we choose "$remove\_thr$" = 0.25. Subsequently, we perform another round of erosion and observe the appearance of blobs after removing the network. This allows us to determine whether we need to adjust the "thr" or "$remove\_thr$" parameters if cells are excessively removed.

Following this, we use erosion to eliminate small patches and promote cell growth. Finally, we visualize all steps and outcomes together (see Fig. 2.12), including the DoG method for identifying canaliculi and lacunae, as well as enhancements made by removing extraneous features such as extra noise.

The parameters chosen for this osteon are represented in table 2.1.

s1	s2	thr	sc1	sc2	thrc	$remove\_thr$
0.6	1.2	15	6.8	8.9	15	0.25

Table 2.1: Parameters chosen for the thresholding of the osteonG. s1, s2, and thr are related to the canaliculi and represent, respectively, the two smoothing ratios and the thresholding. sc1, sc2, and thrc are the same kind of parameters, but they are related to the cells. $remove\_thr$ is the parameter used to improve the final image.

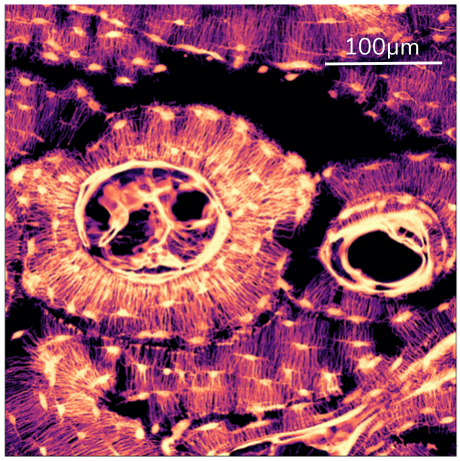

Figure 2.12: Visualization of the canaliculi and the lacunae of the typical osteon.

2.5.3 Segmentation

Following the thresholding process, segmentation was performed to distinguish between canaliculi and lacunae based on their distinct "bulkiness". The disparity in spatial dimensions between canaliculi and lacunae aided in segmenting these components. "Bulky" clusters of voxels associated with the network were examined to determine if they constituted a lacuna. This determination was made by extending these clusters further using a morphological dilation algorithm [6].

At the end of the segmentation, we obtained an image (Fig.2.13) where we can see the cells and the Haversian canal (in blue) and the canaliculi (in red).

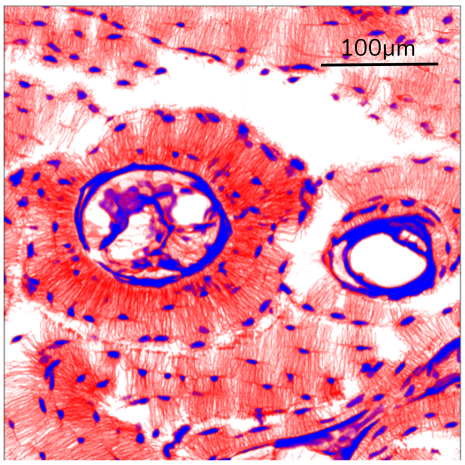

Figure 2.13: Image of the segmentation with the cells and the Haversian canal (in blue) and the canaliculi (in red) of the typical osteon.

2.5.4 Skeletonization

The subsequent stage in our image analysis procedure consisted of skeletonizing the image data (Fig.2.14). This procedure involved eliminating voxels from the surface, thereby producing a refined version of the original image that retains approximately uniform distances from its original boundaries while preserving the network's key topological characteristics, including connectivity, edge length, and orientation.

To accomplish this, the elimination of surface voxels had to stop when only a network comprising chains of voxels remained, as further elimination would have disrupted the topology of the network [6].

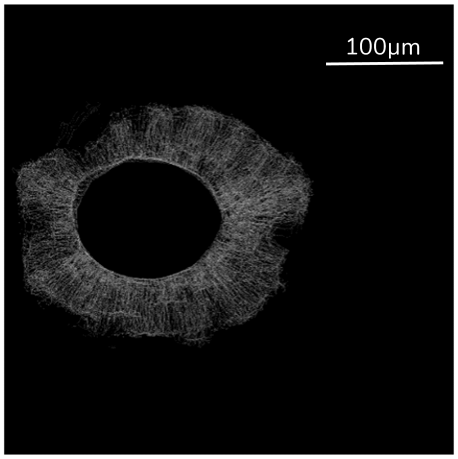

Figure 2.14: Image of the skeletonization of the typical osteon.

The outcome of the image analysis of the OLCN provides differentiation between lacunae and canaliculi, establishing the topology of the canalicular network as a graph composed of nodes (depicting the junction points of canaliculi) and connecting edges (representing the canaliculi themselves). Each canaliculus is represented by numerous spline segments, with the length of each segment being comparable to the dimensions of a voxel [6].

2.5.5 Network analysis

In order to make the analysis focus on an osteon, we performed a mask where the region in red is analyzed and regions in black or green are rejected (Fig.2.15).

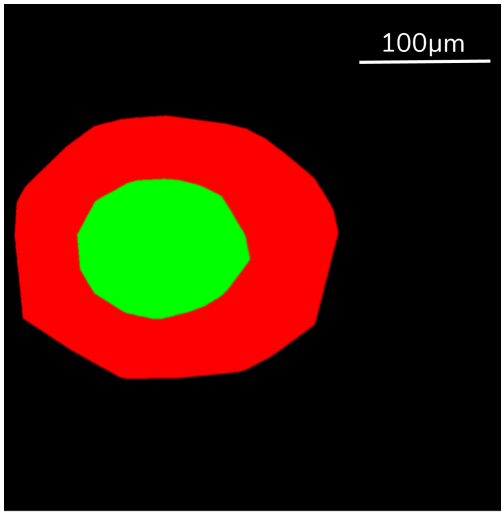

Figure 2.15: Mask of the osteon where the region in red is analyzed and regions in black or green are rejected.

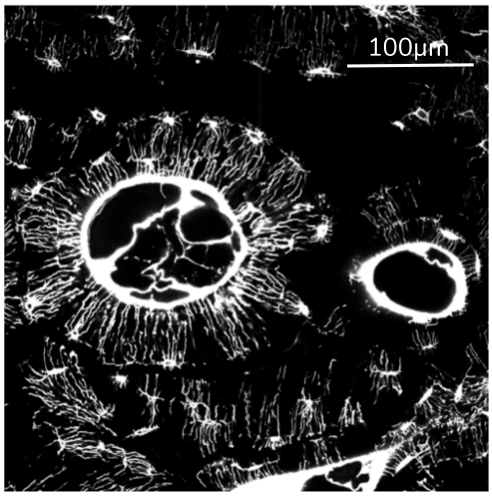

Figure 2.16: Raw data of the CLSM of the typical osteon

Next, the skeletonized images are transformed into a network graph, and this network undergoes smoothing through spline interpolations, where the voxels along all edges are replaced by a smoothing spline interpolation.

Subsequently, a basic network analysis is conducted, involving the calculation of histograms for the degree of the nodes and the weights of the edges. Exponential decay curves are fitted to these histograms. This is followed by a subvolume analysis aimed at capturing the heterogeneities within the network. The degree of

inhomogeneity within the network, as indicated by the distribution of density within small subvolumes, depends on the size of the subvolume.

We choose a subvolume size of 400 μm³ or 50 μm³, based on the analysis, as a representative volume, which is sufficiently large to encompass several canaliculi in most subvolumes and is comparable in size to osteocyte lacunae [6].

To obtain the density distribution of the network, the lengths of all subsections of the network are divided by the volume of the mask within the subvolumes as said earlier. The volume of the mask within each subvolume is determined by the mask voxels using a nearest neighbor approximation, given that the subvolumes are not uniformly sized. Smaller volumes typically exhibit a higher distribution, thus, the minimal size of the subvolumes included in the evaluation is defined by "minweight", which represents the minimum weight threshold.

Subsequently, the lacunae undergo analysis to calculate various properties of the segmented lacunae. If a mask is provided, only cells within the masked region are evaluated, allowing for the exclusion of small cells and cells with only a few connections. Finally, the projection is performed. The source code used for image processing is available for download [110].

2.6 Canaliculi and cells evaluation

2.6.1 Canaliculi

Density maps

One of the properties analyzed is the canalicular density (Ca.Dn) in μm/μm³, which corresponds to the total length of all the canaliculi in a given volume. Using TINA, a subvolume analysis is performed to better capture inhomogeneities within the network. In this case, the volume was partitioned into two different subvolumes of 400 μm³ (edge length = 7.368 μm) and 50 μm³ (edge length = 3.684 μm), with a minimum weight of 350 μm³ and 43 μm³, respectively. The minimum weight corresponds to the minimum size of the subvolumes included in the evaluation. The Ca.Dn was evaluated in each subvolume.

The inhomogeneity is influenced by the size of the subvolumes and is indicated by the width distribution of the Ca.Dn within the new volumes. If the subvolumes are too small, this results in a high proportion of empty subvolumes and a smaller proportion with high Ca.Dn. Briefly the subvolume must be large enough to yield robust values while being small enough to ensure good spatial resolution.

The subvolume of 400 μm³ is chosen to be large enough to encompass multiple canaliculi in each subvolume, and this size is comparable to the size of lacunae. The second choice of a 50 μm³ subvolume is justified by the small size of the CL, which is the focus of this study. The edge length of this subvolume is 3.684 μm, and the CL measures between 1 and 5 μm in thickness. Using this edge size ensures clear information on the variations around and within the CL.

The density means along z were computed using the software Matlab. The depth (z) of the image stack for each osteon was set at 40 μm to make the density means comparable. This depth corresponds to 162 images of the CLS stack.

Correlation density/degree

The degree of connectivity of a node is defined by the number of edges attached to it. This measure was correlated with the Ca.Dn to explore the relationship between the two properties. The degree was part of the TINA outputs and was computed as the number of edges per node.

The analysis was performed using Matlab, and the correlation was considered significant if the p-value was less than 0.05. The Pearson coefficient was calculated, with a lower limit of -1 and an upper limit of 1. A value of 0 corresponds to no correlation, while an absolute value of 1 indicates a perfect linear correlation, which may be negative or positive depending on the sign. The subvolume chosen here is 50 μm³.

Histograms

The frequency distributions of the Ca.Dn were evaluated in all the osteons with a bin width of about 0.01 μm/μm³ over a depth of 40 μm . The subvolume chosen here is 50 μm³.

Layers analysis

To evaluate the changes in Ca.Dn inside the osteon, several concentric layers were analyzed. The goal was to assess the variation in density from the Haversian canal to the CL. First, a mask of the Haversian canal was created by contouring it manually (Fig. 2.17).

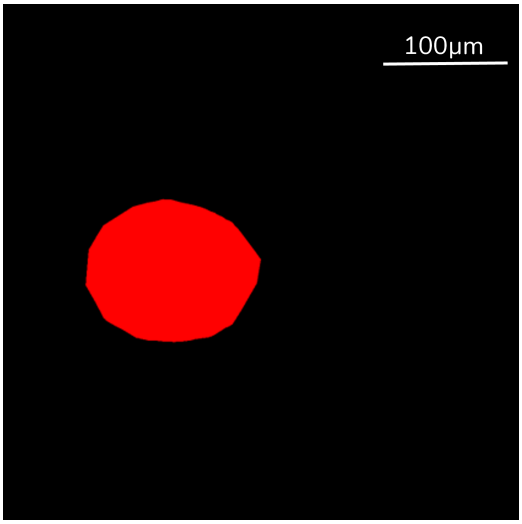

Figure 2.17: Mask of the Haversian canal of the osteonG (red = 1; black = 0). The slice number is 23 over 261.

This mask then underwent multiple cycles of dilation to produce multiple masks of layers, each 5 pixels thick. For example, the mask was dilated by 5 pixels, and the original mask was subtracted from it, resulting in a 5-pixel layer located just beyond the Haversian canal.

Unfortunately, due to the different morphologies of the canal and the CL, it was not possible to reach the CL by taking layers of the shape of the Haversian canal. When the mask continued to be dilated, it ended up crossing the CL without fully accounting for it as can be seen in figure 2.18.

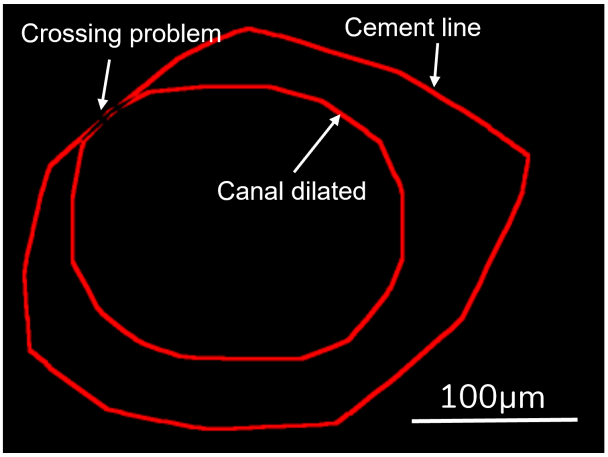

Figure 2.18: Mask of the crossing of the CL (5 pixels) and the layer of the canal dilated (5 pixels) of the osteonG. The slice number is 244 over 261.

To overcome this problem, the analysis was divided into two parts. For the first part, several layers were created as previously described, starting from the Haversian canal until touching the CL (Fig. 2.19). The number of

layers depends on the geometry of the osteon and the size of the canal. For example, osteonG had fewer layers than osteonO because the canal in osteonG is larger.

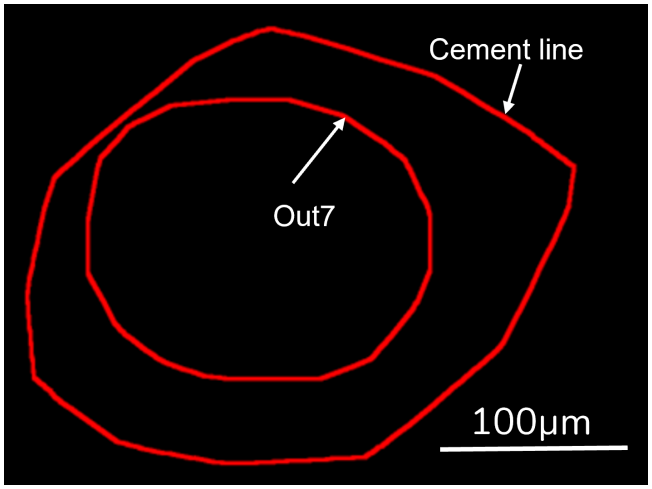

Figure 2.19: Mask of the last layer of the canal dilated and the CL of the osteonG. The slice number is 244 over 261.

The layers are named according to their position relative to the canal. For example, the layer "Out1" corresponds to the layer just after the canal, "Out2" is the layer just after "Out1," and so on (Fig. 2.20).

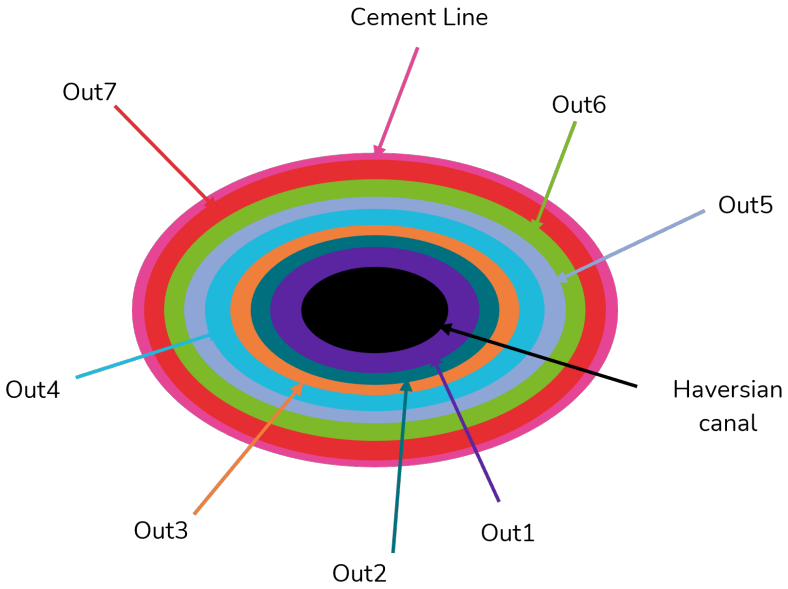

Figure 2.20: Layers used to make the density analysis starting from the Haversian canal. The layers are named according to their position relative to the canal.

The second part involves creating layers from the CL until reaching the Haversian canal by taking into account the morphology of the CL and the osteon. To create these layers, multiple cycles of erosion were applied on the mask of the osteon shown earlier (Fig. 2.15).

The erosion process stopped just before reaching the canal. For example, the layer "In1" was calculated by taking the osteon mask, eroding it by 5 pixels, and then subtracting the eroded mask from the original mask. The result is a layer of 5 pixels just before the CL. Subsequently, "In2" logically represents the layer of 5 pixels just before "In1" (Fig. 2.21).

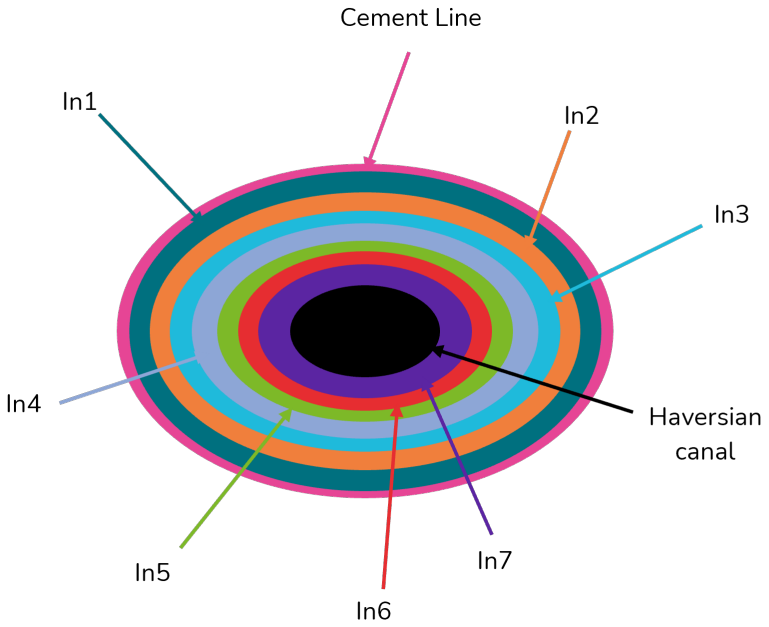

Figure 2.21: Layers used to make the density analysis starting from the CL. The layers are named according to their position relative to the CL.

All the layers computed for this analysis have a pixel size of 5, representing 1.895 μm of thickness. This size was chosen to be comparable to the thickness of the CL.

The CL is also represented by a layer of 5 pixels. To compute this layer, the mask of the osteon was taken, dilated by 5 pixels, and then the original mask was subtracted from the dilated one.

To perform the analysis on the Ca.Dn, the previously calculated density by TINA, as explained before, was multiplied by the mask of each layer obtained. However, a problem arose due to the incompatibility of the sizes of the density image and those of the mask of the layers. The masks had a size of about $1024 \times 1024 \times 250$ pixels like the original images stack, while the density image had a size of about $106 \times 106 \times 20$ pixels due to the partitioning into subvolumes of 50 μm³, depending on the osteon for the z direction. Two different resizes had to be made: one for the z direction and another for the x and y directions.

To address the size discrepancy issue, resizing had to be applied either to the mask or the image. The resize on the mask and the resize on the image were both tested and yielded relatively similar results.

Firstly, for the z direction, resizing was performed on the mask using interpolation in Matlab. To preserve the binary nature of the mask (1 and 0), a threshold was applied. Specifically, values above 0.5 were set to 1, and values below were set to 0. Secondly for the x and y directions, to address the size discrepancy issue, resizing had to be applied either to the mask or the image. The resize on the mask and the resize on the image were both tested and yielded relatively similar results. What seemed more appropriate for the x and y directions was the resizing on the image because visualizing the resized mask revealed gaps in the layers image as can be seen in figure 2.22.

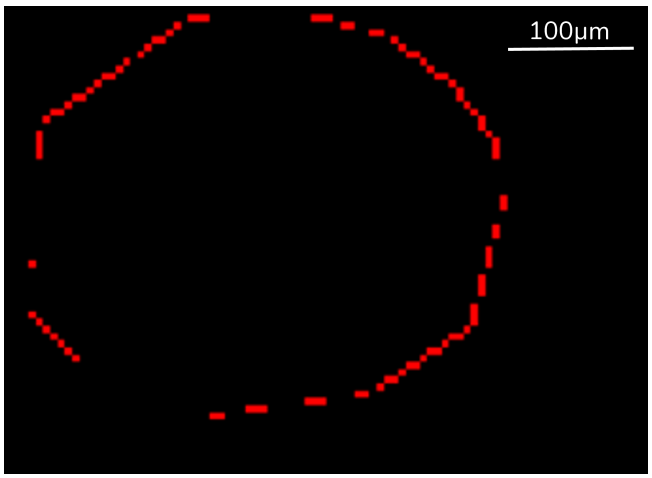

Figure 2.22: Resizing method used on the mask of the CL of the osteonG. The slice number is 1 over 261.

The resize in x and y directions was executed using the "imresize" function in Matlab with bicubic interpolation. Following the resize, the image was multiplied by all the layer masks to generate multiple vectors, each corresponding to one layer. To visualize the density evolution from the Haversian Canal to the CL, two plots were created, one starting from the Haversian canal and the other starting from the CL, showing the calculation of the density mean and standard deviation mean with corresponding error bars.

Orientation

To visualize the network data and evaluate the orientation of the canaliculi, a 3D visualization library for Python is used. Initially, the data is loaded, and then the orientation of the graph is projected using a cylindrical vector which represents the center of the Haversian canal. This process involves adjusting the positions or orientations of the nodes and edges of the graph based on this specified vector to enhance visualization. Consequently, specific components or the entirety of the graph are aligned with the user-defined cylindrical vector. To analyze the orientation of the canaliculi, we defined an angle θ.

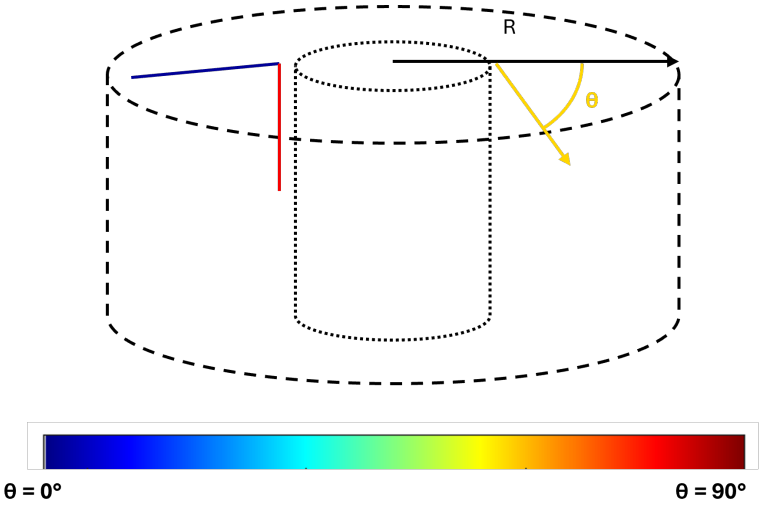

Figure 2.23: Angle θ used to determine the orientation of the canaliculi wihtin the osteon. If θ is blue the canaliculi are radial to the Haversian canal and if θ is in red, the canaliculi are parallel to the canal.

Such an operation is often essential for preparing data for 3D visualization, where orientation and perspective significantly influence data interpretation. Finally, isosurfaces, which are three-dimensional surfaces generated from volumetric data, are plotted, resulting in a 3D graph.

2.6.2 Cells

The TINA code also provides information about the cells. The volume of each lacuna within a segmented image was computed in μm/μm³ by counting the number of voxels contained within each lacuna and multiplying this count by the volume of a single voxel. The volume of a voxel is determined based on the spacing between voxels along each dimension of the image.

Additionally, the shape of the lacunae is evaluated and characterized by the lacunae oblateness and stretch. Lacuna stretch ($Lc.St$) is defined as the normalized difference between the largest and smallest eigenvalues of the shape tensor (*i.e.*, a mathematical representation used in geometry and image analysis to describe the shape of a three-dimensional object):

$$Lc.St = \frac{\lambda_{S,3} - \lambda_{S,1}}{\lambda_{S,3}} \tag{2.1}$$

with $\lambda_{S,i}$ (i = 1–3) being the three shape tensor eigenvalues and where $\lambda_{S,1}$ and $\lambda_{S,3}$ are the largest and smallest eigenvalues, respectively. The value of $Lc.St$ varies between 0 and 1, with 0 representing a spherical shape and 1 indicating infinite stretching of the lacunae [111].

Lacuna oblateness ($Lc.Ob$) characterizes whether the lacuna is more prolate or oblate. It is calculated as follows:

$$Lc.Ob = 2\frac{\lambda_{S,2} - \lambda_{S,1}}{\lambda_{S,3} - \lambda_{S,1}} - 1 \tag{2.2}$$

If $Lc.St$ = 0, $Lc.Ob \approx$ -1 indicates a more prolate (*i.e.*, elliptic) shape, while $Lc.Ob \approx 1$ suggests an oblate (*i.e.*, spherical) shape. This measure provides information on the geometrical anisotropy of osteocyte lacunae, in addition to stretch [111].

To evaluate the properties of the cells with the radial direction of the osteon. The distance (d) of the cells from the center of the Haversian Canal was computed using Matlab with the coordinates of each cell provided by TINA. First, the center of the canal is located using its mask. Then, each cell is located from the corresponding center at the same z-coordinate using the formula:

$$d = \sqrt{(x_B - x_A)^2 - (y_B - y_A)^2} \tag{2.3}$$

with d the distance between the center and the cells, (x_A, y_A) the coordinate of the center and (x_B, y_B) the coordinate of the cell.

All these computed values were reported in graphs represented as box plots and scatter plots for all four osteons. In particular the relation between the previous parameters and the mineral is evaluated. The parameters of stretch, oblateness, volume, and distance are also evaluated in relation to each other.

2.6.3 Statistics

To evaluate the potential correlation between the Ca.Dn and the degree of connectivity, we used Pearson correlation. We also used ANOVA test to compare the properties of the lacuna. Significance levels were set at $p \leq 0.05$. The statistical analysis was performed in MatlabR2022b to compare the properties of lacunae.

Chapter 3

Results

The aim of this chapter is to present all the results obtained from the quantitative evaluation of the canalicular density and the qualitative evaluation of the orientation of the canaliculi, as well as the results concerning the cells and their variations in shape.

3.1 Canaliculi

3.1.1 2D maps density

The 2D maps (Fig.3.1) illustrate the average density along the z-axis of 40 μm for each osteon. Initially, we compare two distinct subvolumes: one measuring 400 μm^3 (Fig.3.2) and the other 50 μm^3 (Fig.3.1A) to detect potential variations between them.

Both subvolumes reveal identical regions of zero density and high-density areas. The key distinction lies in the smaller subvolume containing more empty pixels, as described in the method. This comparison demonstrates that both subvolumes exhibit comparative density representations. Knowing that, we chose to analyze the images with a subvolume of 50 μm^3 to have a more precise idea of the CL density.

In the visualizations, dark blue indicates zero densities, while red highlights regions of high density, reaching approximately 0.15 $\mu m/\mu m^3$. The gray areas represent the Haversian canals. In this part we will present the results for all the osteons.

For the osteon labeled as osteonG on the left side of figure 3.1A, we observe localized zones of high density and significant heterogeneity within the osteon. The high density is predominantly concentrated around the canal and diminishes towards the border of the osteon (*i.e.*,the cement line). On the left part of the osteonG, we perceive a connection with another osteon.

To identify potential changes along the z-axis direction, we averaged the density over depth of 10 μm (see Fig.3.3). Within the first 10 μm depth, we notice fewer areas of high density and no visible connections with the surrounding area. Moving deeper, between 10-20 μm, the areas of high density increase, and beyond 20 μm, connections start to appear in the lower right section of the osteon as can be seen in figure 3.3 with the white dotted square.

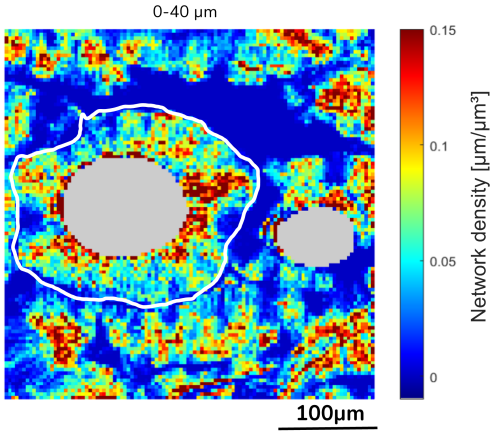

A: OsteonG. The estimated CL is represented in white.

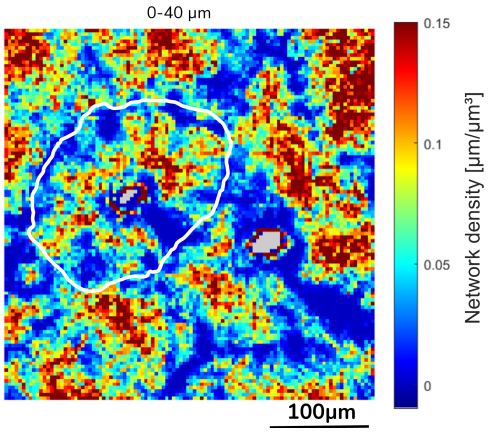

B: OsteonO. The estimated CL is represented in white.

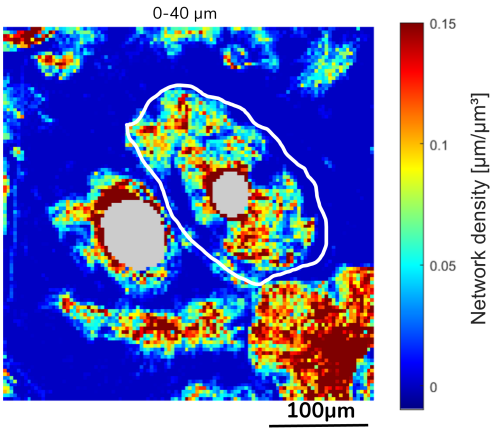

C: OsteonC. The estimated CL is represented in white.

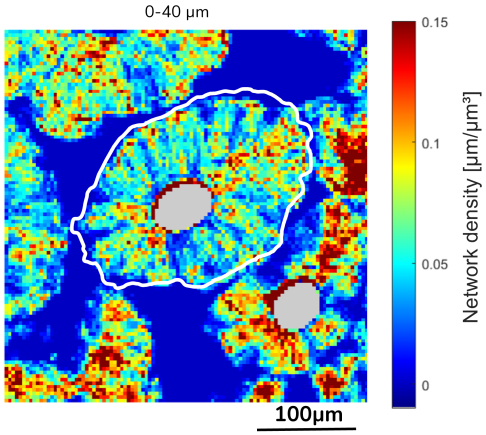

D: OsteonJ. The estimated CL is represented in white.

Figure 3.1: 2D density maps of the four osteons used in this study with a subvolume of 50 μm³. This figure is realized by taking the mean of the density over the z direction. The depth chosen here is 40 μm The density varies between 0 μm/μm³ (dark blue) and 0.15 (red) μm/μm³. The gray color represents the canals discarded from the analysis. All the analyzed osteons are bordered by their CLs, represented in white.

When examining osteonO on the left side of figure 3.1B, we perceive a significant presence of red zones. This osteon is quite asymmetric. However, there is a noticeable decrease in density at the presumed CL, but not within the osteon itself, even though connections with the surrounding osteon and IB are present. Surprisingly, there is a low-density zone near the canal. The network is dense, with few zero-density regions compared to other osteons. In this osteon, changes along the z-axis are not significant (Fig. 3.4). Another observation is that the canal is not very visible because the osteon is drifting. This drifting is probably the cause of the red color around the canal. The network is very sparse and the osteon is not connected everywhere.

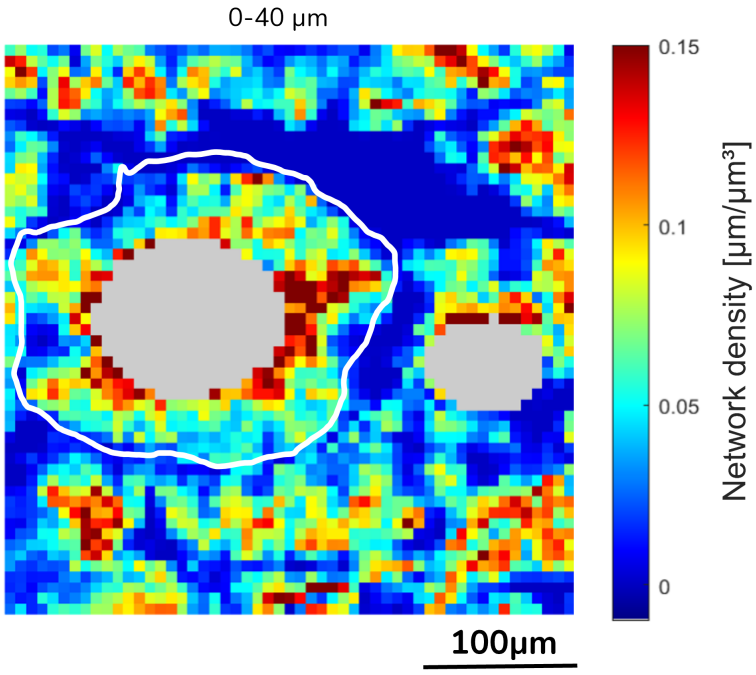

Figure 3.2: 2D density map of osteonG with a subvolume of 400 μm³. This figure is realized by taking the mean of the density over the z direction. The depth chosen here is 40 μm. The density varies between 0 μm/μm³ (dark blue) and 0.15 (red) μm/μm³. The gray color represents the canal discarded from the analysis. The estimated CL is represented in white.

In figure 3.1C, we observe a lack of network around the two osteons, with the osteon on the left appearing isolated. OsteonC, on the right, shows a ring of low density within it. In the first 10 μm, the weakness of the density network is evident. As we delve deeper along the z-axis, the density increases (Fig.3.5).

The figure 3.1D represents the osteonJ. Connections seem to appear at 20-30 μm (Fig.3.6) as can be seen with the white dotted squares.

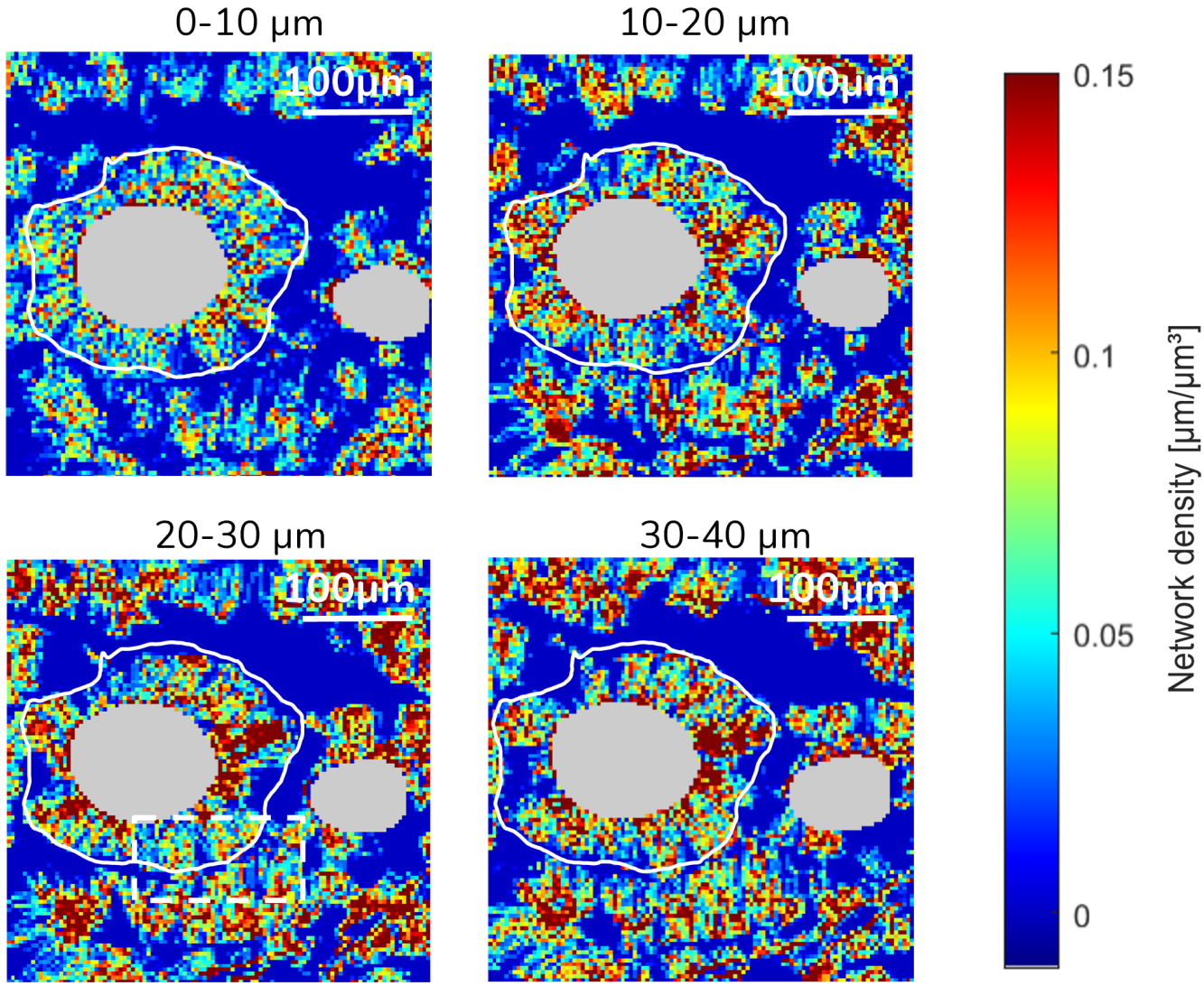

Figure 3.3: 2D density map of osteonG with a subvolume of 50 μm³. This figure is realized by taking the mean of the density over the z direction. The depth chosen here is 40 μm and is divided into 4 images with different depths (0-10 μm, 10-20 μm, 20-30 μm and 30-40 μm) to visualize the density over the z direction. The density varies between 0 μm/μm³ (dark blue) and 0.15 (red) μm/μm³. The gray color represents the canal discarded from the analysis. The white dotted rectangle shows the apparition of the connections with IB. The estimated CLs are represented in white.

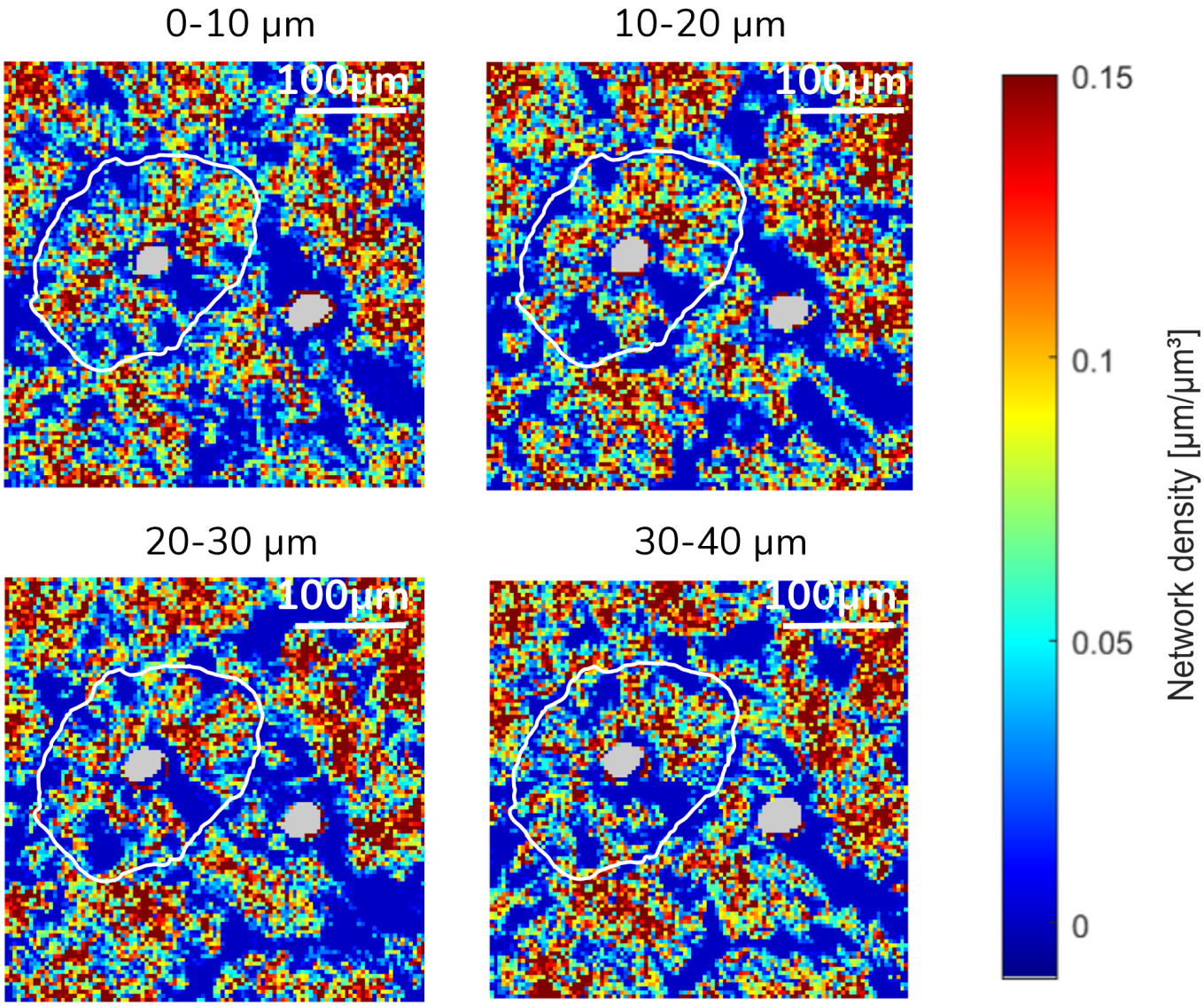

Figure 3.4: 2D density map of osteonO with a subvolume of 50 μm³. This figure is realized by taking the mean of the density over the z direction. The depth chosen here is 40 μm and is divided into 4 images with different depths (0-10 μm, 10-20 μm, 20-30 μm and 30-40 μm) to visualize the density over the z direction. The density varies between 0 μm/μm³ (dark blue) and 0.15 (red) μm/μm³. The gray color represents the canal discarded from the analysis. The estimated CLs are represented in white.

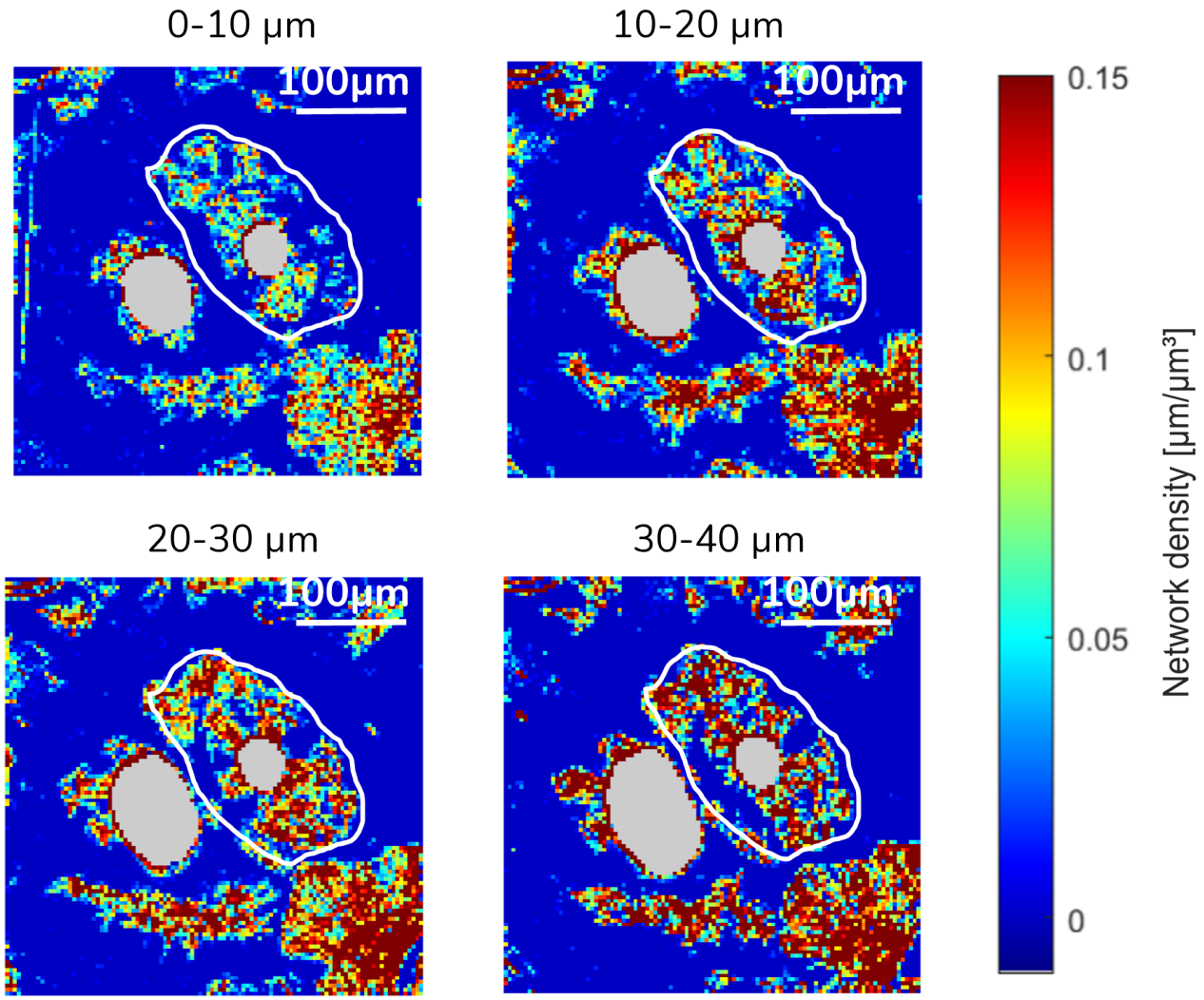

Figure 3.5: 2D density map of osteonC with a subvolume of 50 μm³. This figure is realized by taking the mean of the density over the z direction. The depth chosen here is 40 μm and is divided into 4 images with different depths (0-10 μm, 10-20 μm, 20-30 μm and 30-40 μm) to visualize the density over the z direction. The density varies between 0 μm/μm³ (dark blue) and 0.15 (red) μm/μm³. The gray color represents the canal discarded from the analysis. The estimated CLs are represented in white.

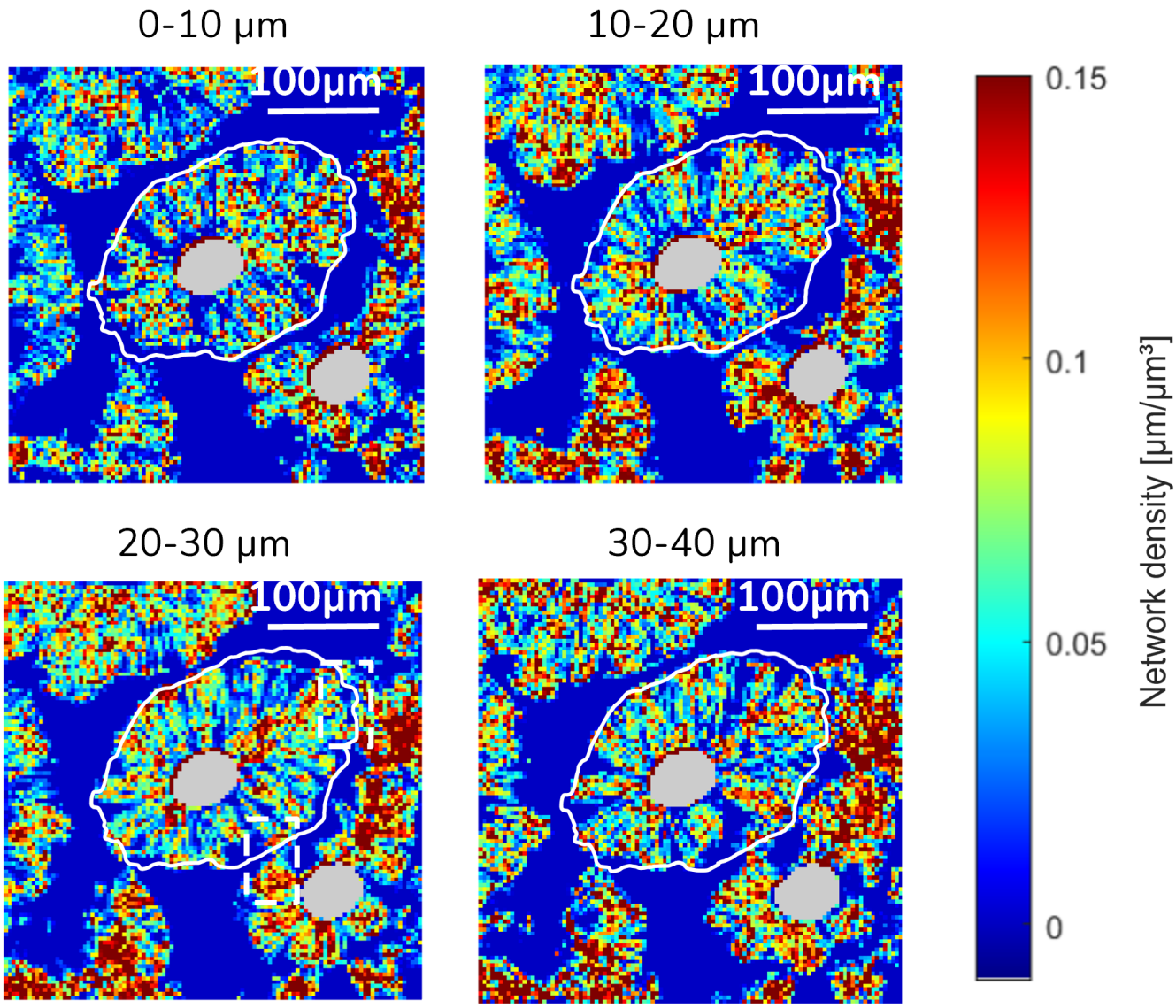

Figure 3.6: 2D density map of osteonJ with a subvolume of 50 μm³. This figure is realized by taking the mean of the density over the z direction. The depth chosen here is 40 μm and is divided into 4 images with different depths (0-10 μm, 10-20 μm, 20-30 μm and 30-40 μm) to visualize the density over the z direction. The density varies between 0 μm/μm³ (dark blue) and 0.15 (red) μm/μm³. The gray color represents the canal discarded from the analysis. The white dotted rectangles show the apparition of the connections with the other osteon on the bottom right and with the IB on the top right. The estimated CLs are represented in white.

3.1.2 Correlation degree/ density

In this section, we examine the correlation between the degree of connectivity and the network density. Figure 3.7 shows positive correlations for all the osteons, with the correlation coefficient R^2 values ranging between 0.36 and 0.64 and the p-value being 0.

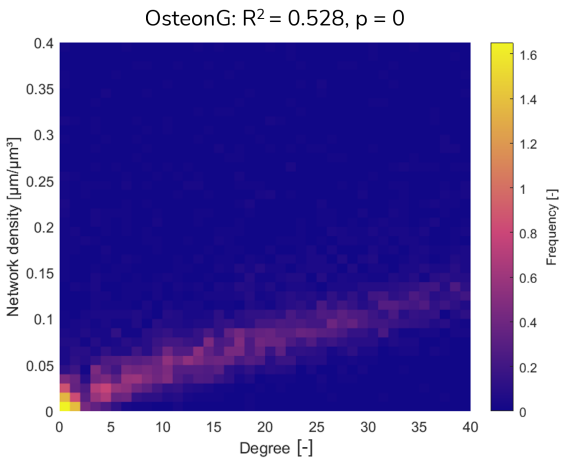

A: OsteonG.

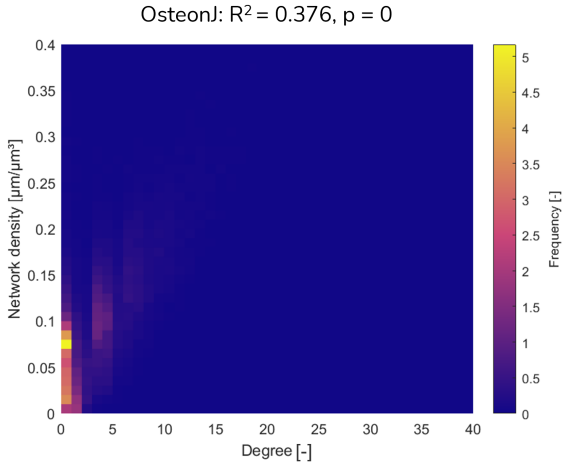

B: OsteonJ.

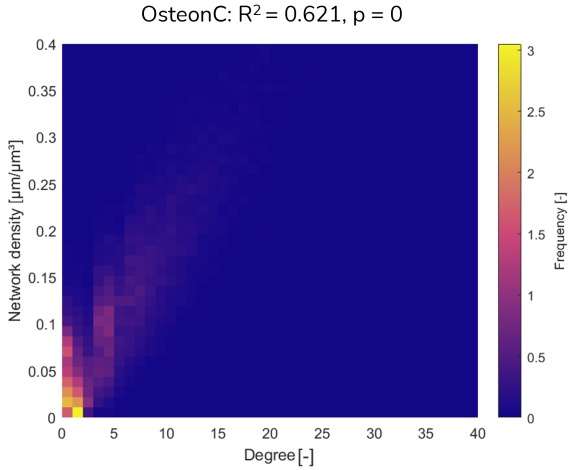

C: OsteonC.

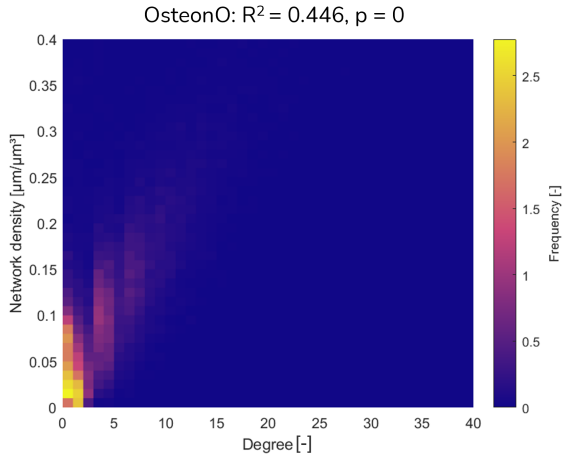

D: OsteonO.

Figure 3.7: The density of canaliculi [μm/μm³] related to the degree of connectivity for the four osteons with their corresponding names, R^2 and p-values. The colorbar shows the frequency.

3.1.3 Histograms of density

In figure 3.8, histograms of density within osteons are displayed. The highest bar on the far left corresponds to subvolumes devoid of any network. All the osteons show a peak before 0.1 μm/μm³, with this peak being the highest for osteonJ (Fig. 3.8B). All osteons have more low-density regions than high-density ones and the frequency decreases with increasing density in all cases.

We observe that the two osteons with lower mineral content (Fig. 3.8A and Fig. 3.8B)) have more smaller densities especially for osteonJ than the osteons with higher mineral content (Fig. 3.8C and Fig. 3.8D). Excluding the first bin, the highest frequency values are 0.005 for osteonC (Fig. 3.8C), 0.007 for osteonO (Fig. 3.8D), and they have a density value found close to 0 μm/μm³ while those for osteonJ (Fig. 3.8B) and osteonG (Fig. 3.8A) are respectively 0.014 and 0.008 and the density values are just before 0.1 μm/μm³.

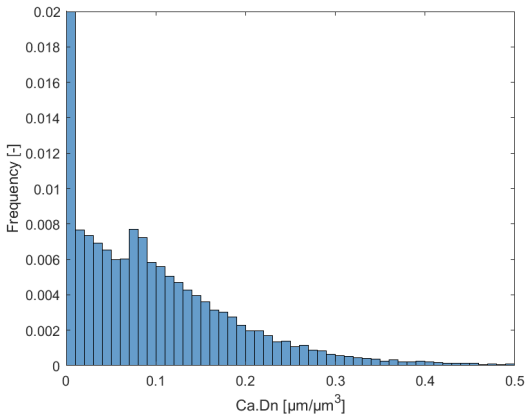

A: OsteonG.

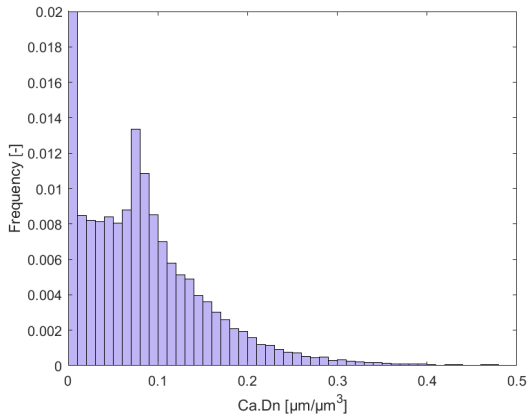

B: OsteonJ.

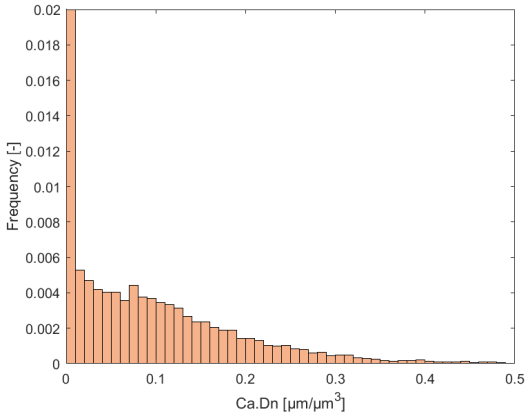

C: OsteonC.

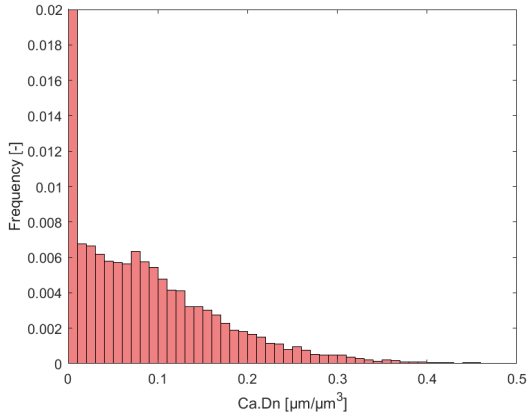

D: OsteonO.

Figure 3.8: Histograms of the density of the canaliculi within the osteons. OsteonG is in blue, osteonJ in purple, osteonC in orange, and osteonO in red. The frequency distributions of the canalicular density were evaluated with a bin width of about 0.01 μm/μm³ over a depth of 40 μm. The subvolume chosen here is 50 μm³.

3.1.4 Layers analysis

In this section, we evaluate the density of the canaliculi from two perspectives as described in the method. The first perspective examines the density starting from the CL and moving through the osteon to the Haversian canal. The second perspective observes the change in density from the Haversian canal to the CL.

These figures are plots with confidence intervals, where the central line represents the mean, and the shaded area represents the confidence interval around this mean. The points with error bars indicate individual measurements along with their uncertainties.

We will begin the analysis with plots of the layers, starting at the CL and extending to the Haversian canal.

Figure 3.9A displays the results for osteonG. It clearly illustrates a gradual increase in density, with the mean value at the CL being the lowest (0.035 μm/μm³), and the mean of the closest layer to the Haversian canal (the last layer analyzed) being the highest (0.067 μm/μm³). The increase follows a linear trend, with the highest value below 0.15 μm/μm³. Another observation is that all mean values are around 0.05 μm/μm³. These means are detailed in table 3.1.

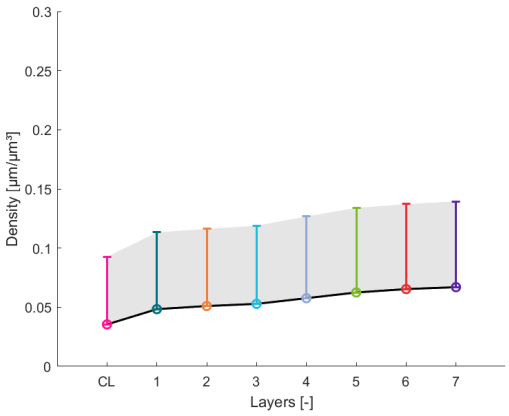

A: OsteonG.

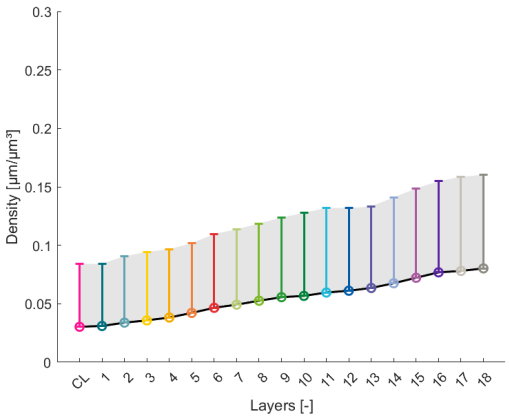

B: OsteonO.

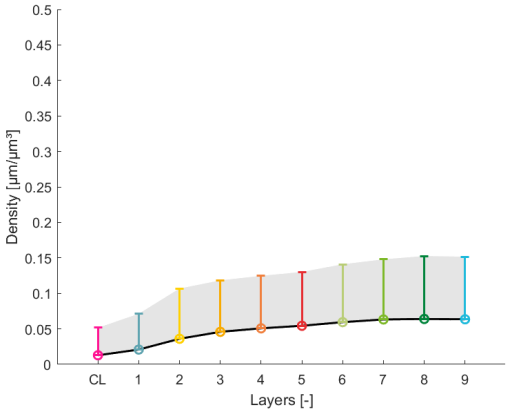

C: OsteonC.

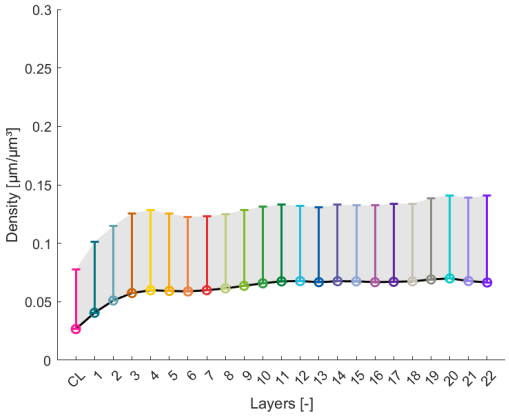

D: OsteonJ.

Figure 3.9: Density mean and standard deviation mean of the canaliculi with corresponding error bars for each layer within the osteons. The evaluation of the density of the canaliculi starts at the CL until reaching the Haversian canal. The thickness of the layers is 5 pixels.

-	Density mean ± std [μm/μm³]
CL	0.035 ± 0.06
Layer 1	0.051 ± 0.06
Layer 2	0.048 ± 0.06
Layer 3	0.053 ± 0.07
Layer 4	0.058 ± 0.07
Layer 5	0.062 ± 0.07
Layer 6	0.065 ± 0.07
Layer 7	0.067 ± 0.07

Table 3.1: Density mean of the canaliculi for each layer of the osteonG starting at the CL.

In figure related to osteonO (Fig.3.9B), similar observations can be made. There is a linear increase, with the mean value at the CL being the lowest (0.030 μm/μm³), and the mean of the closest layer to the Haversian canal (the last layer analyzed) being the highest (0.080 μm/μm³). The highest value of density in this osteon is above 0.15 μm/μm³. In this case as well, all mean values are approximately around 0.05 μm/μm³. Detailed mean values can be found in table 3.2.

-	Density mean ± std[μm/μm³]
CL	0.030 ± 0.05
Layer 1	0.031 ± 0.05
Layer 2	0.034 ± 0.06
Layer 3	0.036 ± 0.06
Layer 4	0.038 ± 0.06
Layer 5	0.042 ± 0.06
Layer 6	0.047 ± 0.06
Layer 7	0.049 ± 0.06
Layer 8	0.053 ± 0.07
Layer 9	0.056 ± 0.07
Layer 10	0.057 ± 0.07
Layer 11	0.060 ± 0.07
Layer 12	0.061 ± 0.07
Layer 13	0.063 ± 0.07
Layer 14	0.068 ± 0.07
Layer 15	0.072 ± 0.08
Layer 16	0.077 ± 0.08
Layer 17	0.078 ± 0.08
Layer 18	0.080 ± 0.08

Table 3.2: Density mean of the canaliculi for each layer of the osteonO starting at the CL.

Similarly, the findings for osteonC (Fig.3.9C) are consistent. The highest value, as observed in osteonO, exceeds 0.15 μm/μm³ . The mean at the CL, which is the lowest mean value, stands at 0.0128 μm/μm³ (refer to table 3.3).

-	Density mean ± std [μm/μm³]
CL	0.013 ± 0.04
Layer 1	0.021 ± 0.05
Layer 2	0.036 ± 0.07
Layer 3	0.046 ± 0.07
Layer 4	0.051 ± 0.07
Layer 5	0.054 ± 0.07
Layer 6	0.059 ± 0.08
Layer 7	0.063 ± 0.08
Layer 8	0.064 ± 0.09
Layer 9	0.063 ± 0.09

Table 3.3: Density mean of the canaliculi for each layer of the osteonC starting at the CL.

For osteonJ (Fig.3.9D), we observe an increase of the density that is not linear. The mean at the CL is the lowest value (0.027 μm/μm³), and similar to osteonG, the maximum density value remains below 0.15 μm/μm³. Additionally, the means are clustered around 0.05 μm/μm³ (see table 3.4).

-	Density mean ± std [μm/μm³]
CL	0.027 ± 0.05
Layer 1	0.040 ± 0.06
Layer 2	0.051 ± 0.06
Layer 3	0.057 ± 0.07
Layer 4	0.060 ± 0.07
Layer 5	0.059 ± 0.07
Layer 6	0.059 ± 0.06
Layer 7	0.060 ± 0.06
Layer 8	0.061 ± 0.06
Layer 9	0.064 ± 0.06
Layer 10	0.066 ± 0.06
Layer 11	0.067 ± 0.06
Layer 12	0.068 ± 0.06
Layer 13	0.067 ± 0.06
Layer 14	0.067 ± 0.06
Layer 15	0.067 ± 0.06
Layer 16	0.067 ± 0.06
Layer 17	0.067 ± 0.07
Layer 18	0.067 ± 0.07
Layer 19	0.069 ± 0.07
Layer 20	0.070 ± 0.07
Layer 21	0.068 ± 0.07
Layer 22	0.066 ± 0.07

Table 3.4: Density mean of the canaliculi for each layer of the osteonJ starting at the CL.

Comparing the four osteons, we find that the mean density at the CL is consistently lowest across all osteons, with osteonC showing the lowest mean and osteonG the highest. The density increase is nonlinear only in the case of osteonJ which is in accordance with the density maps where the distribution of the density is uniform. Furthermore, osteonG and osteonJ, which exhibit lower mineral content, have a maximum density value below 0.15 μm/μm³, whereas the other two osteons have a maximum value above 0.15 μm/μm³.

Moving to the reverse analysis starting at the canal and ending at the CL, for osteonG (Fig. 3.10A), we observe a consistent nonlinear decrease in density, with the lowest mean value at the CL (0.035 μm/μm³). The highest density value is found in the first layer closest to the canal, reaching 0.5 μm/μm³. All the mean values are repertoried in table 3.5.

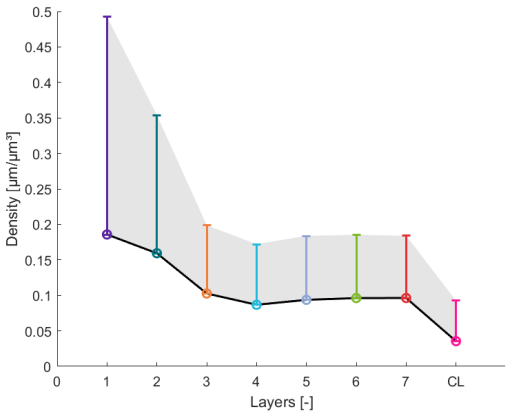

A: OsteonG.

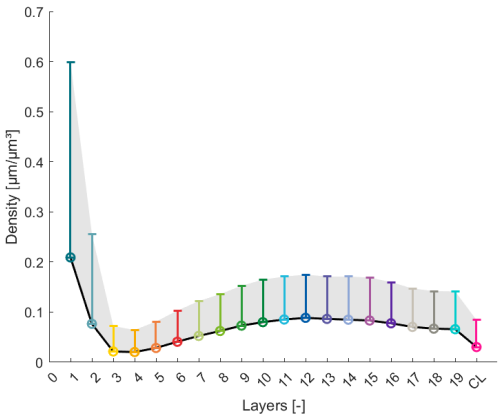

B: OsteonO.

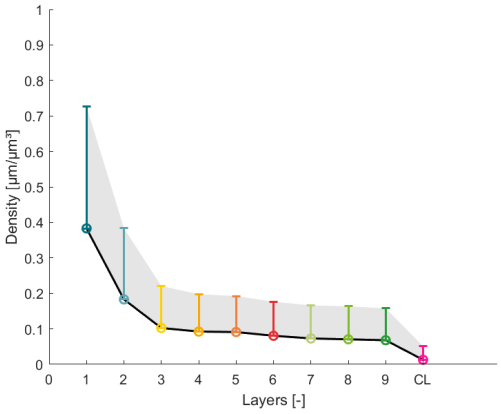

C: OsteonC.

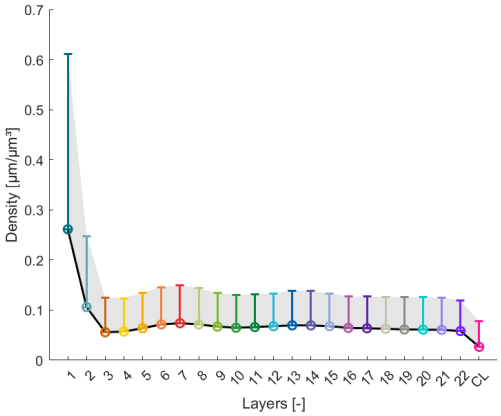

D: OsteonJ.

Figure 3.10: Density mean and standard deviation mean of the canaliculi with corresponding error bars for each layer within the osteons. The evaluation of the density of the canaliculi starts at the Haversian canal until reaching the CL. The thickness of the layers is 5 pixels.

-	Density mean ± std [μm/μm³]
Layer 1	0.186 ± 0.30
Layer 2	0.159 ± 0.20
Layer 3	0.103 ± 0.10
Layer 4	0.087 ± 0.08
Layer 5	0.094 ± 0.09
Layer 6	0.096 ± 0.09
Layer 7	0.096 ± 0.09
CL	0.035 ± 0.06

Table 3.5: Density mean of the canaliculi for each layer of the osteonG starting at the Haversian canal.

In the case of osteonO (Fig.3.10B), we also see a density decrease after the canal, followed by a slight increase before decreasing again. Interestingly, the lowest mean value is not at the CL (0.030 μm/μm³), but rather at the fourth layer (0.020 μm/μm³). Similar to osteonG, the highest density value is observed in the first layer after the canal, reaching 0.6 μm/μm³. The mean values can be found in table 3.6.

-	Density mean ± std [μm/μm³]
Layer 1	0.209 ± 0.39
Layer 2	0.076 ± 0.18
Layer 3	0.021 ± 0.05
Layer 4	0.020 ± 0.04
Layer 5	0.028 ± 0.05
Layer 6	0.041 ± 0.06
Layer 7	0.052 ± 0.07
Layer 8	0.062 ± 0.07
Layer 9	0.073 ± 0.08
Layer 10	0.080 ± 0.08
Layer 11	0.085 ± 0.08
Layer 12	0.088 ± 0.09
Layer 13	0.086 ± 0.08
Layer 14	0.085 ± 0.09
Layer 15	0.083 ± 0.08
Layer 16	0.078 ± 0.08
Layer 17	0.070 ± 0.08
Layer 18	0.067 ± 0.07
Layer 19	0.066 ± 0.07
CL	0.030 ± 0.05

Table 3.6: Density mean of the canaliculi for each layer of the osteonO starting at the Haversian canal.

In the case of the osteonC (see Fig.3.10C), we also observe a consistent nonlinear decrease in density, similar to osteonG. The mean density of the CL is the lowest at 0.0128 μm/μm³ which can be consistent with the 2D maps where the osteonC seems to be isolated (*i.e.*, weak number of connections), and the highest value of the density occurs in the first layer at 0.7 μm/μm³. The mean values are reported in table 3.7.

-	Density mean ± std [μm/μm³]
Layer 1	0.383 ± 0.34
Layer 2	0.183 ± 0.20
Layer 3	0.102 ± 0.12
Layer 4	0.092 ± 0.10
Layer 5	0.091 ± 0.10
Layer 6	0.080 ± 0.09
Layer 7	0.073 ± 0.09
Layer 8	0.070 ± 0.09
Layer 9	0.068 ± 0.09
CL	0.013 ± 0.04

Table 3.7: Density mean of the canaliculi for each layer of the osteonC starting at the Haversian canal.

OsteonJ (Fig.3.10D) exhibits similarities to osteonG. However, the density does not really decrease until reaching the CL, which has the lowest mean value (0.026 μm/μm³). Again, the highest density value is found in the first layer closest to the canal, reaching 0.6 μm/μm³. In the curve, we can perceive a plateau between 0 μm/μm³ and 0.15 μm/μm³ for layer 3 until layer 22. Following this plateau there is a drop at the CL. This plateau is in accordance with the 2 maps where the density is uniformly distributed. In addition, the variability in each layer is constant and weaker than in the layers of osteonO where this variability increases with the layers. We also note that the CL is the layer with the least variability.

-	Density mean ± std [μm/μm³]
Layer 1	0.261 ± 0.35
Layer 2	0.106 ± 0.14
Layer 3	0.056 ± 0.07
Layer 4	0.057 ± 0.07
Layer 5	0.064 ± 0.07
Layer 6	0.071 ± 0.07
Layer 7	0.074 ± 0.07
Layer 8	0.071 ± 0.07
Layer 9	0.067 ± 0.07
Layer 10	0.065 ± 0.06
Layer 11	0.066 ± 0.06
Layer 12	0.068 ± 0.06
Layer 13	0.070 ± 0.07
Layer 14	0.069 ± 0.07
Layer 15	0.068 ± 0.06
Layer 16	0.064 ± 0.06
Layer 17	0.064 ± 0.06
Layer 18	0.063 ± 0.06
Layer 19	0.061 ± 0.06
Layer 20	0.061 ± 0.06
Layer 21	0.060 ± 0.06
Layer 22	0.058 ± 0.06
CL	0.027 ± 0.05

Table 3.8: Density mean of the canaliculi for each layer of the osteonJ starting at the Haversian canal.

When comparing all four osteons in this context, osteonC exhibits the highest density value of 0.7 μm/μm³ (Fig.3.10C). In all osteons, there is a general trend of decreasing density. However, osteonO (Fig.3.10B) shows a slight increase in density before decreasing again and osteonJ (Fig.3.10D) presents a kind of plateau for the density which decreases at the CL. The CL is not the lowest value only in osteonO (Fig.3.10B) which may be surprising.

3.1.5 Orientation

In all osteons, we observe similar characteristics. Each osteon consists of blue canaliculi radiating towards its center. At the periphery, the canaliculi are perpendicular to the radial direction, meaning they run parallel to the Haversian canal or within the image plane as can be seen in figure 3.11 . The color code for the orientation of the canaliculi is calculated in relation to the center of the Haversian canal. Therefore, we have to be careful because we cannot trust the color code outside the osteon.

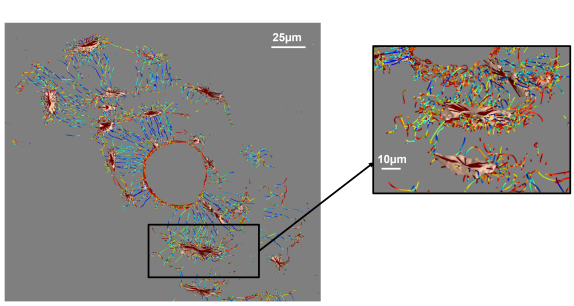

A: OsteonC.

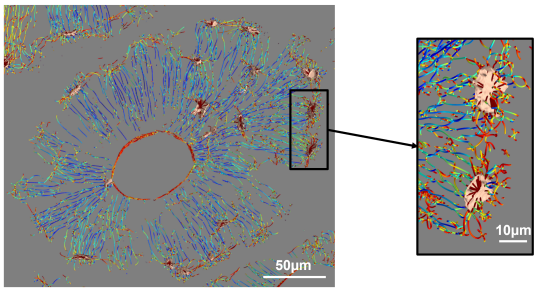

B: OsteonJ.

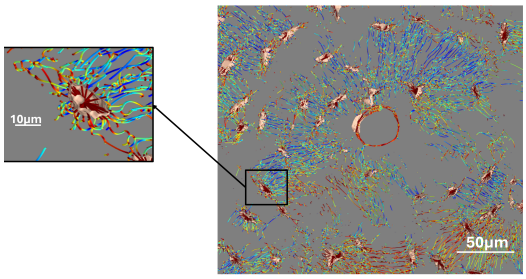

C: OsteonO.

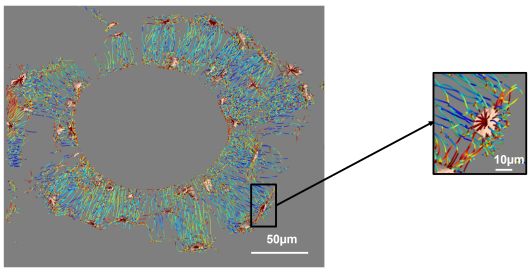

D: OsteonG.

Figure 3.11: Visualization of the orientation of the canaliculi of the osteons. This visualization is made using the tool MayaVi and is represented in the Z plane. The canaliculi in blue run radially (θ between 0 and 30°) toward the center which is the Haversian canal while the canaliculi in red run parallel to the Haversian canal or within the image plane. The zooms show the canaliculi in red at the CL. This zoom in is in another plane for osteonC (Fig. 3.11A) and osteonJ (Fig. 3.11B) to ensure the good visualization of the red canaliculi.

However, there are some specific features in different osteons. OsteonC has two prominent rings of lacunae within it (Fig.3.11A) . The network is mainly disrupted at the CL, but there are some connections with the IB (Fig.3.12).

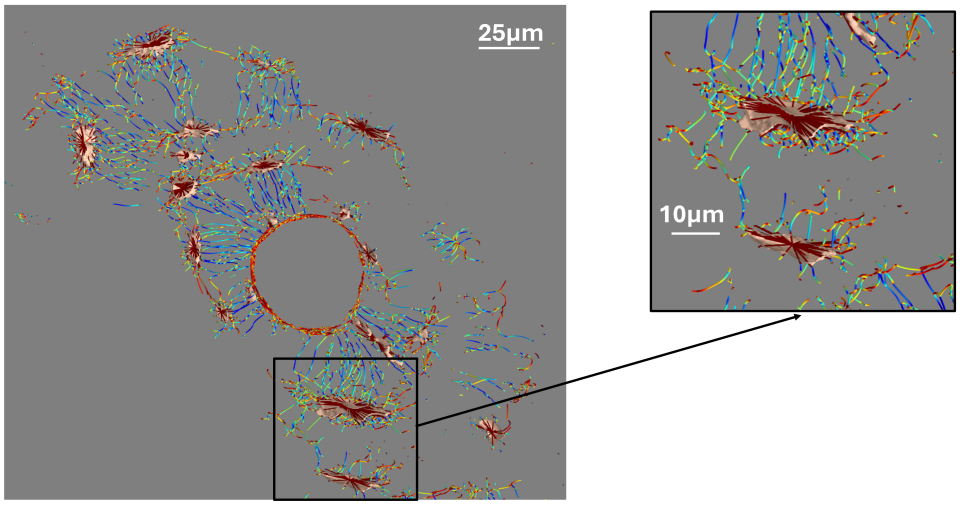

Figure 3.12: Visualization of the orientation of the canaliculi of the osteonC. This vizualisation is made using the tool MayaVi and is represented in the Z plane. The canaliculi in blue run radially (θ between 0 and 30°) toward the center which is the Haversian canal while the canaliculi in red run parallel to the Haversian canal or within the image plane. The zoom shows the network disrupted at the CL.

In osteonO, we observe yellow canaliculi within the osteon and a red area surrounding it. This osteon is

connected to the adjacent osteon (Fig.3.13).

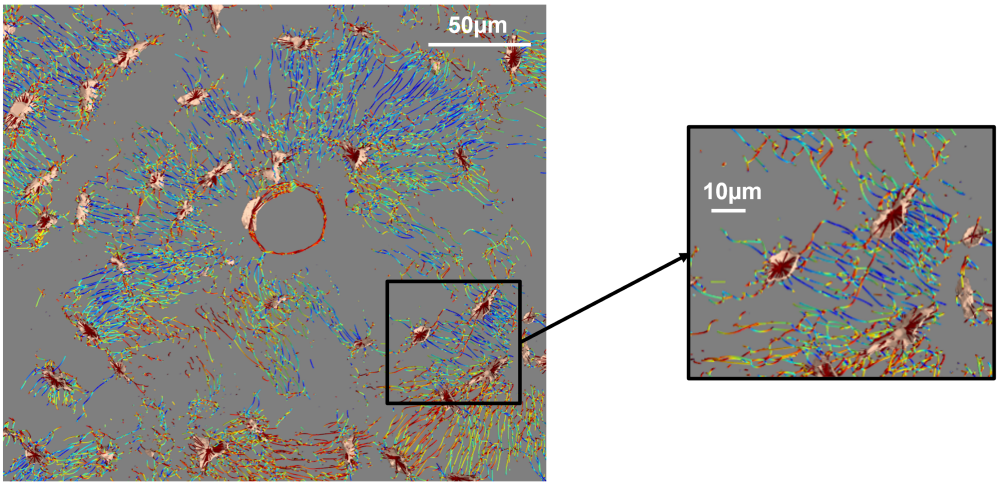

Figure 3.13: Visualization of the orientation of the canaliculi of the osteonO. This vizualisation is made using the tool MayaVi and is represented in the Z plane. The canaliculi in blue run radially (θ between 0 and 30°) toward the center which is the Haversian canal while the canaliculi in red run parallel to the Haversian canal or within the image plane. The zoom shows the connection with the other osteon.

For osteonG, yellow canaliculi are also present within the osteon. Additionally, there is a clear connection to the surrounding bone, where the canaliculi are blue (Fig.3.14). We also notice a connection with another osteon as can be seen in figure 3.15.

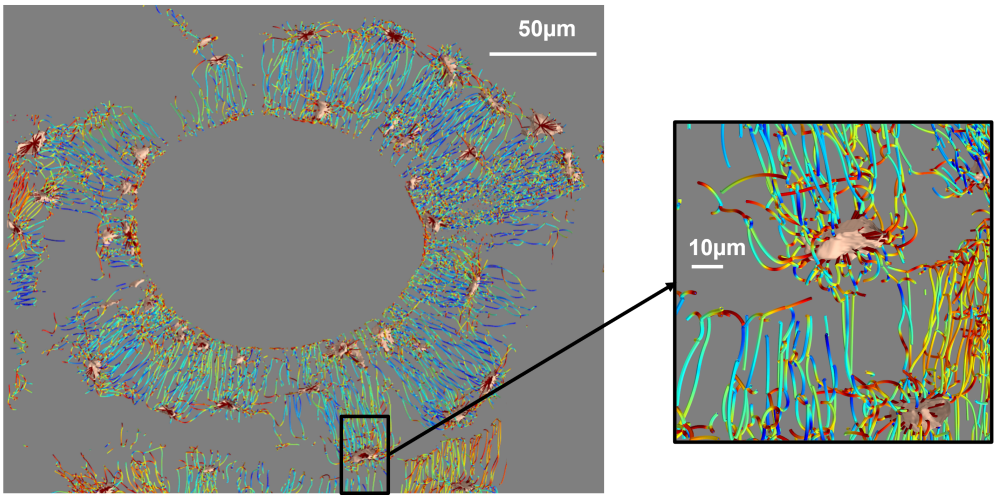

Figure 3.14: Visualization of the orientation of the canaliculi of the osteonG. This vizualisation is made using the tool MayaVi and is represented in the Z plane. The canaliculi in blue run radially (θ between 0 and 30°) toward the center which is the Haversian canal while the canaliculi in red run parallel to the Haversian canal or within the image plane. The zoom shows the connection with IB.

In osteonO, osteonJ, and osteonC, the Haversian canal contains red canaliculi, whereas this is not observed in osteonG. The reason for this difference will be explained in the discussion.

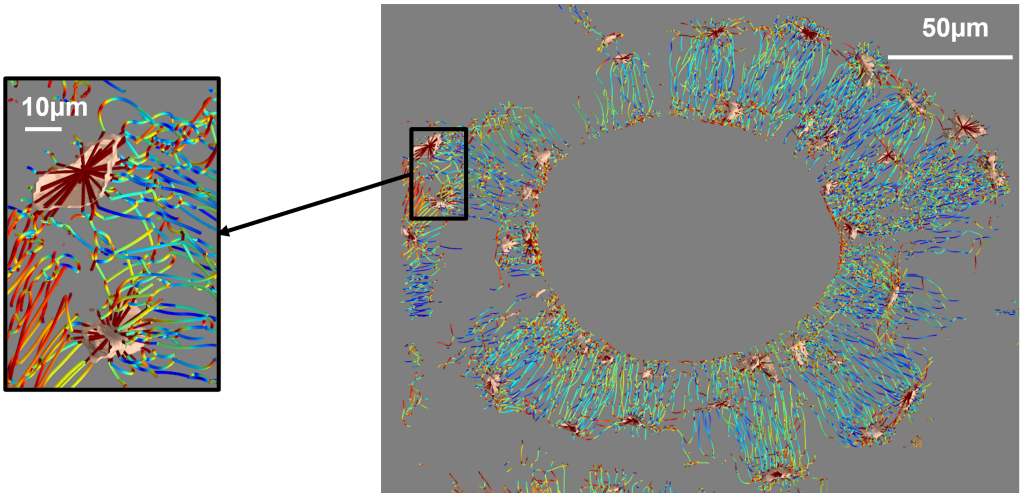

Figure 3.15: Visualization of the orientation of the canaliculi of the osteonO. This vizualisation is made using the tool MayaVi and is represented in the Z plane. The canaliculi in blue run radially (θ between 0 and 30°) toward the center which is the Haversian canal while the canaliculi in red run parallel to the Haversian canal or within the image plane. The zoom shows the connection with another osteon.

3.2 Cells

When examining the cells, we see the volume of the lacunae related to the calcium content in figure 3.16. However, there is no clear correlation between these two properties. The highest average volume is observed in osteonC with 797 $\pm$ 271 μm³ , followed by osteonO with 481 $\pm$ 667 μm³. The difference between osteonC and osteonO is not significant, but these values are significantly different from the other two osteons. Therefore, the volume of the lacunae in osteons with high calcium content is higher and significantly different from that in osteons with low calcium content. The lowest mean volume is found in osteonG with a value of 171 $\pm$ 249 μm³ and the mean value of the osteonJ is 265$\pm$ 459 μm³.

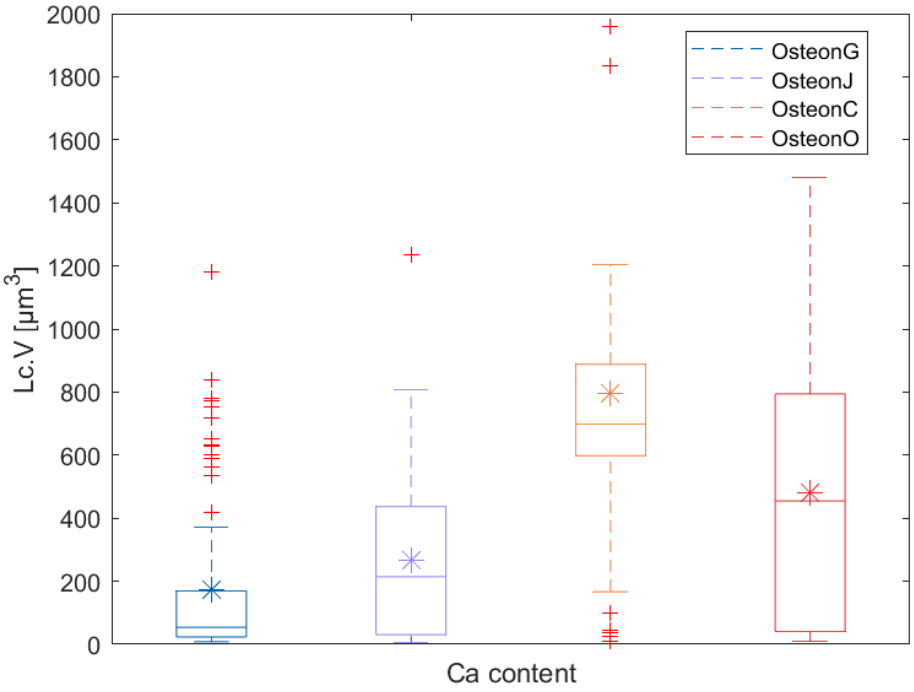

Figure 3.16: Lacunae volume [μm³] related to the calcium content. OsteonG is in blue, osteonJ in purple, osteonC in orange, and osteonO in red. The means are represented by the stars, the medians are the horizontal bars and the boxplots show the data distribution.

Figure 3.17 depicts the stretching (*i.e.*, elongation) of the lacunae relative to the calcium content. There is a slight increase in lacunae elongation with higher calcium content, but this trend is not statistically significant. The highest average elongation is observed in osteonC, with a value of 0.666 $\pm$ 0.14, which is comparable to osteonO (0.656 $\pm$ 0.09). The lowest average elongation is found in osteonG, with a value of 0.608 $\pm$ 0.14. The mean of the stretching are around 0.6.

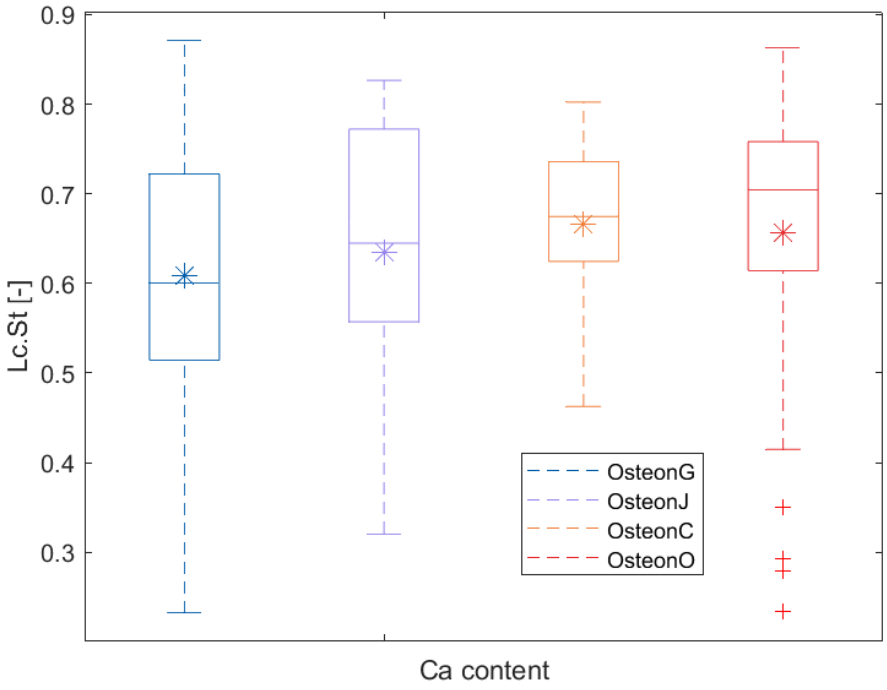

Figure 3.17: Lacunae stretch related to the calcium content. OsteonG is in blue, osteonJ in purple, osteonC in orange, and osteonO in red. The means are represented by the stars, the medians are the horizontal bars and the boxplots show the data distribution.

The evaluation of oblateness with respect to the calcium content reveals no trend (Fig.3.18). This property is relatively the same for each osteon, though it is slightly higher for osteonC.

OsteonC differs significantly from osteonO and osteonG, with a mean value of -0.002 $\pm$ 0.43, whereas osteonO, osteonG, and osteonJ have mean values of -0.230 $\pm$ 0.42, -0.211 $\pm$0.42, and -0.154 $\pm$ 0.39, respectively. The differences between these three are not significant. There appears to be a lot of variability in all the osteons, with most values between -0.5 and 0.

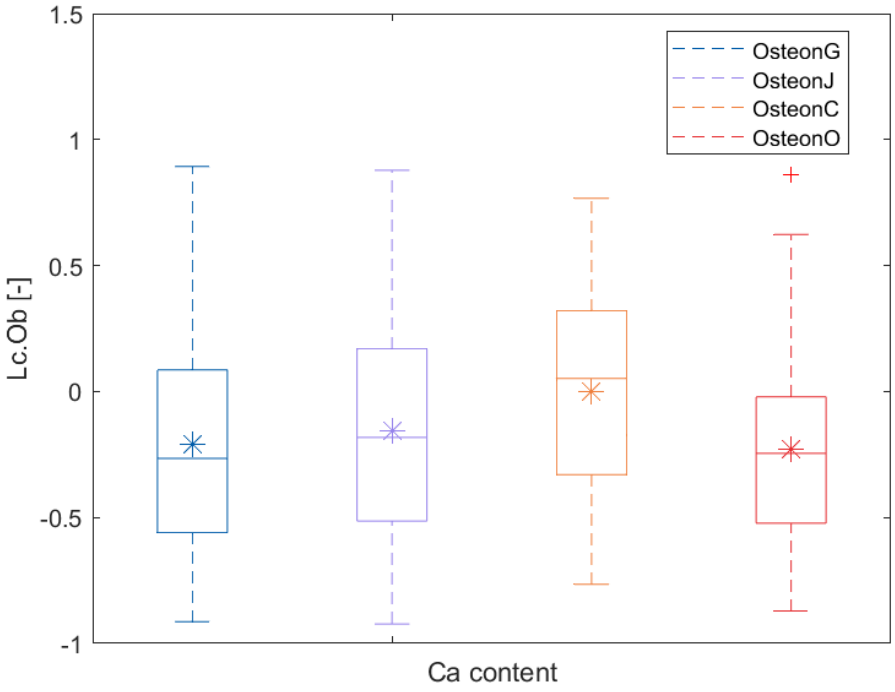

Figure 3.18: Lacunae oblateness related to the calcium content. OsteonG is in blue, osteonJ in purple, osteonC in orange, and osteonO in red. The means are represented by the stars, the medians are the horizontal bars and the boxplots show the data distribution.

We investigated the relationship between lacuna volume and oblateness (Fig.3.19). No correlation was found between these two parameters.

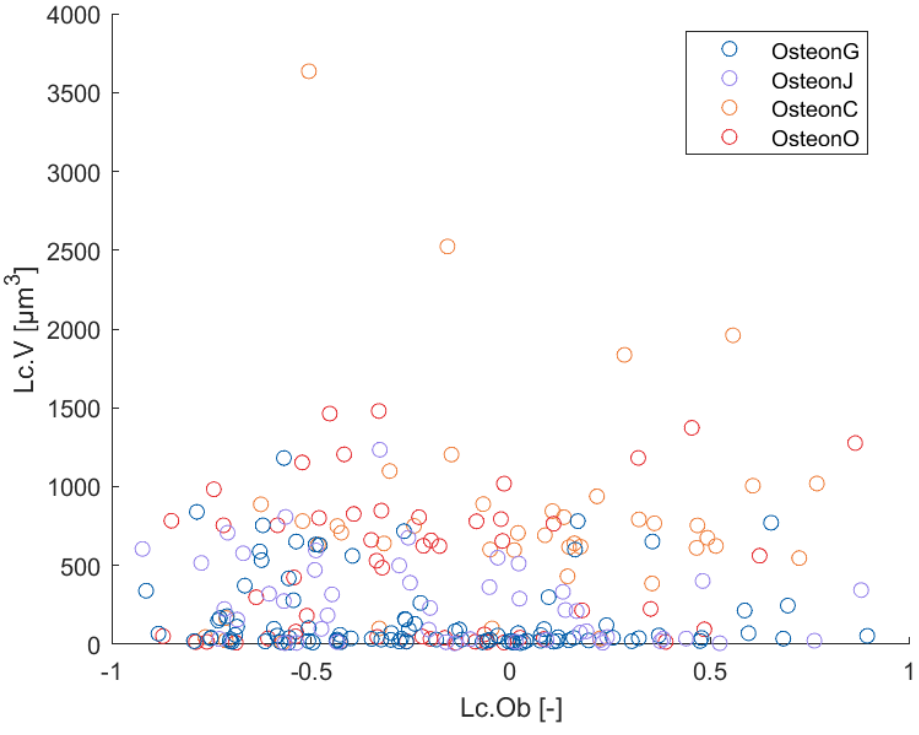

Figure 3.19: Lacunae volume [μm³] related to the lacunae oblateness. OsteonG is in blue, osteonJ in purple, osteonC in orange and osteonO in red.

In figure 3.20, we observe an even distribution of oblateness, stretching, and volume as a function of the distance from the center of the Haversian canal, meaning that no correlation was found.

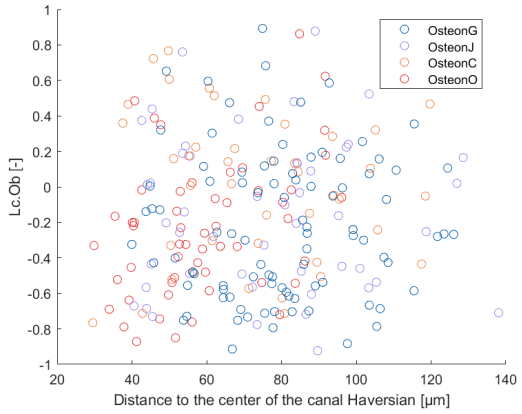

A: The oblateness of the lacunae as a function of the distance [μm] from the center of the Haversian canal.

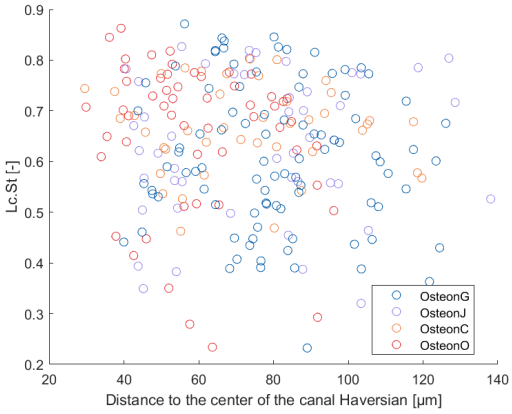

B: The stretching of the lacunae as a function of the distance [μm] from the center of the Haversian canal.

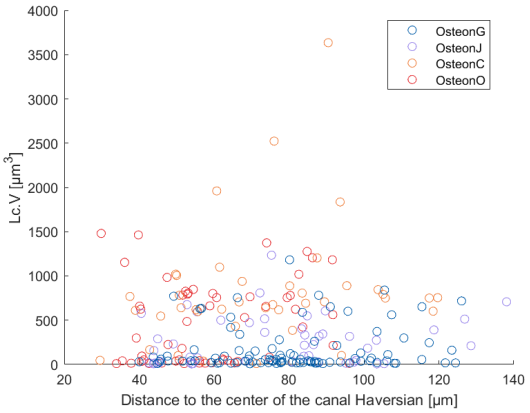

C: The volume of the lacunae [μm³] as a function of the distance [μm] from the center of the Haversian canal.

Figure 3.20: The oblateness, the stretching and the volume [μm³] of the lacunae as a function of the distance from the center of the Haversian canal [μm]. OsteonG is in blue, osteonJ in purple, osteonC in orange and osteonO in red.

We also qualitatively examined the cell density (Fig.3.21). In this figure of osteonJ (Fig.3.21A), we can observe a high number of lacunae near the CL.

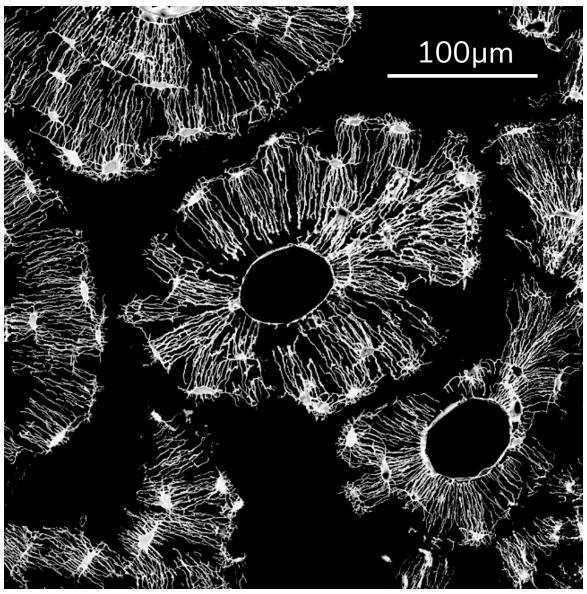

A: OsteonJ.

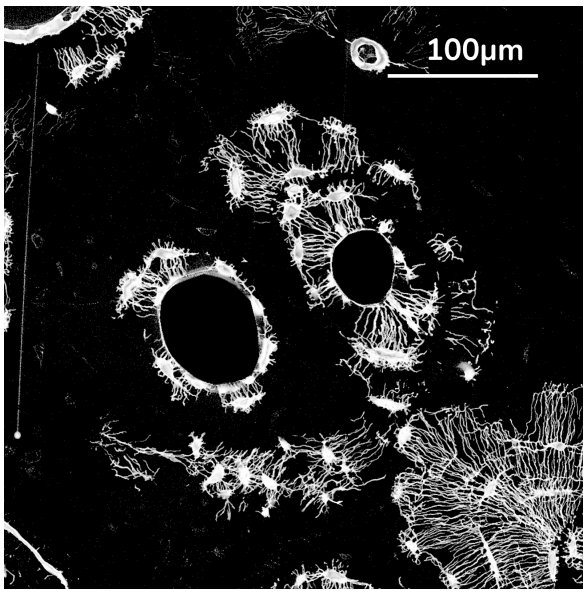

B: OsteonC.

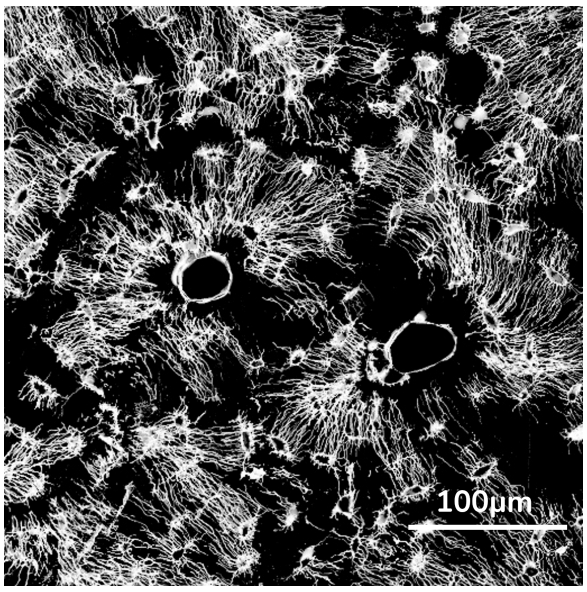

C: OsteonO.

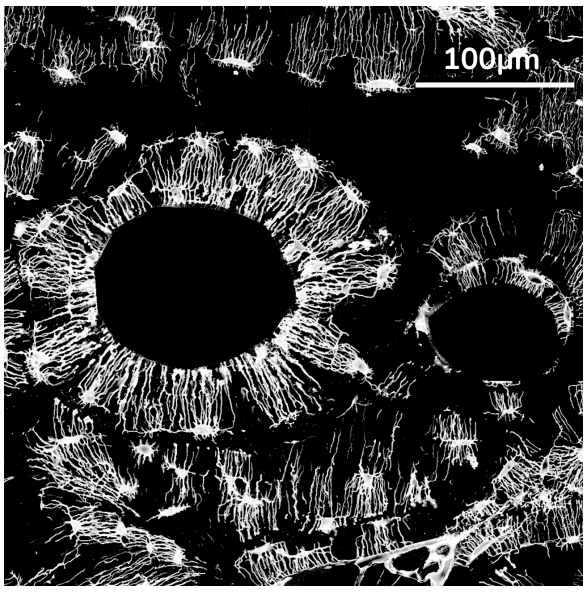

D: OsteonG.

Figure 3.21: Z projection of the CLS of the osteons with a depth of approximately 12 μm which corresponds to 50 slices.

In the case of the osteonC which is an osteon of type II, we perceive two rings of lacunae and these rings are located at the CLs (Fig.3.21B).

In osteonO, there seems to have more lacunae where there is a possible connection with IB at the top left (Fig.3.21C). In addition, there seems to be a lack of cells close to the canal. Lacunae in osteonG seem to be more uniformly distributed (Fig.3.21D).

Chapter 4

Discussion

The aim of this chapter is to discuss the previous results to understand the connections between the osteon and its surrounding environment, and the behavior of the canaliculi and cells. This chapter also presents the limitations of the study and future perspectives for further research.

4.1 Canaliculi

4.1.1 OsteonG

Regarding the first osteon, (*i.e.*, osteonG), the density decreases from the Haversian canal to the osteon border, as observed by Repp et al. [6]. There is a significant heterogeneity within the osteon [112].

The layer analysis confirms the observations in the 2D map by indicating that density decreases from the Haversian canal to the CL, with the CL having the lowest mean density. This value is higher than zero, indicating some connectivity with other osteons/surrounding bone. The layer immediately after the canal has the highest density, which aligns with the findings of Repp et al. [6]. However, this value is unusually high and differs significantly from the others. This can be explained by the penetration of rhodamine into the canal. During segmentation, the borders of the canal are likely included, leading to an artificially high density.

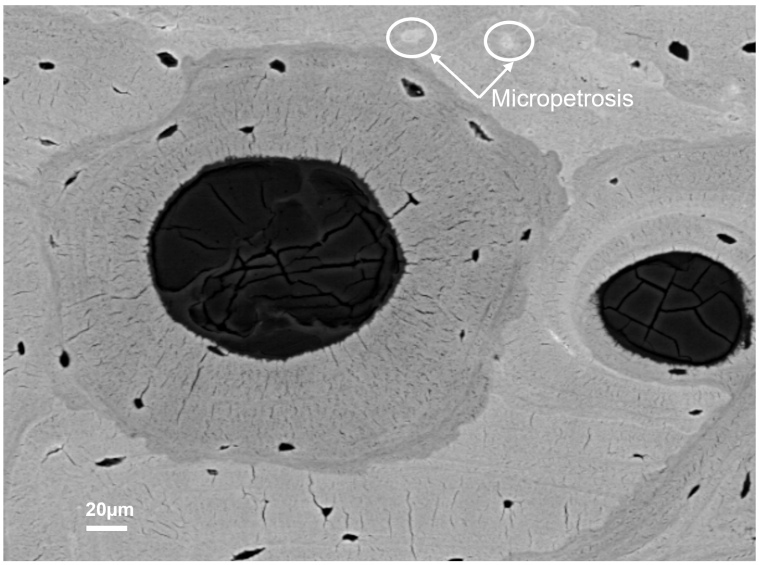

Figure 4.1: qBEI image of osteonG. The micropetrosis are highlighted with the white circle.

There is a large area with zero densities in the IB, but we cannot be certain there is no network in this region, as rhodamine may not penetrate this area. Indeed, rhodamine penetrates all accessible canaliculi and binds

to the walls of the mineralized extracellular matrix, enabling visualization with CLSM [50]. Therefore, no network observed does not necessarily mean that it does not exist. If we analyze the qBEI image of osteonG (Fig.4.1), we can observe that the zero-density area at the top right of the 2D maps (Fig.3.1A) aligns with our observations from the qBEI image. There are white cells which correspond to micropetrosis, (*i.e.*, lacunae filled with minerals following osteocyte) that we can observe in figure 4.1 [113]. The death of osteocytes can be associated with areas of secondary calcification. After cell death, the spaces once occupied by osteocytes can be filled with mineral deposits, appearing brighter on the qBEI image. Indeed, osteocyte death can lead to changes in the structure and composition of the lacunae, resulting in an increase in mineral density in and around these spaces, making them more visible (*i.e.*, white) on the image [114].

There also seems to be a periodic alternation between low densities and high densities in the azimuthal direction. This variation is not reflected in the qBEI images. Indeed the calcium content in qBEI images is quite homogeneous everywhere whereas the network is quietly heterogeneous as seen in the density maps.

4.1.2 OsteonO

In osteonO, it was also observed that the density of the canaliculi decreases as it approaches the CL [6]. However, this decrease is not clearly visible in the 2D maps of the osteons. Nevertheless, this observation is supported by the layer studies. The mean density of the CL is close to zero and is not the lowest mean value, possibly due to the presence of a very low-density area near the canal. There appears to be another CL from the qBEI image close to the canal, which could explain the lower canalicular density in this region. This CL appears whiter than the osteon in the qBEI, consistent with the higher mineral content of the CL compared to the osteon [112]. Therefore, it is possible that this osteon is an osteon of type II, (*i.e.*, an osteon-in-osteon), which could be consistent with the supposed CL inside the osteon analyzed.

This osteon also exhibits significant heterogeneity, as observed in similar studies [112] and in the other osteons of this study.

Additionally, when regarding the qBEI image, the osteon is next to another osteon and it seems that the two osteons are connected together as observed in the density map (Fig. 3.1B). The mean value of the CL, which is not higher than zero, can be explained by the numerous connections of this osteon with other osteon and IB. These connections are visible on the 2D maps as regions with non-zero densities. In this case, the layer immediately after the Haversian canal also shows the highest value, which may also be an artifact, as discussed earlier. To avoid the red value around the canal, its mask should be dilated a bit more.

As for osteonG, there seems to have a periodic alternation between low densities and high densities in the azimuthal direction, but this is again not reflected in the qBEI images.

4.1.3 OsteonJ

In the 2D map of the osteonJ, there is also notable heterogeneity, and the decrease of density within the osteon is not clearly discernible. The lowest mean density is observed at the location of the CL. Layer analysis confirms that the curve of canalicular densities behaves as a kind of plateau.

Additionally, the CL exhibits a non-zero value due to its connections with other osteons. Thanks to the qBEI image, we could see that the osteon is next to other osteons. With the density maps (Fig.3.1D), we could perceive that the bottom-right, the left and the upper sides are connected to other osteons. These connections seem to become more apparent with increasing depth of the osteon (Fig. 3.6).

Similarly to osteonG, the qBEI image reveals the presence of possible micropetrosis that we can see in figure 4.2 which corresponds to zero densities zones in the density maps in figure 3.1D.

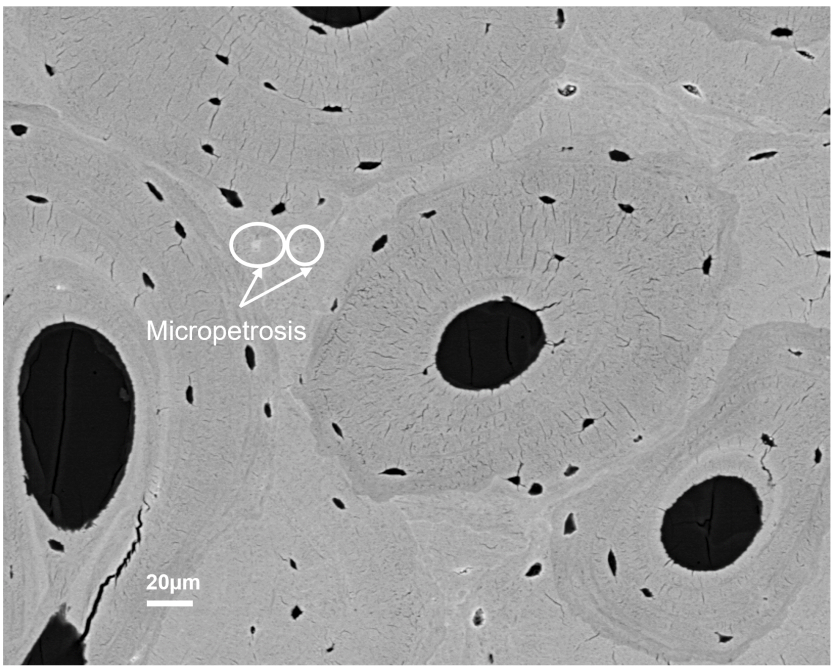

Figure 4.2: qBEI image of osteonJ. The micropetrosis are highlighted with the white circle.

4.1.4 OsteonC

OsteonC further confirms our previous findings regarding the osteonal density and the characteristics of the CL observed in the other three osteons. We observe that the density of the canaliculi increases with depth (Fig.3.5), such as the connections. Specifically, within the first 20 μm from the surface, there are no connections with the osteon on the left, but connections appear after 20 μm depth. Additionally, this osteon is connected to another osteon at the bottom (Fig.3.5).

This osteon is an osteon-in-osteon. Near the canal, the density is high, then it decreases before increasing again and then decreasing once more near the CL (Fig.3.1C). It is evident that there is another CL within this osteon, dividing it into inner and outer osteons, separated by a low-density blue ring representing the CL [43]. This CL is also visible from the qBEI image (Fig.2.1C).

4.1.5 General comparison

When comparing the osteons, osteonC exhibits the lowest mean value of the CL, while osteonJ, osteonO, and osteonG range from lowest to highest values, respectively. This difference can be attributed to the minimal number of connections observed in osteonC (Fig.3.1C), suggesting its isolation from the surrounding area.

In contrast, the other osteons show more connections with their surroundings, potentially explaining their higher mean CL values. Examining the mean density of the canaliculi, we find values similar to those reported by Repp et al. [6]. Additionally, osteons with lower mineral content appear to exhibit more low densities compared to those with higher mineral content when regarding the histograms of density.

There is a correlation between the density of the canaliculi and the degree of connectivity; an increase in connectivity correlates with higher canalicular density. This correlation has also been observed in other studies [50].

Generally, the highest mineralized regions correspond to regions with no visible network. Our hypothesis is that the network could be disrupted with aging and the rhodamine is not able to penetrate and access this specific region.

4.1.6 Orientation

Concerning the orientation of the canaliculi, if θ is less than 30°, it indicates that the canaliculi are oriented towards the Haversian canal with varying angles within the osteon. In this situation, the canalicular network might function as a supply network, meaning that the radial canaliculi provide the shortest connection between the central blood vessels and the osteocytes [115].

If θ is greater than 60°, besides their role in facilitating cell-to-cell communication, these lateral canaliculi could function to maintain the connectivity of the network in case larger parts of the radial network become clogged or interrupted [115] [116].

In all the osteons, the network is primarily composed of canaliculi oriented radially, but they change direction near the presumed location of the CL. Here, they are running parallel to or within the image plane.

In the osteon-within-an-osteon structure (*i.e.*, osteonC), two rings of lacunae are visible, indicating the presence of two CLs with corresponding changes in the orientation of the canaliculi. These two sections of the osteon are connected at certain points, but not uniformly throughout.

In osteonO, the network exhibits greater heterogeneity compared to others. This network is notably disrupted at the CL, although some connections do exist. OsteonG is also connected with the surrounding bone through radial canaliculi.

As mentioned earlier, there are red canaliculi present at the location of the Haversian canal, which can be explained by the method used to segment the canals during image processing. The rhodamine infiltrated all porosities including the canal, leading to a strong fluorescent signal at these locations. To prevent this error, the mask of the canal of the osteon should be slightly dilated. This hypothesis was tested with osteonG (Fig.3.11D). The difference is clear, as the canal in osteonG does not exhibit this red color, unlike the other osteons (Fig.3.11).

4.1.7 Generalities

Based on our results on connections, our hypothesis is that the osteon does not need many connections and behaves independently. While the canalicular density inside the osteons is very high, there are not a lot of connections between the osteons and their surroundings. These sparse connections may be explained by the fact that osteons do not need to communicate between each other. One could wonder if the loss of one connection has a huge impact on the whole system or if the robustness is ensured as in many biological materials. We also noticed that the connections between osteons are more present than the connections between osteon and IB.

4.2 Cells

Regarding the cells into the four osteons, we find that the stretching of the lacunae is relatively the same in each osteon. The mean value is around 0.6 for each osteon, which is comparable to what was found in mice in Mader et al [111]. This is a bit smaller than what was obtained in [112] for the lamellar and the central bone in rats.

The evaluation of the oblateness shows that this property does not change too much between the osteons. The mean values for the oblateness is relatively the same between osteonG, osteonJ, osteonO. It is around -0.2 which is comparable to the value found in [112] for the central bone observed in rats, and for mice in Mader et al [111]. It means that the lacunae in osteonG, osteonJ and osteonO are more prolate than for osteonC which has a mean value around 0. This value is comparable to the one found in [112] for the lamellar bone in rats.

We find no correlation between the calcium content of the osteon and the volume, the stretching and the oblateness of their lacunae.

This study also highlights that the lacunae oblateness is not correlated with their volume. In addition, none of the three morphometric lacuna parameters studied (oblateness, volume and stretching) are changing with the distance from the Haversian canal.

One interesting element found is that the number of lacunae seems to increase near the CL. This is comparable to the study of Gauthier et al. [60] where the properties of lacunae are found to vary according to the distance. If the CL is considered as the starting point of the bone deposition, it would mean that this potential increase in lacuna density could signify a higher activity of osteoblasts at the onset of bone remodeling.

Another plausible explanation for the potential increase in cells on the periphery is that they can detect micro-damage. Indeed, when the cracks are spreading into the bone matrix, they are cutting the canaliculi connected to some osteocytes leading to the death of those cells (micropetrosis) followed by the remodeling of this region. The cells may also function as a fluid flow mechanosensory system, thereby enabling better communication with the external environment.

4.3 Limitations

This study, however, presents some limitations. First, the number of samples was limited, which makes the comparison between osteons and their mineral content not entirely feasible. Additionally, the rhodamine used with CLS might not penetrate all parts of the osteon uniformly, leading to regions without visible networks, though it is uncertain if networks are truly absent in those areas.

During the TINA analysis, we created a mask of the osteon for image processing manually, which remains approximate and subject to our appreciation. We also observed that the mask of the canal needed to be dilated to avoid artifacts caused by rhodamine penetration into the canal. Furthermore, selecting parameters for the TINA analysis introduces subjectivity, as these parameters are chosen based on qualitative assessments of the results. The selection of subvolumes also presents a limitation. Choosing an appropriate subvolume involves a trade-off: it must be large enough to provide robust values but small enough to maintain good spatial resolution. To determine the correct size, we need to conduct tests, such as a convergence test on the subvolume, to confirm it is not too large, which would average out local heterogeneity and gradients, or too small, which would fail to accurately represent the local volume. In the time frame of the Master's thesis, the exact determination of the subvolume using convergence test could not be established.

Other limitations concern the study of the density of the canaliculi within the osteon. In particular, the method used to resize images for studying density across layers may not be the best choice. We had to resize the image or the mask to allow the multiplication of them because the size of the image had changed by applying a subvolume in the TINA analysis. Finally we chose to resize the image with an bicubic interpolation. We cannot be certain that the chosen method is optimal, as each method has its drawbacks. The layer thickness of 5 pixels might also be a limitation due to the uncertainty around the exact size of the CL, which we estimated. We had to make a compromise between the small size of the CL and the size of the subvolume because the thickness has to be large enough to include the size of the subvolume without cutting it. Indeed, if the subvolume is cut, it may be counted twice.

Lastly, an issue arises with cell analysis because TINA is known to be more accurate to study canaliculi than to study cells. Indeed the volume and the shape of cells may not be correctly computed, potentially affecting the precision of cell-related results since rhodamine may enter a bit the bone matrix. Therefore, we cannot fully trust TINA for cell analysis [117].

4.4 Perspectives

In this study of osteons, several research perspectives can be proposed to deepen our understanding and open new avenues for scientific exploration. Firstly, to continue our analysis, the number of connections and the orientation of the canaliculi should be quantified to confirm our current qualitative observations. The orientation of the lacunae should also be assessed, and the length of the canaliculi should be studied, as this could provide insights into bone maturation and nutrient transport mechanisms.

Secondly, to delve deeper into this study, it would be pertinent to test the hypothesis that fluid flow induced by loading produces forces detectable by cells. Experimental studies using mechanical loading models could quantify these forces and examine their impact on cellular signaling. The number of osteons could be increased

to evaluate how the network architecture influences the fluid flow pattern through the LCN as it was done by Van Tol et al [43].

Additionally, Focused Ion Beam in dual beam configuration with Scanning Electron Microscope or synchrotron nano-computed tomography could be used to explore regions where the network is not visible or where rhodamine did not penetrate, to evaluate the possible presence of LCN or even a nanochannels network. The possible presence of this network which is significantly smaller than the lacunar-canalicular network, may offer additional and complementary routes for the transport of mineral ions or mineral precursors. This network could play a crucial role in maintaining mineral homeostasis [92].

Finally, a systematic comparison of bone characteristics between young and elderly individuals, as well as a comparison between young and old tissues, could reveal structural changes related to aging. To enable this comparison, the number of samples should be increased. This increase would also allow for comparisons between different mineral contents to see their influence on the canalicular network and the potential connections with surrounding bone. These research perspectives offer promising directions for continuing the study of osteons and their surroundings to understand their connections and their behaviors.

Conclusion

The aim of this study was to evaluate the potential connections between osteons and their surroundings and if these connections are more likely with IB or other osteons. To conduct this study, a combination of qBEI and CLSM were performed on two human femoral bones.

Four osteons were analyzed using an open-access tool for image network analysis (TINA). A deepen analysis on the density of the canaliculi has been made followed by a qualitative analysis on their orientation. The cells have been studied by evaluating their shape according to the mineral content of the osteons and also according to their position within the osteon. A qualitative analysis has been performed on the density of the cells.

Concerning the canalicular density, we observed a high heterogeneity and, a decrease in density from the Haversian canal until reaching the CL for the four osteons analyzed. The mean density of the CL is weak but higher than zero due to the connections observed. We found few connections between the osteon and its surroundings, and these connections are more likely with other osteons than with IB. We also noticed a very striking absence of network in certain regions of IB corresponding to the highest mineralized regions. The network could be disrupted with aging and hence the rhodamine is not able to penetrate and access this specific region which leads to an absence of network. To evaluate this hypothesis, FIB-SEM tests should be conducted.

Concerning the qualitative analysis on the orientation of the canaliculi, we observed similar characteristics in all the osteons. Indeed, each osteon consists of blue canaliculi radiating towards its center. At the periphery, the canaliculi are perpendicular to the radial direction, meaning they run parallel to the Haversian canal or within the image plane. This finding means that there is a change in the orientation of the canaliculi at the periphery of the osteon. This analysis also confirms the presence of few connections between osteons and their surroundings, especially inter-osteonal. These sparse connections could be explained by the fact that osteons could behave independently and may not need to communicate and to exchange information.

Regarding the cells, one interesting finding is that the number of lacunae seems to increase near the CL which may signify a higher osteoblast activity at the onset of bone remodeling. It can also be explained by the fact that the cells can detect microdamage more easily at the periphery or function as a fluid flow mechanosensory system, enabling better communication with the external environment.

This work provides a characterization of the OLCN network inside and outside the periphery of an osteon, highlighting the existence of sparse connections between osteons and their surrounding bone. These connections are likely to play an important role in bone mechanosensitivity as well as cellular communication. To continue this analysis, a quantification of the connections through the CLs with respect to tissue age could be done by increasing the number of samples.

Bibliography

[1] Edesignua. *Collagen*. URL: https://depositphotos.com/fr/vector/collagen-fiber-molecule-amino-acid-sequence-molecular-structure-three-polypeptides.html.

[2] Maria-Grazia Ascenzi and Allison K. Roe. "The osteon: the micromechanical unit of compact bone". In: *Frontiers in Bioscience (Landmark Edition)* 17.4 (Jan. 1, 2012), pp. 1551–1581. ISSN: 2768-6698. DOI: 10.2741/4003.

[3] John G. Skedros et al. "Cement lines of secondary osteons in human bone are not mineral-deficient: new data in a historical perspective". In: *The Anatomical Record. Part A, Discoveries in Molecular, Cellular, and Evolutionary Biology* 286.1 (Sept. 2005), pp. 781–803. ISSN: 1552-4884. DOI: 10.1002/ar.a.20214.

[4] Nicolai Ernlund Lassen et al. "Coupling of Bone Resorption and Formation in Real Time: New Knowledge Gained From Human Haversian BMUs". In: *Journal of Bone and Mineral Research* 32.7 (July 1, 2017), pp. 1395–1405. ISSN: 0884-0431, 1523-4681. DOI: 10.1002/jbmr.3091. URL: https://academic.oup.com/jbmr/article/32/7/1395/7605423 (visited on 03/11/2024).

[5] Lynda F. Bonewald. "Osteocytes as dynamic multifunctional cells". In: *Annals of the New York Academy of Sciences* 1116 (Nov. 2007), pp. 281–290. ISSN: 0077-8923. DOI: 10.1196/annals.1402.018.

[6] Felix Repp et al. "Spatial heterogeneity in the canalicular density of the osteocyte network in human osteons". In: *Bone Reports* 6 (June 2017), pp. 101–108. ISSN: 23521872. DOI: 10.1016/j.bonr.2017.03.001. URL: https://linkinghub.elsevier.com/retrieve/pii/S2352187217300116 (visited on 03/11/2024).

[7] Lynda F. Bonewald. "The amazing osteocyte". In: *Journal of Bone and Mineral Research: The Official Journal of the American Society for Bone and Mineral Research* 26.2 (Feb. 2011), pp. 229–238. ISSN: 1523-4681. DOI: 10.1002/jbmr.320.

[8] Robert O. Ritchie, Markus J. Buehler, and Paul Hansma. "Plasticity and toughness in bone". In: *Physics Today* 62.6 (June 1, 2009), pp. 41–47. ISSN: 0031-9228, 1945-0699. DOI: 10.1063/1.3156332. URL: https://pubs.aip.org/physicstoday/article/62/6/41/390182/Plasticity-and-toughness-in-boneOur-bones-are-full (visited on 03/11/2024).

[9] Ulrike G. K. Wegst et al. "Bioinspired structural materials". In: *Nature Materials* 14.1 (Jan. 2015), pp. 23–36. ISSN: 1476-1122, 1476-4660. DOI: 10.1038/nmat4089. URL: https://www.nature.com/articles/nmat4089 (visited on 05/15/2024).

[10] Wolfgang Wagermaier, Klaus Klaushofer, and Peter Fratzl. "Fragility of Bone Material Controlled by Internal Interfaces". In: *Calcified Tissue International* 97.3 (Sept. 2015), pp. 201–212. ISSN: 0171-967X, 1432-0827. DOI: 10.1007/s00223-015-9978-4. URL: http://link.springer.com/10.1007/s00223-015-9978-4 (visited on 05/15/2024).

[11] Petar Milovanovic et al. "Osteocytic Canalicular Networks: Morphological Implications for Altered Mechanosensitivity". In: *ACS Nano* 7.9 (Sept. 24, 2013), pp. 7542–7551. ISSN: 1936-0851, 1936-086X. DOI: 10.1021/nn401360u. URL: https://pubs.acs.org/doi/10.1021/nn401360u (visited on 06/17/2024).

[12] Timothy Montalbano and Gang Feng. “Nanoindentation characterization of the cement lines in ovine and bovine femurs”. In: *Journal of Materials Research* 26.8 (Apr. 28, 2011), pp. 1036–1041. ISSN: 0884-2914, 2044-5326. DOI: 10.1557/jmr.2011.46. URL: http://link.springer.com/10.1557/jmr.2011.46 (visited on 06/17/2024).

[13] Yuxiao Zhou et al. “Elastic modulus mapping for bovine cortical bone from submillimeter- to submicron-scales using PeakForce Tapping atomic force microscopy”. In: *Extreme Mechanics Letters* 41 (Nov. 2020), p. 101031. ISSN: 23524316. DOI: 10.1016/j.eml.2020.101031. URL: https://linkinghub.elsevier.com/retrieve/pii (visited on 06/17/2024).

[14] Natalie A Sims and T John Martin. “Coupling the activities of bone formation and resorption: a multitude of signals within the basic multicellular unit”. In: *BoneKEy Reports* 3 (Jan. 8, 2014). ISSN: 20476396. DOI: 10.1038/bonekey.2013.215. URL: http://www.portico.org/Portico/article?article=pgk2ph97srv (visited on 06/17/2024).

[15] D. T. Denhardt and X. Guo. “Osteopontin: a protein with diverse functions”. In: *FASEB journal: official publication of the Federation of American Societies for Experimental Biology* 7.15 (Dec. 1993), pp. 1475–1482. ISSN: 0892-6638.

[16] X. Neil Dong, Xiaohui Zhang, and X. Edward Guo. “Interfacial strength of cement lines in human cortical bone”. In: *Mechanics & chemistry of biosystems: MCB* 2.2 (June 2005), pp. 63–68. ISSN: 1546-2048.

[17] et al. Cantamessa. “Abstract and Presentation”. In: *Proceedings of the 28th Congress of the European Society of Biomechanics (ESB)*. 2023.

[18] David B. Burr, Mitchell B. Schaffler, and Richard G. Frederickson. “Composition of the cement line and its possible mechanical role as a local interface in human compact bone”. In: *Journal of Biomechanics* 21.11 (Jan. 1988), pp. 939–945. ISSN: 00219290. DOI: 10.1016/0021-9290(88)90132-7. URL: https://linkinghub.elsevier.com/retrieve/pii/0021929088901327 (visited on 03/11/2024).

[19] P. Fratzl et al. “Structure and mechanical quality of the collagen–mineral nano-composite in bone”. In: *J. Mater. Chem.* 14.14 (2004), pp. 2115–2123. ISSN: 0959-9428, 1364-5501. DOI: 10.1039/B402005G. URL: http://xlink.rsc.org/?DOI=B402005G (visited on 03/11/2024).

[20] S. Weiner and H. D. Wagner. “THE MATERIAL BONE: Structure-Mechanical Function Relations”. In: *Annual Review of Materials Science* 28.1 (Aug. 1998), pp. 271–298. ISSN: 0084-6600. DOI: 10.1146/annurev.matsci.28.1.271. URL: https://www.annualreviews.org/doi/10.1146/annurev.matsci.28.1.271 (visited on 03/11/2024).

[21] D. Ruffoni et al. “The bone mineralization density distribution as a fingerprint of the mineralization process”. In: *Bone* 40.5 (May 2007), pp. 1308–1319. ISSN: 87563282. DOI: 10.1016/j.bone.2007.01.012. URL: https://linkinghub.elsevier.com/retrieve/pii/S8756328207000373 (visited on 03/11/2024).

[22] Jonathon Dj. Black and Baha John Tadros. “Bone structure: from cortical to calcium”. In: *Orthopaedics and Trauma* 34.3 (June 2020), pp. 113–119. ISSN: 18771327. DOI: 10.1016/j.mporth.2020.03.002. URL: https://linkinghub.elsevier.com/retrieve (visited on 03/11/2024).

[23] Dieter Felsenberg. “Struktur und Funktion des Knochens: Stützwerk aus Kollagen und Hydroxylapatit”. In: *Pharmazie in unserer Zeit* 30.6 (Nov. 2001), pp. 488–494. ISSN: 0048-3664, 1615-1003. DOI: 10.1002/1615-1003(200111)30:6<488::AID-PAUZ488>3.0.CO;2-U. URL: https://onlinelibrary.wiley.com/doi/10.1002/1615-1003(200111)30:6%3C488::AID-PAUZ488%3E3.0.CO;2-U (visited on 03/11/2024).

[24] Dick Heinegård and Åke Oldberg. “Structure and biology of cartilage and bone matrix noncollagenous macromolecules”. In: *The FASEB Journal* 3.9 (July 1989), pp. 2042–2051. ISSN: 0892-6638, 1530-6860. DOI: 10.1096/fasebj.3.9.2663581. URL: https://onlinelibrary.wiley.com/doi/10.1096/fasebj.3.9.2663581 (visited on 03/11/2024).

[25] Michel Van Der Rest and Robert Garrone. “Collagen family of proteins”. In: *The FASEB Journal* 5.13 (Oct. 1991), pp. 2814–2823. ISSN: 0892-6638, 1530-6860. DOI: 10.1096/fasebj.5.13.1916105. URL: https://onlinelibrary.wiley.com/doi/10.1096/fasebj.5.13.1916105 (visited on 03/11/2024).

[26] P. Fratzl. “Collagen: Structure and Mechanics, an Introduction”. In: *Collagen*. Ed. by Peter Fratzl. Boston, MA: Springer US, 2008, pp. 1–13. ISBN: 978-0-387-73905-2 978-0-387-73906-9. DOI: 10.1007/978-0-387-73906-9_1. URL: http://link.springer.com/10.1007/978-0-387-73906-9_1 (visited on 03/11/2024).

[27] Natalie Reznikov et al. “Fractal-like hierarchical organization of bone begins at the nanoscale”. In: *Science* 360.6388 (May 4, 2018), eaao2189. ISSN: 0036-8075, 1095-9203. DOI: 10.1126/science.aao2189. URL: https://www.science.org/doi/10.1126/science.aao2189 (visited on 03/11/2024).

[28] Marios Georgiadis, Ralph Müller, and Philipp Schneider. “Techniques to assess bone ultrastructure organization: orientation and arrangement of mineralized collagen fibrils”. In: *Journal of The Royal Society Interface* 13.119 (June 2016), p. 20160088. ISSN: 1742-5689, 1742-5662. DOI: 10.1098/rsif.2016.0088. URL: https://royalsocietypublishing.org/doi/10.1098/rsif.2016.0088 (visited on 03/11/2024).

[29] Kilian E. Stockhausen et al. “Collagen Fiber Orientation Is Coupled with Specific Nano-Compositional Patterns in *Dark* and *Bright* Osteons Modulating Their Biomechanical Properties”. In: *ACS Nano* 15.1 (Jan. 26, 2021), pp. 455–467. ISSN: 1936-0851, 1936-086X. DOI: 10.1021/acsnano.0c04786. URL: https://pubs.acs.org/doi/10.1021/acsnano.0c04786 (visited on 03/11/2024).

[30] SERVIER MEDICAL ART. *Bone*. URL: https://smart.servier.com/?s=bone.

[31] Mehdi Sadat-Shojai et al. “Synthesis methods for nanosized hydroxyapatite with diverse structures”. In: *Acta Biomaterialia* 9.8 (Aug. 2013), pp. 7591–7621. ISSN: 17427061. DOI: 10.1016/j.actbio.2013.04.012. URL: https://linkinghub.elsevier.com/retrieve/pii (visited on 03/11/2024).

[32] John D. Currey and Ron Shahar. “Cavities in the compact bone in tetrapods and fish and their effect on mechanical properties”. In: *Journal of Structural Biology* 183.2 (Aug. 2013), pp. 107–122. ISSN: 10478477. DOI: 10.1016/j.jsb.2013.04.012. URL: https://linkinghub.elsevier.com/retrieve/pii/S1047847713001123 (visited on 03/11/2024).

[33] Peter Fratzl and Richard Weinkamer. “Nature’s hierarchical materials”. In: *Progress in Materials Science* 52.8 (Nov. 2007), pp. 1263–1334. ISSN: 00796425. DOI: 10.1016/j.pmatsci.2007.06.001. URL: https://linkinghub.elsevier.com/retrieve/pii (visited on 03/11/2024).

[34] Natalie Reznikov et al. “The 3D structure of the collagen fibril network in human trabecular bone: Relation to trabecular organization”. In: *Bone* 71 (Feb. 2015), pp. 189–195. ISSN: 87563282. DOI: 10.1016/j.bone.2014.10.017. URL: https://linkinghub.elsevier.com/retrieve/pii/S8756328214003901 (visited on 03/11/2024).

[35] N. H. Hart et al. “Mechanical basis of bone strength: influence of bone material, bone structure and muscle action”. In: *Journal of Musculoskeletal & Neuronal Interactions* 17.3 (Sept. 1, 2017), pp. 114–139. ISSN: 1108-7161.

[36] Alizae Marny Mohamed. “An overview of bone cells and their regulating factors of differentiation”. In: *The Malaysian journal of medical sciences: MJMS* 15.1 (Jan. 2008), pp. 4–12. ISSN: 1394-195X.

[37] Paul Rowe, Adam Koller, and Sandeep Sharma. “Physiology, Bone Remodeling”. In: *StatPearls*. Treasure Island (FL): StatPearls Publishing, 2024. URL: http://www.ncbi.nlm.nih.gov/books/NBK499863/ (visited on 03/11/2024).

[38] Dimitrios J. Hadjidakis and Ioannis I. Androulakis. “Bone Remodeling”. In: *Annals of the New York Academy of Sciences* 1092.1 (Dec. 2006), pp. 385–396. ISSN: 0077-8923, 1749-6632. DOI: 10.1196/annals.1365.035. URL: https://nyaspubs.onlinelibrary.wiley.com/doi/10.1196/annals.1365.035 (visited on 03/11/2024).

[39] Tamara A. Franz-Odendaal, Brian K. Hall, and P. Eckhard Witten. "Buried alive: How osteoblasts become osteocytes". In: *Developmental Dynamics* 235.1 (Jan. 2006), pp. 176–190. ISSN: 1058-8388, 1097-0177. DOI: 10.1002/dvdy.20603. URL: https://anatomypubs.onlinelibrary.wiley.com/doi/10.1002/dvdy.20603 (visited on 03/11/2024).

[40] Keith Hill et al. "Bone Remodeling". In: *Encyclopedia of Exercise Medicine in Health and Disease*. Ed. by Frank C. Mooren. Berlin, Heidelberg: Springer Berlin Heidelberg, 2012, pp. 140–143. ISBN: 978-3-540-36065-0 978-3-540-29807-6. DOI: 10.1007/978-3-540-29807-6_314. URL: http://link.springer.com/10.1007/978-3-540-29807-6_314 (visited on 03/11/2024).

[41] A. M. Parfitt. "Osteonal and hemi-osteonal remodeling: the spatial and temporal framework for signal traffic in adult human bone". In: *Journal of Cellular Biochemistry* 55.3 (July 1994), pp. 273–286. ISSN: 0730-2312. DOI: 10.1002/jcb.240550303.

[42] A. M. Parfitt. "Quantum concept of bone remodeling and turnover: implications for the pathogenesis of osteoporosis". In: *Calcified Tissue International* 28.1 (Aug. 24, 1979), pp. 1–5. ISSN: 0171-967X. DOI: 10.1007/BF02441211.

[43] Alexander Franciscus van Tol et al. "The mechanoresponse of bone is closely related to the osteocyte lacunocanalicular network architecture". In: *Proceedings of the National Academy of Sciences of the United States of America* 117.51 (Dec. 22, 2020), pp. 32251–32259. ISSN: 1091-6490. DOI: 10.1073/pnas.2011504117.

[44] Pei Dong et al. "3D osteocyte lacunar morphometric properties and distributions in human femoral cortical bone using synchrotron radiation micro-CT images". In: *Bone* 60 (Mar. 2014), pp. 172–185. ISSN: 87563282. DOI: 10.1016/j.bone.2013.12.008. URL: https://linkinghub.elsevier.com/retrieve/pii/S8756328213004961 (visited on 06/17/2024).

[45] Peter Varga et al. "Synchrotron X-ray phase nano-tomography-based analysis of the lacunar–canalicular network morphology and its relation to the strains experienced by osteocytes in situ as predicted by case-specific finite element analysis". In: *Biomechanics and Modeling in Mechanobiology* 14.2 (Apr. 2015), pp. 267–282. ISSN: 1617-7959, 1617-7940. DOI: 10.1007/s10237-014-0601-9. URL: http://link.springer.com/10.1007/s10237-014-0601-9 (visited on 06/17/2024).

[46] Luis Cardoso et al. "Advances in assessment of bone porosity, permeability and interstitial fluid flow". In: *Journal of Biomechanics* 46.2 (Jan. 2013), pp. 253–265. ISSN: 00219290. DOI: 10.1016/j.jbiomech.2012.10.025. URL: https://linkinghub.elsevier.com/retrieve/pii/S002192901200632X (visited on 06/17/2024).

[47] Mitchell B. Schaffler et al. "Osteocytes: Master Orchestrators of Bone". In: *Calcified Tissue International* 94.1 (Jan. 2014), pp. 5–24. ISSN: 0171-967X, 1432-0827. DOI: 10.1007/s00223-013-9790-y. URL: http://link.springer.com/10.1007/s00223-013-9790-y (visited on 06/17/2024).

[48] Simona Bolamperti, Isabella Villa, and Alessandro Rubinacci. "Bone remodeling: an operational process ensuring survival and bone mechanical competence". In: *Bone Research* 10.1 (July 18, 2022), p. 48. ISSN: 2095-6231. DOI: 10.1038/s41413-022-00219-8. URL: https://www.nature.com/articles/s41413-022-00219-8 (visited on 06/17/2024).

[49] G. Marotti et al. "Quantitative evaluation on osteocyte canalicular density in human secondary osteons". In: *Bone* 16.1 (Jan. 1995), pp. 125–128. ISSN: 87563282. DOI: 10.1016/8756-3282(95)80022-I. URL: https://linkinghub.elsevier.com/retrieve/pii/875632829580022I (visited on 06/17/2024).

[50] Junning Chen et al. "Spatial variations in the osteocyte lacuno-canalicular network density and analysis of the connectomic parameters". In: *PLOS ONE* 19.5 (May 14, 2024). Ed. by Zhao Li, e0303515. ISSN: 1932-6203. DOI: 10.1371/journal.pone.0303515. URL: https://dx.plos.org/10.1371/journal.pone.0303515 (visited on 06/17/2024).

[51] Michael Kerschnitzki et al. “Poorly Ordered Bone as an Endogenous Scaffold for the Deposition of Highly Oriented Lamellar Tissue in Rapidly Growing Ovine Bone”. In: *Cells Tissues Organs* 194.2 (2011), pp. 119–123. ISSN: 1422-6405, 1422-6421. DOI: 10.1159/000324467. URL: https://www.karger.com/Article/FullText/324467 (visited on 03/12/2024).

[52] Vincent Ebacher et al. “Sub-lamellar microcracking and roles of canaliculi in human cortical bone”. In: *Acta Biomaterialia* 8.3 (Mar. 2012), pp. 1093–1100. ISSN: 17427061. DOI: 10.1016/j.actbio.2011.11.013. URL: https://linkinghub.elsevier.com/retrieve/pii (visited on 06/17/2024).

[53] Sheldon Weinbaum. “1997 Whitaker Distinguished Lecture: Models to Solve Mysteries in Biomechanics at the Cellular Level; A New View of Fiber Matrix Layers”. In: *Annals of Biomedical Engineering* 26.4 (July 1998), pp. 627–643. ISSN: 0090-6964. DOI: 10.1114/1.134. URL: http://link.springer.com/10.1114/1.134 (visited on 06/17/2024).

[54] Todd A. Curtis, Shahid H. Ashrafi, and Dennis F. Weber. “Canalicular communication in the cortices of human long bones”. In: *The Anatomical Record* 212.4 (Aug. 1985), pp. 336–344. ISSN: 0003-276X, 1097-0185. DOI: 10.1002/ar.1092120403. URL: https://onlinelibrary.wiley.com/doi/10.1002/ar.1092120403 (visited on 06/17/2024).

[55] Stefaan W. Verbruggen, Ted J. Vaughan, and Laoise M. McNamara. “Fluid flow in the osteocyte mechanical environment: a fluid–structure interaction approach”. In: *Biomechanics and Modeling in Mechanobiology* 13.1 (Jan. 2014), pp. 85–97. ISSN: 1617-7959, 1617-7940. DOI: 10.1007/s10237-013-0487-y. URL: http://link.springer.com/10.1007/s10237-013-0487-y (visited on 06/17/2024).

[56] Pascal R. Buenzli. “Osteocytes as a record of bone formation dynamics: A mathematical model of osteocyte generation in bone matrix”. In: *Journal of Theoretical Biology* 364 (Jan. 2015), pp. 418–427. ISSN: 00225193. DOI: 10.1016/j.jtbi.2014.09.028. URL: https://linkinghub.elsevier.com/retrieve/pii/S0022519314005670 (visited on 06/17/2024).

[57] Victoria Ip et al. “Remnant Woven Bone and Calcified Cartilage in Mouse Bone: Differences between Ages/Sex and Effects on Bone Strength”. In: *PLOS ONE* 11.11 (Nov. 9, 2016). Ed. by Joseph M Wallace, e0166476. ISSN: 1932-6203. DOI: 10.1371/journal.pone.0166476. URL: https://dx.plos.org/10.1371/journal.pone.0166476 (visited on 06/17/2024).

[58] A. Shipov et al. “Unremodeled endochondral bone is a major architectural component of the cortical bone of the rat (Rattus norvegicus)”. In: *Journal of Structural Biology* 183.2 (Aug. 2013), pp. 132–140. ISSN: 10478477. DOI: 10.1016/j.jsb.2013.04.010. URL: https://linkinghub.elsevier.com/retrieve/pii/S104784771300110X (visited on 06/17/2024).

[59] Stéphane Blouin et al. “Osteocyte lacunae in transiliac bone biopsy samples across life span”. In: *Acta Biomaterialia* 157 (Feb. 2023), pp. 275–287. ISSN: 17427061. DOI: 10.1016/j.actbio.2022.11.051. URL: https://linkinghub.elsevier.com/retrieve/pii (visited on 06/17/2024).

[60] Rémy Gauthier et al. “3D analysis of the osteonal and interstitial tissue in human radii cortical bone”. In: *Bone* 127 (Oct. 2019), pp. 526–536. ISSN: 87563282. DOI: 10.1016/j.bone.2019.07.028. URL: https://linkinghub.elsevier.com/retrieve/pii/S8756328219303023 (visited on 06/17/2024).

[61] G. Marotti, A. Z. Zallone, and M. Ledda. “Number, size and arrangement of osteoblasts in osteons at different stages of formation”. In: *Calcified Tissue Research* 21 Suppl (Aug. 1976), pp. 96–101. ISSN: 0008-0594.

[62] M.D. McKee and A. Nanci. “Osteopontin at mineralized tissue interfaces in bone, teeth, and osseointegrated implants: Ultrastructural distribution and implications for mineralized tissue formation, turnover, and repair”. In: *Microscopy Research and Technique* 33.2 (Feb. 1, 1996), pp. 141–164. ISSN: 1059-910X, 1097-0029. DOI: 10.1002/(SICI)1097-0029(19960201)33:2<141::AID-JEMT5>3.0.CO;2-W. URL: https://onlinelibrary.wiley.com/doi/10.1002/(SICI)1097-0029(19960201)33:2%3C141::AID-JEMT5%3E3.0.CO;2-W (visited on 06/17/2024).

[63] F. Barthelat. “Architectured materials in engineering and biology: fabrication, structure, mechanics and performance”. In: *International Materials Reviews* 60.8 (Nov. 17, 2015), pp. 413–430. ISSN: 0950-6608, 1743-2804. DOI: 10.1179/1743280415Y.0000000008. URL: http://www.tandfonline.com/doi/full/10.1179/1743280415Y. (visited on 03/11/2024).

[64] Marc André Meyers et al. “Biological materials: Structure and mechanical properties”. In: *Progress in Materials Science* 53.1 (Jan. 2008), pp. 1–206. ISSN: 00796425. DOI: 10.1016/j.pmatsci.2007.05.002. URL: https://linkinghub.elsevier.com/retrieve/pii (visited on 05/15/2024).

[65] Francois Barthelat and Reza Rabiei. “Toughness amplification in natural composites”. In: *Journal of the Mechanics and Physics of Solids* 59.4 (Apr. 2011), pp. 829–840. ISSN: 00225096. DOI: 10.1016/j.jmps.2011.01.001. URL: https://linkinghub.elsevier.com/retrieve/pii/S0022509611000020 (visited on 03/11/2024).

[66] Huajin Gao. “Application of fracture mechanics concepts to hierarchical biomechanics of bone and bone-like materials”. In: *Advances in Fracture Research*. Ed. by Alberto Carpinteri, Yiu-Wing Mai, and Robert O. Ritchie. Dordrecht: Springer Netherlands, 2006, pp. 101–137. ISBN: 978-1-4020-4626-1. DOI: 10.1007/978-1-4020-5423-5_8. URL: http://link.springer.com/10.1007/978-1-4020-5423-5_8 (visited on 03/11/2024).

[67] Francois Barthelat, Zhen Yin, and Markus J. Buehler. “Structure and mechanics of interfaces in biological materials”. In: *Nature Reviews Materials* 1.4 (Mar. 8, 2016), p. 16007. ISSN: 2058-8437. DOI: 10.1038/natrevmats.2016.7. URL: https://www.nature.com/articles/natrevmats20167 (visited on 03/11/2024).

[68] Markus J. Buehler. “Tu(r)ning weakness to strength”. In: *Nano Today* 5.5 (2010), pp. 379–383. ISSN: 17480132. DOI: 10.1016/j.nantod.2010.08.001. URL: https://linkinghub.elsevier.com/retrieve/pii/S1748013210001076 (visited on 05/15/2024).

[69] F. Song, A.K. Soh, and Y.L. Bai. “Structural and mechanical properties of the organic matrix layers of nacre”. In: *Biomaterials* 24.20 (Sept. 2003), pp. 3623–3631. ISSN: 01429612. DOI: 10.1016/S0142-9612(03)00215-1. URL: https://linkinghub.elsevier.com/retrieve/pii/S0142961203002151 (visited on 05/15/2024).

[70] John W.C. Dunlop, Richard Weinkamer, and Peter Fratzl. “Artful interfaces within biological materials”. In: *Materials Today* 14.3 (Mar. 2011), pp. 70–78. ISSN: 13697021. DOI: 10.1016/S1369-7021(11)70056-6. URL: https://linkinghub.elsevier.com/retrieve/pii/S1369702111700566 (visited on 03/11/2024).

[71] Ahmad Khayer Dastjerdi, Reza Rabiei, and Francois Barthelat. “The weak interfaces within tough natural composites: Experiments on three types of nacre”. In: *Journal of the Mechanical Behavior of Biomedical Materials* 19 (Mar. 2013), pp. 50–60. ISSN: 17516161. DOI: 10.1016/j.jmbbm.2012.09.004. URL: https://linkinghub.elsevier.com/retrieve/pii (visited on 03/11/2024).

[72] David I. Spivak et al. “Category theoretic analysis of hierarchical protein materials and social networks”. In: *PloS One* 6.9 (2011), e23911. ISSN: 1932-6203. DOI: 10.1371/journal.pone.0023911.

[73] Mobin Yahyazadehfar and Dwayne Arola. “The role of organic proteins on the crack growth resistance of human enamel”. In: *Acta Biomaterialia* 19 (June 2015), pp. 33–45. ISSN: 1878-7568. DOI: 10.1016/j.actbio.2015.03.011.

[74] Jae-Young Rho, Liisa Kuhn-Spearing, and Peter Zioupos. “Mechanical properties and the hierarchical structure of bone”. In: *Medical Engineering & Physics* 20.2 (Mar. 1998), pp. 92–102. ISSN: 13504533. DOI: 10.1016/S1350-4533(98)00007-1. URL: https://linkinghub.elsevier.com/retrieve/pii/S1350453398000071 (visited on 03/11/2024).

[75] M. Yahyazadehfar, Devendra Bajaj, and Dwayne D. Arola. “Hidden contributions of the enamel rods on the fracture resistance of human teeth”. In: *Acta Biomaterialia* 9.1 (Jan. 2013), pp. 4806–4814. ISSN: 17427061. DOI: 10.1016/j.actbio.2012.09.020. URL: https://linkinghub.elsevier.com/retrieve/pii/S1742706112004576 (visited on 05/15/2024).

[76] M. Mirkhalaf, A. Khayer Dastjerdi, and F. Barthelat. “Overcoming the brittleness of glass through bio-inspiration and micro-architecture”. In: *Nature Communications* 5.1 (Jan. 28, 2014), p. 3166. ISSN: 2041-1723. DOI: 10.1038/ncomms4166. URL: https://www.nature.com/articles/ncomms4166 (visited on 05/15/2024).

[77] Biorender. *Human anatomy*. URL: https://app.biorender.com/illustrations.

[78] Yayun Wang, Steven E. Naleway, and Bin Wang. “Biological and bioinspired materials: Structure leading to functional and mechanical performance”. In: *Bioactive Materials* 5.4 (2020), pp. 745–757. ISSN: 2452-199X. DOI: https://doi.org/10.1016/j.bioactmat.2020.06.003. URL: https://www.sciencedirect.com/science/article/pii/S2452199X20300943.

[79] Alexandra Tits et al. “Structural and functional heterogeneity of mineralized fibrocartilage at the Achilles tendon-bone insertion”. In: *Acta Biomaterialia* 166 (Aug. 2023), pp. 409–418. ISSN: 17427061. DOI: 10.1016/j.actbio.2023.04.018. URL: https://linkinghub.elsevier.com/retrieve/pii/S174270612300212X (visited on 06/17/2024).

[80] H.S. Gupta et al. “Two different correlations between nanoindentation modulus and mineral content in the bone–cartilage interface”. In: *Journal of Structural Biology* 149.2 (Feb. 2005), pp. 138–148. ISSN: 10478477. DOI: 10.1016/j.jsb.2004.10.010. URL: https://linkinghub.elsevier.com/retrieve/pii/S104784770400214X (visited on 06/17/2024).

[81] Britney Alexi Lamarche et al. “2D size of trabecular bone structure units (BSU) correlate more strongly with 3D architectural parameters than age in human vertebrae”. In: *Bone* 160 (July 2022), p. 116399. ISSN: 87563282. DOI: 10.1016/j.bone.2022.116399. URL: https://linkinghub.elsevier.com/retrieve/pii/S8756328222000758 (visited on 06/17/2024).

[82] Jean-Marie Delaisse. “The reversal phase of the bone-remodeling cycle: cellular prerequisites for coupling resorption and formation”. In: *BoneKEy Reports* 3 (Aug. 6, 2014). ISSN: 20476396. DOI: 10.1038/bonekey.2014.56. URL: http://www.portico.org/Portico/article?article=pgk2ph9fhq2 (visited on 06/17/2024).

[83] Thomas L. Andersen et al. “Understanding Coupling between Bone Resorption and Formation”. In: *The American Journal of Pathology* 183.1 (July 2013), pp. 235–246. ISSN: 00029440. DOI: 10.1016/j.ajpath.2013.03.006. URL: https://linkinghub.elsevier.com/retrieve/pii/S0002944013002629 (visited on 06/17/2024).

[84] R.K Nalla et al. “Mechanistic aspects of fracture and R-curve behavior in human cortical bone”. In: *Biomaterials* 26.2 (Jan. 2005), pp. 217–231. ISSN: 01429612. DOI: 10.1016/j.biomaterials.2004.02.017. URL: https://linkinghub.elsevier.com/retrieve/pii (visited on 06/17/2024).

[85] K. J. Koester, J. W. Ager, and R. O. Ritchie. “The true toughness of human cortical bone measured with realistically short cracks”. In: *Nature Materials* 7.8 (Aug. 2008), pp. 672–677. ISSN: 1476-1122, 1476-4660. DOI: 10.1038/nmat2221. URL: https://www.nature.com/articles/nmat2221 (visited on 03/11/2024).

[86] S. Mohsin, F. J. O’Brien, and T. C. Lee. “Osteonal crack barriers in ovine compact bone”. In: *Journal of Anatomy* 208.1 (Jan. 2006), pp. 81–89. ISSN: 0021-8782, 1469-7580. DOI: 10.1111/j.1469-7580.2006.00509.x. URL: https://onlinelibrary.wiley.com/doi/10.1111/j.1469-7580.2006.00509.x (visited on 06/17/2024).

[87] J.W. Ager, G. Balooch, and R.O. Ritchie. “Fracture, aging, and disease in bone”. In: *Journal of Materials Research* 21.8 (Aug. 1, 2006), pp. 1878–1892. ISSN: 0884-2914, 2044-5326. DOI: 10.1557/jmr.2006.0242. URL: http://link.springer.com/10.1557/jmr.2006.0242 (visited on 03/11/2024).

[88] Maximilien E. Launey, Markus J. Buehler, and Robert O. Ritchie. "On the Mechanistic Origins of Toughness in Bone". In: *Annual Review of Materials Research* 40.1 (June 1, 2010), pp. 25–53. ISSN: 1531-7331, 1545-4118. DOI: 10.1146/annurev-matsci-070909-104427. URL: https://www.annualreviews.org/doi/10.1146/annurev-matsci-070909-104427 (visited on 03/11/2024).

[89] Max Langer et al. "X-Ray Phase Nanotomography Resolves the 3D Human Bone Ultrastructure". In: *PLoS ONE* 7.8 (Aug. 29, 2012). Ed. by Xi-Nian Zuo, e35691. ISSN: 1932-6203. DOI: 10.1371/journal.pone.0035691. URL: https://dx.plos.org/10.1371/journal.pone.0035691 (visited on 06/17/2024).

[90] Emeline Raguin et al. "Focused ion beam-SEM 3D analysis of mineralized osteonal bone: lamellae and cement sheath structures". In: *Acta Biomaterialia* 121 (Feb. 2021), pp. 497–513. ISSN: 17427061. DOI: 10.1016/j.actbio.2020.11.002. URL: https://linkinghub.elsevier.com/retrieve/pii/S1742706120306450 (visited on 06/17/2024).

[91] Nina K. Wittig et al. "Bone Biomineral Properties Vary across Human Osteonal Bone". In: *ACS Nano* 13.11 (Nov. 26, 2019), pp. 12949–12956. ISSN: 1936-0851, 1936-086X. DOI: 10.1021/acsnano.9b05535. URL: https://pubs.acs.org/doi/10.1021/acsnano.9b05535 (visited on 06/17/2024).

[92] Tengteng Tang et al. "Subcanalicular Nanochannel Volume Is Inversely Correlated With Calcium Content in Human Cortical Bone". In: *Journal of Bone and Mineral Research* 38.2 (Dec. 1, 2020), pp. 313–325. ISSN: 0884-0431, 1523-4681. DOI: 10.1002/jbmr.4753. URL: https://academic.oup.com/jbmr/article/38/2/313-325/7499907 (visited on 05/15/2024).

[93] Michael Kerschnitzki. "Bone material characteristics influenced by osteocytes". In: (Mar. 1, 2012). In collab. with Humboldt-Universität Zu Berlin and Humboldt-Universität Zu Berlin. Publisher: [object Object]. DOI: 10.18452/16479. URL: https://edoc.hu-berlin.de/handle/18452/17131 (visited on 03/12/2024).

[94] Andreas Roschger. "Quantitative analysis of local mineral content and composition during bone growth and remodeling". In: (Sept. 20, 2015). In collab. with Humboldt-Universität Zu Berlin and Humboldt-Universität Zu Berlin. Publisher: [object Object]. DOI: 10.18452/17326. URL: https://edoc.hu-berlin.de/handle/18452/17978 (visited on 03/12/2024).

[95] Stéphane Blouin et al. "Confocal laser scanning microscopy-a powerful tool in bone research". In: *Wiener Medizinische Wochenschrift (1946)* 168.11 (Sept. 2018), pp. 314–321. ISSN: 1563-258X. DOI: 10.1007/s10354-018-0639-x.

[96] A. Boyde and S.J. Jones. "Back-scattered electron imaging of skeletal tissues". In: *Metabolic Bone Disease and Related Research* 5.3 (Jan. 1983), pp. 145–150. ISSN: 02218747. DOI: 10.1016/0221-8747(83)90016-4. URL: https://linkinghub.elsevier.com/retrieve/pii/0221874783900164 (visited on 03/11/2024).

[97] P. Roschger et al. "Bone mineralization density distribution in health and disease". In: *Bone* 42.3 (Mar. 2008), pp. 456–466. ISSN: 87563282. DOI: 10.1016/j.bone.2007.10.021. URL: https://linkinghub.elsevier.com/retrieve/pii/S8756328207008162 (visited on 03/11/2024).

[98] P Roschger et al. "Validation of quantitative backscattered electron imaging for the measurement of mineral density distribution in human bone biopsies". In: *Bone* 23.4 (Oct. 1998), pp. 319–326. ISSN: 87563282. DOI: 10.1016/S8756-3282(98)00112-4. URL: https://linkinghub.elsevier.com/retrieve/pii/S8756328298001124 (visited on 03/11/2024).

[99] Markus A. Hartmann et al. "Quantitative Backscattered Electron Imaging of Bone Using a Thermionic or a Field Emission Electron Source". In: *Calcified Tissue International* 109.2 (Aug. 2021), pp. 190–202. ISSN: 0171-967X, 1432-0827. DOI: 10.1007/s00223-021-00832-5. URL: https://link.springer.com/10.1007/s00223-021-00832-5 (visited on 03/11/2024).

[100] C. Lukas et al. “The Heterogeneous Mineral Content of Bone—Using Stochastic Arguments and Simulations to Overcome Experimental Limitations”. In: *Journal of Statistical Physics* 144.2 (July 2011), pp. 316–331. ISSN: 0022-4715, 1572-9613. DOI: 10.1007/s10955-011-0209-8. URL: http://link.springer.com/10.1007/s10955-011-0209-8 (visited on 05/15/2024).

[101] A. G. Robling and S. D. Stout. “Morphology of the drifting osteon”. In: *Cells, Tissues, Organs* 164.4 (1999), pp. 192–204. ISSN: 1422-6405. DOI: 10.1159/000016659.

[102] Christine M. Schnitzler and Julia M. Mesquita. “Cortical porosity in children is determined by age-dependent osteonal morphology”. In: *Bone* 55.2 (Aug. 2013), pp. 476–486. ISSN: 87563282. DOI: 10.1016/j.bone.2013.03.021. URL: https://linkinghub.elsevier.com/retrieve/pii/S8756328213001415 (visited on 06/15/2024).

[103] Christina Møller Andreasen et al. “Understanding Age-Induced Cortical Porosity in Women: The Accumulation and Coalescence of Eroded Cavities Upon Existing Intracortical Canals Is the Main Contributor”. In: *Journal of Bone and Mineral Research* 33.4 (Apr. 1, 2018), pp. 606–620. ISSN: 0884-0431, 1523-4681. DOI: 10.1002/jbmr.3354. URL: https://academic.oup.com/jbmr/article/33/4/606-620/7605472 (visited on 06/15/2024).

[104] B D Arhatari et al. “Imaging the 3D structure of secondary osteons in human cortical bone using phase-retrieval tomography”. In: *Physics in Medicine and Biology* 56.16 (Aug. 21, 2011), pp. 5265–5274. ISSN: 0031-9155, 1361-6560. DOI: 10.1088/0031-9155/56/16/012. URL: https://iopscience.iop.org/article/10.1088/0031-9155/56/16/012 (visited on 06/15/2024).

[105] M.F. Ericksen. “Histologic estimation of age at death using the anterior cortex of the femur”. In: *American Journal of Physical Anthropology* 84.2 (Feb. 1991), pp. 171–179. ISSN: 0002-9483, 1096-8644. DOI: 10.1002/ajpa.1330840207. URL: https://onlinelibrary.wiley.com/doi/10.1002/ajpa.1330840207 (visited on 06/15/2024).

[106] Isabel S. Maggiano et al. “Three-dimensional reconstruction of Haversian systems in human cortical bone using synchrotron radiation-based micro- CT : morphology and quantification of branching and transverse connections across age”. In: *Journal of Anatomy* 228.5 (May 2016), pp. 719–732. ISSN: 0021-8782, 1469-7580. DOI: 10.1111/joa.12430. URL: https://onlinelibrary.wiley.com/doi/10.1111/joa.12430 (visited on 06/15/2024).

[107] Felix Repp. *Tool for Image and Network Analysis (TINA)*. URL: https://www.euroscipy.org/2015/schedule/presentation/48/.

[108] D. Marr and E. Hildreth. “Theory of edge detection”. In: *Proceedings of the Royal Society of London. Series B, Biological Sciences* 207.1167 (Feb. 29, 1980), pp. 187–217. ISSN: 0950-1193. DOI: 10.1098/rspb.1980.0020.

[109] Siddharth Misra and Yaokun Wu. “Machine learning assisted segmentation of scanning electron microscopy images of organic-rich shales with feature extraction and feature ranking”. In: *Machine Learning for Subsurface Characterization*. Elsevier, 2020, pp. 289–314. ISBN: 978-0-12-817736-5. DOI: 10.1016/B978-0-12-817736-5.00010-7. URL: https://linkinghub.elsevier.com/retrieve/pii/B9780128177365000107 (visited on 03/30/2024).

[110] Maximilian Rummler. *TINA*. URL: https://gitlab.mpikg.mpg.de/rummler/TINAl.

[111] Kevin Scott Mader et al. “A quantitative framework for the 3D characterization of the osteocyte lacunar system”. In: *Bone* 57.1 (Nov. 2013), pp. 142–154. ISSN: 87563282. DOI: 10.1016/j.bone.2013.06.026. URL: https://linkinghub.elsevier.com/retrieve/pii/S8756328213002445 (visited on 06/15/2024).

[112] Fiona Linnea Bach-Gansmo et al. “Osteocyte lacunar properties in rat cortical bone: Differences between lamellar and central bone”. In: *Journal of Structural Biology* 191.1 (July 2015), pp. 59–67. ISSN: 10478477. DOI: 10.1016/j.jsb.2015.05.005. URL: https://linkinghub.elsevier.com/retrieve/pii/S1047847715300022 (visited on 08/02/2024).

[113] Petar Milovanovic and Björn Busse. “Micropetrosis: Osteocyte Lacunar Mineralization in Aging and Disease”. In: *Current Osteoporosis Reports* 21.6 (Dec. 2023), pp. 750–757. ISSN: 1544-1873, 1544-2241. DOI: 10.1007/s11914-023-00832-4. URL: https://link.springer.com/10.1007/s11914-023-00832-4 (visited on 08/02/2024).

[114] J. Klein-Nulend and L.F. Bonewald. “The osteocyte”. In: *Principles of Bone Biology*. Elsevier, 2020, pp. 133–162. ISBN: 978-0-12-814841-9. DOI: 10.1016/B978-0-12-814841-9.00006-3. URL: https://linkinghub.elsevier.com/retrieve/pii/B9780128148419000063 (visited on 08/02/2024).

[115] Felix Repp et al. “Coalignment of osteocyte canaliculi and collagen fibers in human osteonal bone”. In: *Journal of Structural Biology* 199.3 (Sept. 2017), pp. 177–186. ISSN: 10478477. DOI: 10.1016/j.jsb.2017.07.004. URL: https://linkinghub.elsevier.com/retrieve/pii/S1047847717301260 (visited on 03/11/2024).

[116] Philip Kollmannsberger et al. “The small world of osteocytes: connectomics of the lacuno-canalicular network in bone”. In: *New Journal of Physics* 19.7 (July 19, 2017), p. 073019. ISSN: 1367-2630. DOI: 10.1088/1367-2630/aa764b. URL: https://iopscience.iop.org/article/10.1088/1367-2630/aa764b (visited on 08/02/2024).

[117] Group Leader at the Max Planck Institute for Colloids Richard Weinkamer and Interfaces Research. *Email communication with Davide Ruffoni*. Apr. 2024.